Faculty of Physics and Astronomy
Heidelberg University

Master's Thesis

in Physics

submitted by

Pavel Rozov

born in Heidelberg

2026

Electrochemical studies on azo-compounds and of light effects in V_2O_5-based electrode materials

This master's thesis was conducted by Pavel Rozov
at the Kirchhoff-Institute for Physics
under the supervision of
Prof. Dr. Rüdiger Klingeler

This thesis investigates the effects of light and temperature on the electrochemical behavior of vanadium pentoxide (V_2O_5) as well as azo- and nitro-based organic compounds as potential electrode materials for lithium-ion batteries. Electrochemical studies by cyclic voltammetry and galvanostatic cycling suggest that deep lithiation of V_2O_5 down to 2 V promotes defect state formation, as indicated by additional peaks in the cyclic voltammograms. These features are associated with the γ-phase transition and the corresponding structural degradation of V_2O_5. Illumination only slightly increases the peak currents, i.e., by 21 %, and reduces overpotentials, indicating improved reaction kinetics. However, its influence on the specific capacity is negligible and is associated with the morphology of the material. Electrochemical studies of differently functionalized azo-based polymers reveal no significant redox activity of these materials. This is contrasted by the nitro-based materials, where several redox peaks are observed, the variation of which with the spacer length between the nitrophenyl group and the polymer backbone is investigated. Substituting electronegative CF_3 groups significantly affects the reduction peaks and likely shifts the corresponding oxidation peak beyond the voltage regime under study. Adding Carbon Black to the synthesis process increases the specific capacity by more than 400 %, indicating that an improved carbon matrix lifts kinetic limitations.

Elektrochemische Untersuchungen an Azoverbindungen sowie zu Lichteffekten in V_2O_5-basierten Elektrodenmaterialien

Im Rahmen dieser Arbeit werden die Einflüsse von Licht und Temperatur auf das elektrochemische Verhalten von Vanadiumpentoxid (V_2O_5) untersucht, sowie azo- und nitrobasierte organische Verbindungen als potenzielle Elektrodenmaterialien für Lithium-Ionen-Batterien. Elektrochemische Untersuchungen mittels zyklischer Voltammetrie und galvanostatischer Zyklierung legen nahe, dass eine Lithiierung von V_2O_5 bis 2 V die Bildung von Defektzuständen begünstigt, was sich in zusätzlichen Peaks in den zyklischen Voltammogrammen zeigt. Diese Merkmale stehen im Zusammenhang mit dem γ-Phasenübergang und der damit verbundenen strukturellen Degradation von V_2O_5. Bestrahlung mit Licht führt zu einer moderaten Erhöhung der Peakströme um ~ 21 % und verringert die Überspannungen, was auf eine verbesserte Reaktionskinetik hinweist. Der Einfluss auf die spezifische Kapazität bleibt jedoch vernachlässigbar und ist auf die Morphologie des Materials zurückzuführen. Elektrochemische Untersuchungen unterschiedlich funktionalisierter azo-basierter Polymere zeigen keine nennenswerte Redoxaktivität dieser Materialien. Die meisten nitrobasierten Verbindungen hingegen weisen mehrere Redoxpeaks auf, deren Veränderung in Abhängigkeit von der Spacerlänge zwischen der Nitrophenylgruppe und dem Polymerrückgrat untersucht wird. Die Substitution mit elektronegativen CF_3-Gruppen zeigt deutliche Auswirkungen auf die Reduktionspeaks und verschiebt vermutlich den zugehörigen Oxidationspeak außerhalb des untersuchten Spannungsbereichs. Die Zugabe von Carbon Black während des Syntheseprozesses erhöht die spezifische Kapazität um mehr als 400 %, was darauf hindeutet, dass eine verbesserte leitfähige Kohlenstoffmatrix kinetische Limitierungen reduziert.

Contents

1 Introduction **1**

2 Theoretical Background and Experimental Methods **3**

2.1 Electrochemistry 3

2.1.1 Galvanic Cell 3

2.1.2 Lithium-Ion Batteries 4

2.2 Electrochemical Measurements 6

2.2.1 Cyclic Voltammetry 6

2.2.2 Galvanostatic Cycling with Potential Limitation 7

2.3 Electrochemical Setup 8

2.3.1 Electrode Preparation 8

2.3.2 Cell Assembly 10

2.3.3 Measurement under Light-Illumination 10

3 Investigating Photo-Effects in V_2O_5 Batteries **13**

3.1 Vanadium Pentoxide: State of the Art 13

3.1.1 Photo-enhanced electrochemical effects in V_2O_5 (Boruah et al.) . . . 14

3.2 Setup for Temperature Measurements 17

3.3 Synthesis and Physical Characterization 19

3.4 Electrochemical Characterization 20

3.4.1 Electrochemical Behavior of V_2O_5 Cathodes in the Dark 20

3.4.2 Light and Heat Effects on Cycling Behavior 25

3.4.3 In-situ Temperature Measurement in LIB Cells 30

3.5 Conclusion and Outlook 35

4 Azo-Based Electrode Materials **37**

4.1 Organic Azo-Based Batteries: State of the Art 37

4.2 Synthesis of Organic Azo-Compounds 40

4.3 Electrochemical Characterization 43

4.3.1 Carbon Black Reference Measurement 43

4.3.2 Novel Azo Compounds 45

4.3.3 Nitro Compounds 52

4.4 Conclusion and Outlook 62

5 Summary and Outlook **65**

A Appendix **69**

1. Introduction

In recent decades, rapid technological development has significantly increased the demand for advanced energy storage systems [1]. In this regard, lithium-ion batteries (LIBs) have emerged as the key component in portable electronics, electric vehicles, and renewable energy applications. Their high energy density, long cycle life, and low self-discharge rate make them increasingly important in modern infrastructure [2, 3]. As reliance on LIBs continues to grow, the need to further enhance their performance, safety, and sustainability becomes increasingly critical [4, 5, 6].

A typical LIB cell consists of a solid positive (cathode) and negative electrode (anode), a liquid electrolyte containing lithium-ions, a polymeric separator and two current collectors enclosed within a sealed casing [7]. Among inorganic cathode materials, vanadium pentoxide (V_2O_5) has been studied extensively due to its high theoretical capacity and its layered crystal structure, enabling it to reversibly intercalate lithium ions [8, 9]. Integrating light-harvesting functionality into lithium-ion batteries enables the direct conversion of solar energy into stored chemical energy, avoiding inefficiencies associated with separate photovoltaics. The development of such photo-rechargeable lithium-ion batteries (photo-LIBs) would open a new route to a sustainable and renewable-based energy future, as they can both harvest solar energy and store it electrochemically [10]. V_2O_5 is a semiconductor with a bandgap in the visible range, making it a promising candidate for photo-LIBs [11]. Recent studies have shown that the material displays improved electrochemical performance under illumination, which is linked to photo-induced charge carrier processes [11, 12]. At the same time, illumination may also increase the local temperature of cell components, which can itself enhance electrochemical performance [13]. It is therefore essential to distinguish genuine photonic effects from purely thermal influences. Understanding the interplay between these contributions is crucial for assessing the role of light in the enhanced performance of photo-rechargeable lithium-ion batteries [14, 15].

Currently, electrode materials for LIBs are predominantly based on inorganic compounds due to their high energy density and strong chemical stability [16, 17]. However, their production is associated with considerable energy demand and pollutant

emissions [18]. In the search for more sustainable alternatives, organic electrode materials have gained growing attention due to their structural tunability, lower toxicity, natural abundance and flexibility [19, 20, 21]. Among these, azo compounds have emerged as promising candidates for redox-active electrode materials [22, 23]. Beside offering fast kinetics, the compounds achieve high theoretical capacities through the reversible multi-electron transfer capability of the azo (N = N) linkage [24, 25]. However, organic molecules are typically very dissolvable in electrolytes, which reduces the number of redox-active sites with subsequent cycling and leads to a stronger capacity fade [26, 27]. Incorporating the azo group into cross-linked polymer networks could thus make it more insoluble and enhance its cycling stability [28]. Furthermore, the electrochemical behavior of such materials can be systematically tuned by modifying substituents and spacer lengths [29]. A detailed electrochemical investigation is therefore required to understand how molecular architecture influences redox activity and long-term stability. Studying these relationships provides insight into the design principles of organic electrode materials and their potential role as sustainable alternatives to conventional inorganic systems.

This thesis investigates the electrochemical behavior of V_2O_5 electrodes, with particular emphasis on disentangling the effects of light and temperature on their performance, as well as the redox mechanisms of novel azo-based organic compounds. The following chapters present the electrochemical characterization of both inorganic and organic electrode materials evaluated as potential cathode and anode candidates for lithium-ion batteries. Chapter 2 offers insight into the theoretical background and experimental setup of the measurements used in this work. Chapter 3 examines the effects of light and temperature on the electrochemical performance of V_2O_5, aiming to disentangle photonic contributions from thermal effects through controlled experiments. Chapter 4 shifts to novel organic azo- and nitro-based compounds and examines their reaction mechanisms and redox behavior. The thesis concludes with a comprehensive summary of the experimental findings in Chapter 5 and outlines the perspectives for future research on the battery materials investigated.

2. Theoretical Background and Experimental Methods

2.1 Electrochemistry

2.1.1 Galvanic Cell

The fundamental operating principle of a battery lies in the conversion of chemical into electrical energy via redox reactions. Oxidation occurs at the anode, where electrons are released. These electrons are transfered to the cathode, where reduction takes place. The reaction formula is:

$$\mathrm{Ox} + ne^- \underset{\text{Oxidation}}{\overset{\text{Reduction}}{\rightleftharpoons}} \mathrm{Red}\,, \tag{2.1}$$

with Ox denoting the oxidized state of the electrode substance, Red the reduced state, and n the amount of electrons participating in the reaction. In a typical galvanic cell, the anode and cathode are separated by a porous separator immersed in an electrolyte solution. The separator prevents electrical contact between the electrodes while allowing ions to flow through. During discharge, electrons flow through an external circuit from the anode to the cathode, performing electrical work. In case of a rechargeable (secondary) battery, this process can be reversed by charging the cell with an external power source. Batteries that cannot be (dis-)charged reversibly are called primary cells. The redox reactions are driven by the electrochemical potential difference between anode and cathode. In thermal equilibrium, the electrochemical potential of an electrode is given by the Nernst equation:

$$E = E_0 + \frac{RT}{nF} \ln\left(\frac{a_{\mathrm{Ox}}}{a_{\mathrm{Red}}}\right)\,, \tag{2.2}$$

where E_0 is the standard electrode potential, $R = 8.3144\,\mathrm{J/(K\,mol)}$ the universal gas constant, T the temperature, n the number of transferred electrons, and $F = 26\,801.48\,\mathrm{mA\,h/mol}$ the Faraday constant. The activity $a_{\mathrm{Ox/Red}}$ denotes the amount of specimen per volume of solution, which participate in the oxidation/reduction process. The absolute potential of an individual electrode cannot be measured directly.

However, the potential difference between two half-cells is experimentally accessible. After connecting two half-cells, the difference in electrochemical potentials between cathode and anode is:

$$E_{\text{cell}} = E_{\text{cathode}} - E_{\text{anode}} \,, \tag{2.3}$$

which amounts to the voltage of a total galvanic cell. It is often also referred to as open-circuit voltage (OCV). Here, a high OCV (i.e. an increased cathode and low anode potential, respectively) is preferable to achieve large powers and therefore high energies in a battery.

2.1.2 Lithium-Ion Batteries

Lithium-ion batteries (LIBs) are the most commonly used rechargeable galvanic cells because of their high energy density, light weight, and efficient electrochemical behavior [3, 30, 31]. They usually consist of a cathode, an anode and a separator soaked in an electrolyte solution. Charge transport occurs via electrons in the external circuit as well as via lithium ions (Li^+) within the interior of the cell. The liquid electrolyte serves to transport Li^+ ions between anode and cathode. As such, it has high ionic but low electrical conductivity, which would otherwise facilitate internal short-circuits and reduce the overall efficiency and safety of the cell [32]. Modern LIBs use intercalation materials as active electrode materials for anode and cathode. In these materials, Li^+ ions are reversibly inserted (lithiated) and extracted (delithiated) during battery operation without destroying the crystal structure. Li^+-ions can also accumulate in the active material through conversion or alloying processes [33], but since the cathode materials examined in this study undergo solely intercalation reactions, these processes will not be discussed. Usually, the cathode/anode material is investigated in a half-cell configuration, where a Li-chip serves as both the counter electrode and the reference electrode. Lithium provides a stable and well-known reference potential (0 V vs. Li/Li^+), which allows the measured potential of the tested electrode to be directly related to the Li/Li^+ redox couple. In such a half-cell, the electrochemical properties of a single electrode can be evaluated without interference from a second active material. However, elemental lithium metal is unsafe due to its high reactivity with oxygen and water, and dendrites can form leading to short circuits [34]. To prevent this, the electrolyte is dripped into a porous separator which is placed between the Li-chip and the investigated electrode.

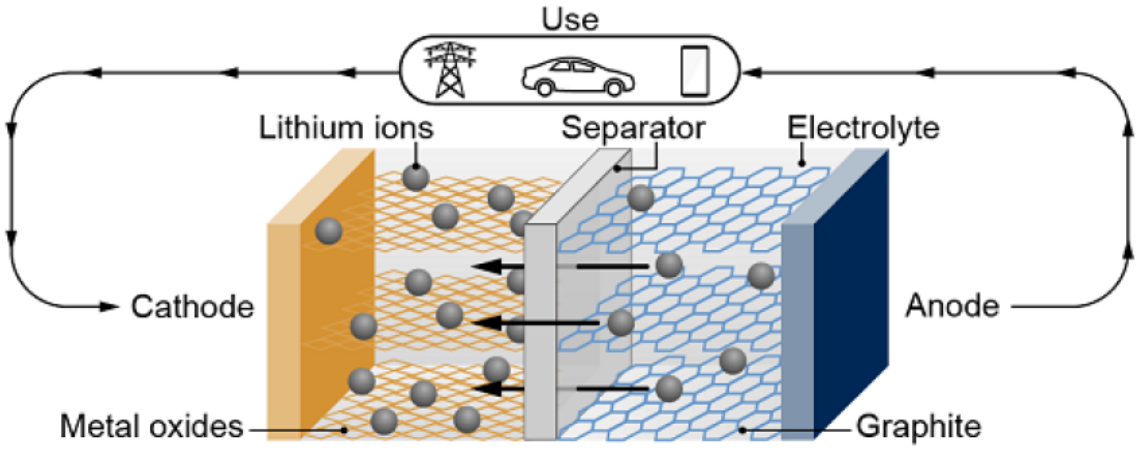


Figure 2.1: Illustration of the working principle of LIBs during discharge. The cell consists of a cathode (typically a metal oxide) and an anode (typically graphite), separated by a porous separator soaked in electrolyte. The high ionic conductivity of the separator allows diffusion of Li^+-ions from the anode to the cathode, where they recombine with electrons traveling through the external circuit. Adapted from [35].

For the anode of an LIB, one typically uses graphite, while a typical cathode is made of lithium-containing metal oxides such as $LiCoO_2$, $LiMn_2O_4$ or $LiFePO_4$ [36, 37]. In terms of electrolyte, a lithium salt is used, usually lithium hexafluorophosphate ($LiPF_6$), lithium perchlorate ($LiClO_4$) or lithium bis(trifluoromethylsulfonyl)imide (LiTFSI), dissolved in organic solvents. Such solvents can be ethylene carbonate (EC), propylene carbonate (PC), dimethyl carbonate (DMC), diethyl carbonate (DEC), or ethyl methyl carbonate (EMC) [38]. During discharge, Li-ions move from the anode to the cathode through the electrolyte, while electrons flow through the external circuit (see Fig. 2.1). The process is reversed during charging. To enable electronic conduction, the active electrode material is coated onto an inert current collector (usually copper for the anode, aluminum for the cathode). Due to the low conductivity of many cathode materials, they are mixed with conductive carbon and a polymer binder to form a slurry, which then adheres well to the current collector [34].

There are a few key performance parameters of a battery: The specific capacity (expressed in mA h/g) denotes the amount of charge that is stored or released per mass of active material. The cycling performance refers to how many charge-discharge cycles a battery can undergo without significant loss in specific capacity. The Coulomb efficiency (CE, see eq. 2.6) represents the ratio of discharge capacity to charge

capacity within a single cycle; deviations from 100 % suggest irreversible reactions occurring in the cell. The amount of energy that can be stored in the battery (in W/kg) is measured by the specific power density, which is calculated as the product of the nominal cell voltage and specific capacity, normalized by weight. The rate performance measures the ability of a battery to charge and discharge at alternating current densities. A detailed explanation of the electrochemistry in a battery can be found in [34, 39, 40].

2.2 Electrochemical Measurements

2.2.1 Cyclic Voltammetry

Cyclic voltammetry (CV) is a widely used electrochemical technique to study reduction and oxidation processes in a battery [41]. A triangular voltage E is applied to the working electrode relative to the reference electrode, sweeping the potential linearly from an initial (E_i) to a final potential (E_f) and then back to E_i (see Fig. 2.2a), typically at scan rates $\mathrm{d}E/\mathrm{d}t$ of $0.1 - 1\,\mathrm{mV/s}$. The resulting current is measured over time (Fig. 2.2b) and plotted against the applied potential, resulting in a cyclic voltammogram (CV, see Fig. 2.2c).

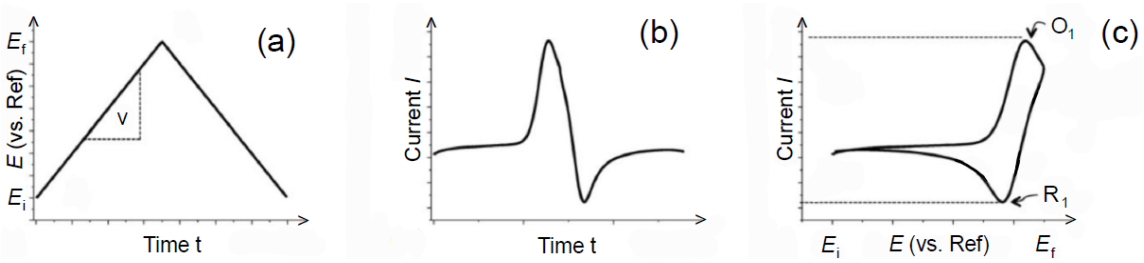


Figure 2.2: Example of a cyclic voltammetry measurement. (a) triangular voltage applied to the cell, (b) the resulting current detected over time, (c) the measured cyclic voltammogram, with an oxidation peak O_1 and reduction peak R_1. Adapted from [42].

The observed peaks (e.g. O_1 and R_1) correspond to redox reactions, with their potential values E_R and E_O (for reduction and oxidation, respectively) providing insight into the specific underlying processes. Here, the redox potential is defined as $E_{1/2} = \frac{1}{2}(E_\mathrm{R} + E_\mathrm{O})$ [43]. This work follows the IUPAC convention, which means that oxidation is indicated by a positive current and reduction by a negative one. From the height and width of the current peaks, one can deduce the kinetics of the redox

process, as well as the degree of crystallinity of the electrode material [44, 45]. Kinetic barriers, e.g. mass transport limitations or charge transfer resistance, prevent the redox reactions from occurring at the thermodynamic equilibrium potentials. The extra voltage needed to drive a redox reaction is called overpotential η and can be deduced from the difference between both redox peaks, $\eta = E_{\mathrm{R}} - E_{\mathrm{O}}$ [43]. In case of oxidation, the overpotential increases the required potential for a reaction, and in case of reduction, it decreases it. Hence, an elevation of the overpotential, which indicates poor diffusion of reactants or inefficient electron transfer, is reflected in CV as an increase in peak separation [46]. A more detailed introduction to CV can be found in [47].

2.2.2 Galvanostatic Cycling with Potential Limitation

Galvanostatic cycling with potential limitation (GCPL) is a method to study the charging and discharging behavior of a battery cell, as well as the specific capacity and cyclability. For this, a constant (dis-)charge current is applied to a cell, and the resulting voltage profile is measured over time. GCPL-measurements can offer valuable insights into the electrochemical behavior of the system. The shape of the voltage profile helps identifying the nature of the underlying process. For instance, in a Nerstian system, the voltage stabilizes in the form of a plateau near the equilibrium potential of the redox couple. Each plateau indicates a redox process and corresponds to a peak in cyclic voltammetry. The amount of charge transferred during cycling reflects the lithium content in the electrode material and is quantified as the specific capacity:

$$C_{\mathrm{spec}} = \frac{1}{m} \int_0^t I(t) \mathrm{d}t \,, \tag{2.4}$$

calculated by integrating the measured current I over time t and normalizing to the mass m of the active electrode material. Using Faraday's law, one can calculate the theoretical, material-specific capacity as:

$$C_{\mathrm{theo}} = \frac{z \cdot F}{M} \,, \tag{2.5}$$

where z denotes the amount of electrons stored in each unit cell, F the Faraday constant and M the molar mass of the active material. Both current and capacity are normalized to the mass load of the active electrode components.

Anode materials studied in this work are tested within a voltage window of 0.01 to

3.00 V. In this range, the influence of Carbon black, which is used as part of the working electrode, must also be considered, as it is electrochemically active at low voltages and can influence the measured specific capacity. In order to determine this influence, blank measurements were performed (see Section 4.3.1), where the electrodes consist out of CB and PVDF in a mass ratio of 85:15. Cycling rates for electrode materials are typically reported in C-rates, where a C/x-rate corresponds to charging or discharging the theoretical capacity within x hours.

In addition to capacity, GCPL allows the evaluation of the Coulombic efficiency (CE) [48]:

$$\mathrm{CE} = \frac{\text{discharge capacity}}{\text{charge capacity}}\,, \tag{2.6}$$

which measures the reversibility of the electrochemical processes and is defined as the ratio of the charge extracted during discharge to the charge supplied during charging. Furthermore, GCPL offers insights into the cycling stability, which quantifies the retention of capacity over multiple charge-discharge cycles. The overall electrochemical performance, which is a key metric for assessing the viability and suitability of battery materials, is defined by the combined evaluation of specific capacity and cycling stability.

2.3 Electrochemical Setup

This section provides an overview of sample preparation and electrochemical measurement techniques. Due to the air sensitivity of some components, the fabrication of the battery cells was carried out in a glove box with an argon atmosphere (O_2 concentration < 1 ppm, H_2O concentration < 1 ppm). To investigate the electrochemical properties, a multi-channel VMP3 [49], a VSP potentiostat [50] and a battery cycler (BCS) [51] from BioLogic were utilized. The room temperature was controlled to be constant at 25°C. For all devices, the software "EC-Lab" from BioLogic was used [52]. Before each measurement, an OCV resting time of $12 - 24$ h was carried out to ensure a state of equilibrium.

2.3.1 Electrode Preparation

All handling and preparation steps of the active material have to be executed inside an argon-filled glovebox (H_2O, $O_2 < 1$ ppm). For the V_2O_5-based electrodes

prepared in this work (see Chap. 3), four main components are used: the active material (AM), reduced graphene oxide (rGO, Sigma Aldrich), poly(3-hexylthiophene-2,5-diyl) (P3HT, Ossila) and the binder polyvinylidene difluoride (PVDF, Sigma Aldrich). For the purposes of this work, the weight ratio of AM:rGO:P3HT:PVDF was set to 93:1:1:5. As for the azo-based electrodes (see Chap. 4), the used components were AM, Carbon black (CB, Super C65, Timcal) and PVDF in a weight ratio of 60:30:10 (AM:CB:PVDF). After combining the components, they are disperged in 200 µL N-Methyl-2-pyrrolidone (NMP, Alfa Aesar) for 70 min using an ultrasonic dismembrator (Fisher Scientific FB120) with a pulsed setting (15 s pulse, 20 s resting) and an amplitude of 35 %. The mixture is then evacuated (pressure $p < 0.01$ mbar) inside the transfer chamber of the glovebox for $15 - 30$ min to evaporate parts of the NMP and thus increase the viscosity. After reaching a suitable viscosity, the paste is applied homogeneously to a mesh-like current collector (diameter $d = 10$ mm) by hand using a spatula. For V_2O_5-electrodes, one uses light-transparent carbon felt (CF, Sigracet 39 AA) current collectors, while for the azo compounds, aluminium (Al) and copper (Cu) meshes are used. The coated electrodes are dried inside the evacuated transfer chamber overnight and subsequently compressed using a hydraulic press at 10 MPa to further improve electrode density and adhesion. The last step has to be skipped for the CF meshes due to their high fragility. Finally, the electrodes are weighted to deduce the amount $\Delta m = m_f - m_i$ of the dry components on each mesh (m_i/m_f mass of mesh before/after coating). The mass loading of the AM on each electrode is assumed to be 93 % of Δm for V_2O_5, and 60 % for the azo-based electrodes.

The quality of electrode fabrication strongly influences the reproducibility of the electrochemical measurements. Key factors affecting electrode quality include the homogeneity during both the mixing process and the application to the current collector, as well as the mass loading of the electrodes. Since these steps are performed manually by hand, precise control over these parameters is inherently limited. Based on repeated experiments and comparative measurements, the uncertainty in electrochemical measurements, arising from variations in electrode preparation, was estimated to be between 5 % and 10 %, which is typical for laboratory-scale studies of this kind [53].

2.3.2 Cell Assembly

The coin cells used in this work (see Fig. 2.3) were commercially available type 2032 housings ($d = 20\,\text{mm}$, height $= 3.2\,\text{mm}$) made of 304/316 stainless steel. Each cell consists of two caps, a stainless steel spring, a stainless steel spacer, a lithium disk (Alfa Aesar, 99.9 % metal basis, $d = 10\,\text{mm}$) as counter/reference electrode, and two non-woven glass fiber separators (Whatman GF/D, $d = 12\,\text{mm}$), each soaked with 65 µL of electrolyte. The standard electrolyte used in this work was 1 M LiTFSI in a 1:1 ratio (by volume) of Dimethoxyethane (DME) and 1,3-Diloxane (DOL). The lithium foil serves as both the counter and reference electrode, such that all voltages measured in this work are referenced against the Li/Li^+ half-cell (as discussed in Section 2.1.2). The cells were assembled inside an argon-filled glove box and sealed using an electric press (MSK 640-G, TMAX) with a pressure of approximately 900 kg, ensuring airtight sealing for measurements outside the glove box.

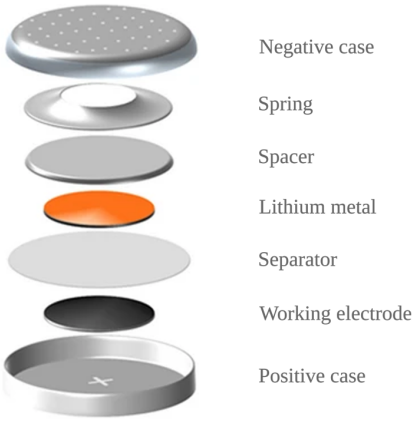


Figure 2.3: Schematic illustration of the coin cell used in this work. Adapted from [54].

2.3.3 Measurement under Light-Illumination

For the illuminated electrochemical setup, the standard CR2032-type coin cells were replaced by custom-designed windowed coin cells manufactured by KIT Campus Transfer GmbH [55] (see Fig. 2.4 right). In their production process, a 6 mm diameter hole was drilled into the upper stainless steel cap. To keep the battery cell airtight, a Kapton window of 75 µm thickness was sealed onto the hole using EPOXY resin. Such a structural design enabled in-situ light irradiation onto the V_2O_5-electrode during the measurements.

Illumination of the battery cell was provided by a high-power tunable Xenon lamp (TLS120 XeLamp), whose light was guided via an optical glass fiber. The fiber was positioned $\sim 25\,\text{mm}$ above the cell window to ensure full exposure of the electrode's illuminated area.

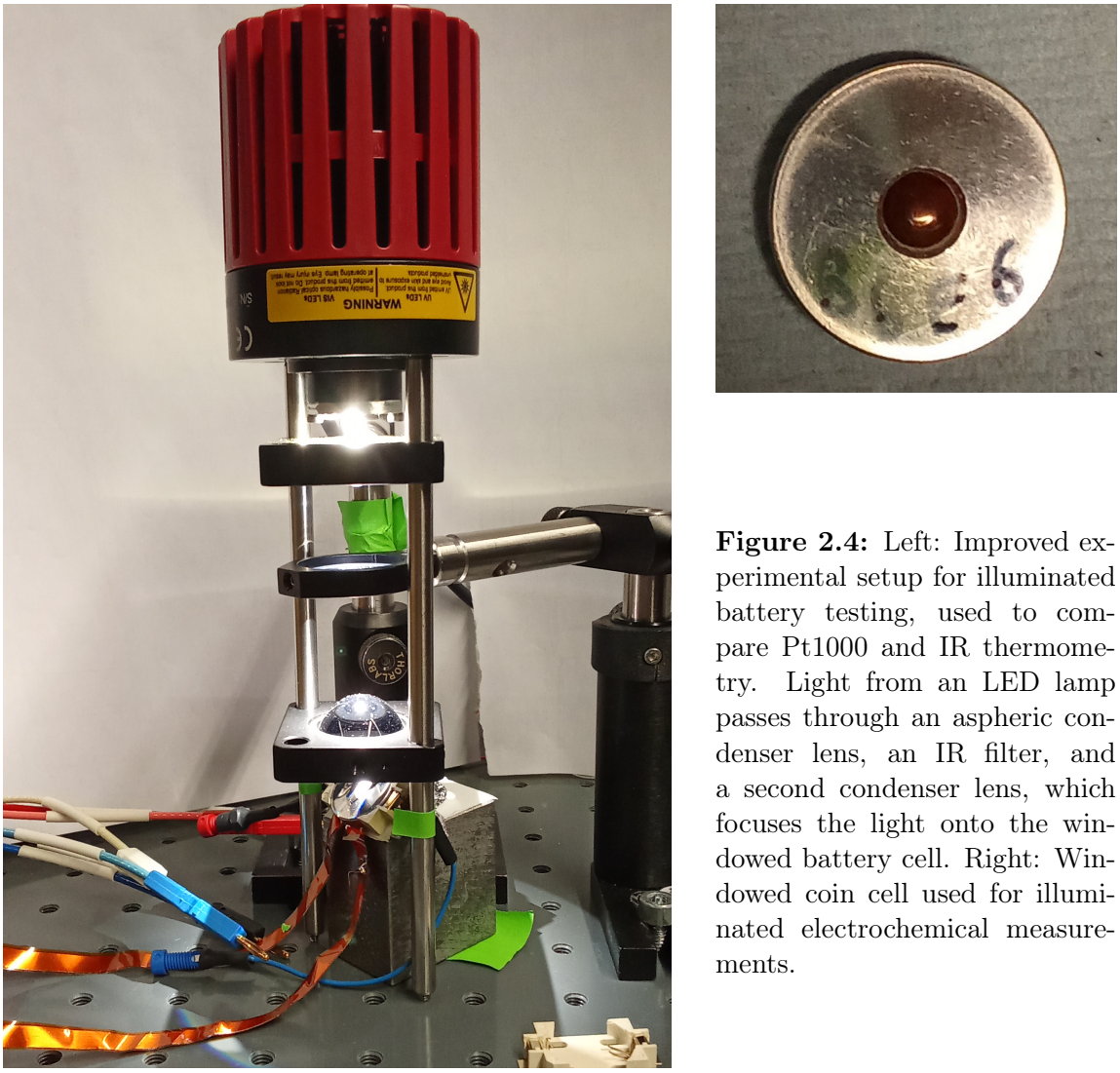


Figure 2.4: Left: Improved experimental setup for illuminated battery testing, used to compare Pt1000 and IR thermometry. Light from an LED lamp passes through an aspheric condenser lens, an IR filter, and a second condenser lens, which focuses the light onto the windowed battery cell. Right: Windowed coin cell used for illuminated electrochemical measurements.

To minimize thermal effects, both an ultraviolet (UV) filter (Edmund N-WG320) and an infrared (IR) filter (Edmund EDSP800) were positioned in between fiber output and coin cell. This allowed illumination with broadband white light in a wavelength range of $320 - 800\,\text{nm}$ and a power of $\sim 53\,\text{mW}$ at the fiber end [56]. Temperature measurements of the illuminated electrode were conducted via a Pt1000 resistance thermometer (32208707 M222, Yageo Nexensos [57]), which was embedded inside the battery cell (see Section 3.2).

For future battery testing under light, a more advanced illumination setup was developed. A neutral white LED light source (MNWHLP1, ThorLabs) was used for comparative temperature measurements of the Pt1000 sensor and an IR thermometer (Fluke 62 MAX [58]) aimed at the cell window (Section 3.4.3, setup in Fig. 2.4 left). For power supply and intensity regulation, the LED was connected to a T-Cube LED driver (LEDD1B, ThorLabs) with an analog current adjustment. To focus as much light as possible onto the cell window, two aspheric condenser lenses were placed in between light source and coin cell. The first lens (ACL12708U, diameter $d = 12.7\,\mathrm{mm}$, ThorLabs) was positioned at a distance from the LED that approximately corresponded to its focal length of $f_1 = 8\,\mathrm{mm}$. With this, the majority of the light was captured and the outgoing light beam consisted of almost parallel rays. The second lens (ACL25416U, diameter $d = 25.4\,\mathrm{mm}$, ThorLabs), which was placed $\sim 5\,\mathrm{cm}$ away from the first one, focused the beam onto the coin cell. The distance to the cell was $\sim 11\,\mathrm{mm}$, which was slightly below the lens's focal length of $f_2 = 16\,\mathrm{mm}$ to ensure full illumination of the cell window. To reduce thermal load, an IR filter was positioned in the beam path between both condenser lenses.

3. Investigating Photo-Effects in V_2O_5 Batteries

3.1 Vanadium Pentoxide: State of the Art

V_2O_5 belongs to the class of two-dimensional (2D) transition metal oxides and is a very promising cathode material for lithium-ion batteries. It offers high theoretical capacities of 294 and 441 mA h/g for intercalation of 2 and 3 Li-ions, respectively [59], as well as a large open-circuit voltage ($\sim$ 3.4 V vs Li/Li^+) [60]. The material is safe, naturally abundant, and very cost-effective to produce [61, 62, 63]. In its unlithiated state, V_2O_5 has a layered, orthorhombic crystal structure with a space group symmetry of *Pmmn* [9]. The layers consist of $[VO_5]$ square pyramids that share corners and edges to form zigzag-shaped lamellar sheets along the crystallographic a-direction (see Fig. 3.1a). These sheets, which have an interlayer gap of 4.368 Å, are held together by weak van der Waals forces [9]. Li-ions can intercalate reversibly into the gaps without destroying the lattice, which provides good cycling stability [64].

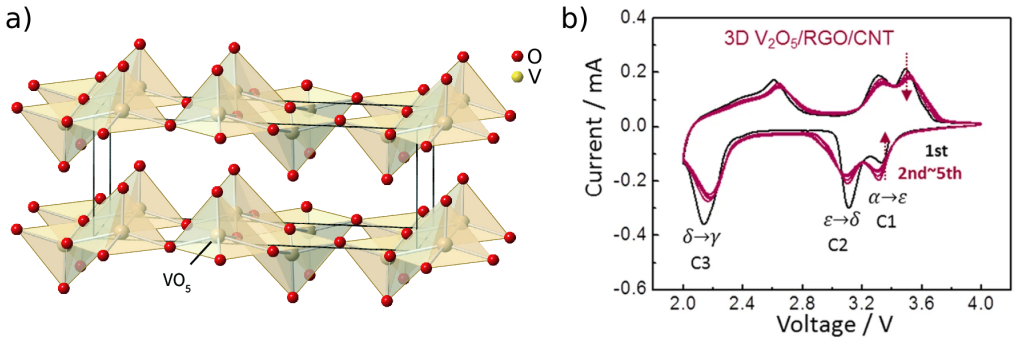


Figure 3.1: (a) Crystal structure of V_2O_5 showing VO_5 octahedral units (taken from [65]). (b) CV-measurement of a 3D V_2O_5 composite with the electrolyte 1 M $LiPF_6$ in EC/DEC (scan rate 0.2 mV/s) in the voltage range of $2 - 4$ V. It shows 3 distinct cathodic and anodic peaks, which correspond to the 3 characteristic phase transitions (3.1) - (3.3) of V_2O_5. Adapted from [66].

Upon cycling, vanadium switches reversibly between the oxidation states V^{4+} and V^{5+}, as the Li-ions (de-)intercalate from the lattice [67]. During these processes,

V_2O_5 acquires several different phases. The proposed reaction mechanisms are [68]:

$$V_2O_5 + 0.5Li^+ + 0.5e^- \longleftrightarrow \varepsilon\text{-}Li_{0.5}V_2O_5\,, \tag{3.1}$$

$$\varepsilon\text{-}Li_{0.5}V_2O_5 + 0.5Li^+ + 0.5e^- \longleftrightarrow \delta\text{-}LiV_2O_5\,, \tag{3.2}$$

$$\delta\text{-}LiV_2O_5 + Li^+ + e^- \longleftrightarrow \gamma\text{-}Li_2V_2O_5\,. \tag{3.3}$$

In the unlithiated phase, also called α-phase, both vanadium atoms in a V_2O_5-unit are oxidized as V^{5+} [67]. Upon lithiation, Li-ions intercalate into the material, leading to a partial reduction of vanadium atoms to V^{4+}. The material stabilizes in the ε-phase (3.1), where $\sim 50\,\%$ of the V_2O_5-units hold a Li-ion [68]. With further lithiation, the structure adjusts itself to accommodate more Li^+. The stacking sequence shifts along the c-axis by half a unit cell, resulting in the δ-phase (3.2) with a space group symmetry of *Amma* [69]. In this phase, every V_2O_5-unit holds on average one Li-ion. Finally, with even further Li^+-intercalation, the γ-phase (3.3) is stabilized, where VO_5-pyramids undergo rotations by 90° in opposite directions [70]. This causes a distortion of the crystal structure, and the symmetry of the space group changes to *Pnma* [71]. In this phase, every V_2O_5-unit stores on average two Li-ions, with both vanadium atoms being reduced to V^{4+} [67]. These reversible phase transitions can be visualized in a cyclic voltammogram with a potential window of $2 - 4\,V$ (Fig. 3.1b), where the transitions from α to ε, ε to δ and δ to γ occur as reduction peaks at $\sim 3.33\,V$, $\sim 3.11\,V$ and $\sim 2.13\,V$, respectively [66]. The corresponding reverse transitions appear as subsequent oxidation peaks at $\sim 2.61\,V$, $\sim 3.31\,V$ and $\sim 3.50\,V$ [66]. Further lithiation causes a complete collapse of the layered structure into a cubic ω-$Li_3V_2O_5$ phase [72]. It is a reconstructive phase transition that requires breaking of the atomic (V−O) bonds, which makes it irreversible [73]. A clear understanding of this structure is still missing, and some studies propose that it may consist of a mixture of lithium vanadates and oxides [74].

3.1.1 Photo-enhanced electrochemical effects in V_2O_5 (Boruah et al.)

In addition to promising electrochemical characteristics, V_2O_5 also offers photoactive properties. In a recent study, Boruah et al. demonstrated that V_2O_5-based cathodes can exhibit enhanced electrochemical performance under illumination [11].

The proposed photocharging mechanism of such an electrode is depicted in Fig. 3.2a. With a band gap of $\sim 2.2\,\mathrm{eV}$, V_2O_5 is capable of absorbing light in the optical range to generate electron-hole pairs [11]. V^{4+} is photo-oxidized to V^{5+}, while electrons are excited into the conduction band. With the help of a conductive additive in the cathode, in this case reduced graphene oxide (rGO), the photoelectrons are transferred to the current collector and the external circuit. By adding Poly(3-hexylthiophene-2,5-diyl) (P3HT), which is a conjugated p-type polymer, electron transport is further supported. At the same time, the band energies of P3HT hinder the hole movement to the current collector, which prevents electron-hole pairs from recombining. The accumulation of electrons at the anode and holes at the V_2O_5 site facilitate the deintercalation of Li^+ from the cathode, which enhances the measured electrochemical signal.

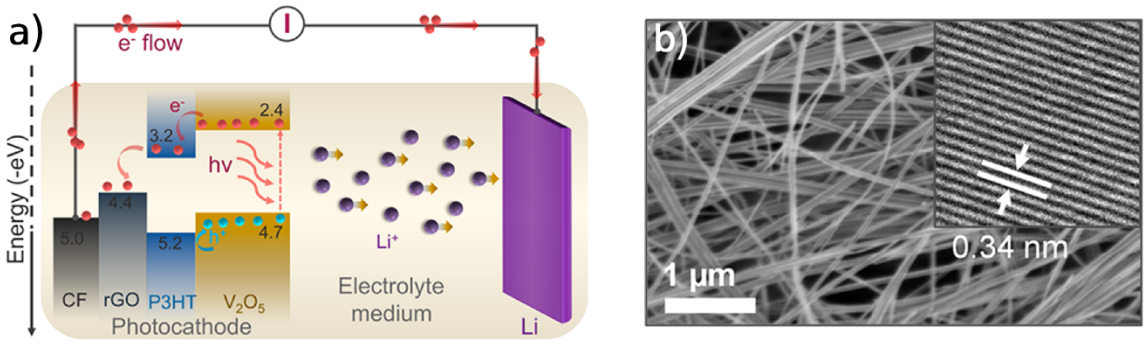


Figure 3.2: (a) Schematic illustration of the proposed photocharging mechanism of a V_2O_5-electrode with a P3HT-additive. (b) SEM-image of the V_2O_5 nanofibers, with a HRTEM image in the inset. Adapted from [11].

For the photoactive material, Boruah et al. chose 1D V_2O_5 nanofibers with a diameter of $20 - 50\,\mathrm{nm}$ (Fig. 3.2b) and an interplanar spacing of $\sim 0.34\,\mathrm{nm}$ (inset of Fig. 3.2b). Electrochemical characterization was performed under dark and illuminated conditions using a monochromatic light source ($\lambda \sim 455\,\mathrm{nm}$, intensity $\sim 12\,\mathrm{mW/cm^2}$), whose wavelength was chosen to match the absorption of V_2O_5. This ensured efficient photoexcitation of the cathode material. For in-situ illumination, the photocathode was placed in a CR2032 coin cell with a $\sim 7\,\mathrm{mm}$ diameter hole, which was mounted with a transparent glass window.

Cyclic voltammetry measurements performed by Boruah et al. within a potential window of $2 - 4\,\mathrm{V}$ showed that illumination increases the current density while preserving the redox peak positions, resulting in an overall enhancement of $\sim 30\,\%$

in the CV area (Fig. 3.3a). This improvement was attributed to an increase in the charge carrier density and enhanced diffusion kinetics of Li-ions under light exposure.

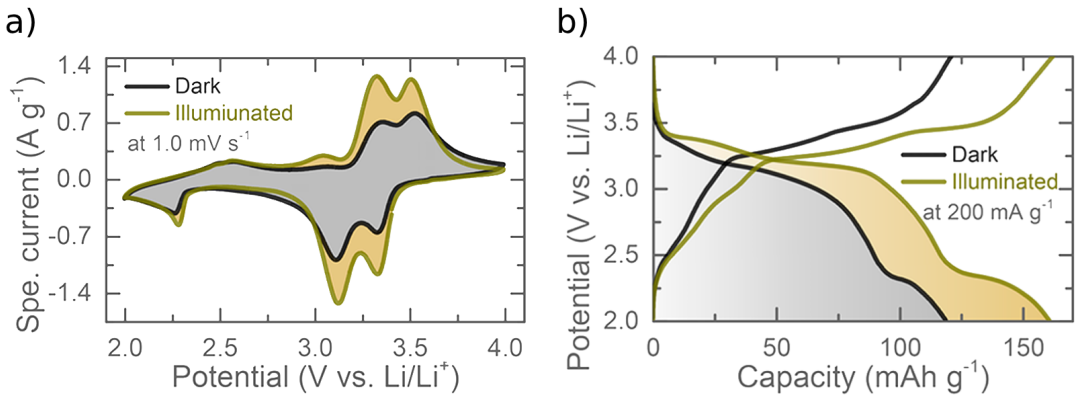


Figure 3.3: (a) CV-measurement of V_2O_5 (scan rate 1.0 mV/s) under dark and illuminated conditions. (b) GCPL-curves of V_2O_5 (seventh cycle) under dark and illuminated conditions at 200 mA/g. Both adapted from [11].

Galvanostatic charge-discharge measurements at a specific current of 200 mA/g demonstrated substantial enhancements of the capacity under illumination. Its value increased by over 36 % from $\sim$ 118 mA h/g to $\sim$ 161 mA h/g (Fig. 3.3b), which confirmed the positive impact of light in improving the electrochemical performance.

The study by Boruah et al. demonstrates photo-assisted electrochemistry in LIBs employing V_2O_5-based photocathodes. This is mainly attributed to light-induced charge carrier generation and separation mechanisms. Nevertheless, the potential contribution of photothermal effects to the observed improvements cannot be excluded, as a fully decoupled thermal analysis was not explicitly conducted. The study serves as an important reference point for the present work, which aims to systematically disentangle and quantify the respective contributions of bare photonic and photothermal effects under controlled conditions.

3.2 Setup for Temperature Measurements

To disentangle photonic and thermal light effects on the electrochemical performance of vanadium pentoxide, the temperature of the illuminated V_2O_5-electrode has to be measured in real time. For this purpose, a platinum (Pt) resistance temperature detector (RTD) is used, in this case a Pt1000 commercial temperature sensor (32208707 M222, Yageo Nexensos [57]). The RTD, measuring $2.3 \times 2.1 \times 0.9\,\mathrm{mm}^3$, is embedded into a coin cell and positioned in direct proximity to the electrode (see Fig. 3.4). To be able to measure the resistance, the leads of the thermometer are attached to a 35 µm thin copper (Cu) foil, which exits the coin cell but is thin enough to ensure that the cell is sealed airtight.

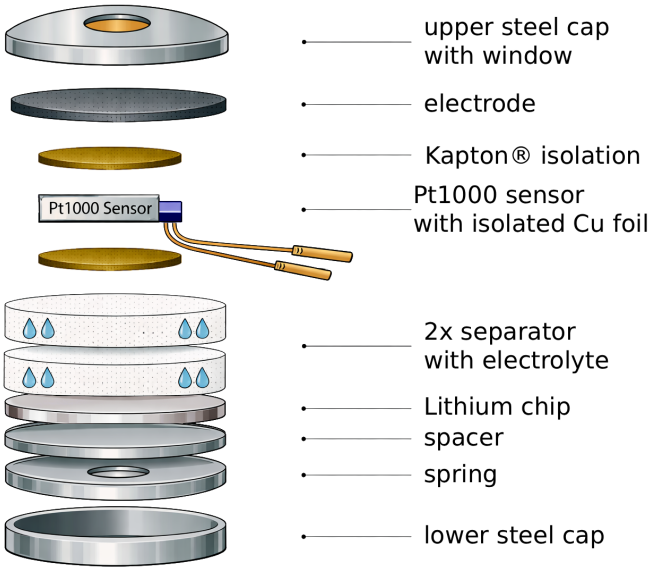


Figure 3.4: Schematic illustration of the embedded Pt1000 resistance thermometer for in-situ temperature measurement of an LIB coin cell half cell [75]. Through an isolating Kapton layer, the sensor has direct contact with the illuminated V_2O_5-electrode.

The Cu-foil, which is fabricated by CMC Klebetechnik GmbH [76], is isolated on both sides by a 50 µm thin Kapton-HN layer (Fig. 3.5). The isolating layer prevents direct contact between copper foil and steel case of the cell, which would otherwise cause a short circuit in the resistance measurement. To ensure that no part of the foil touches the steel cap, the Kapton isolation is applied with a ~ 0.5 mm overhang. Since the V_2O_5-electrode contains conductive carbon, direct contact with the Pt1000

sensor can also lead to a short circuit. To prevent this, Kapton isolation is attached to the sensor element, too. The fully assembled coin cell with the built-in Pt1000 thermometer is depicted in Fig. 3.5b. Through the protruding copper foil, the sensor resistance can be recorded with a multimeter (Keithley 2000) in real time. A self-written Python program (see Appendix A.1) is then used to read out the multimeter once every second and convert the measured resistance values into temperature.

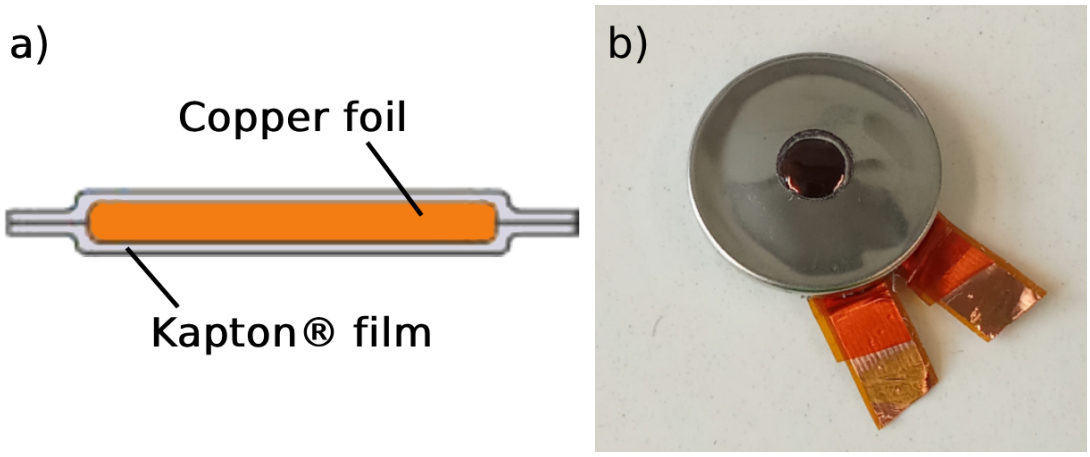


Figure 3.5: (a) Schematic cross section of the Kapton-isolated copper foil [76]. (b) Assembled LIB coin cell with embedded Pt1000 sensor.

Within the scope of this thesis, the relevant temperatures are between 20 and 30 °C. In this range, Pt1000 resistance thermometers exhibit an approximately linear resistance-temperature relationship, which can be described more accurately by the Callendar-van Dusen equation [77]:

$$R(T) = R_0 \left(1 + AT + BT^2\right), \tag{3.4}$$

where R(T) is the measured resistance at temperature T, R_0 the resistance at 0 °C (for a Pt1000, it is $R_0 = 1000\,\Omega$), $A = 3.9083 \cdot 10^{-3}\,°C^{-1}$ and $B = -5.775 \cdot 10^{-7}\,°C^{-2}$. This equation forms the basis of standardized RTD calibration according to IEC 60751 [78].

3.3 Synthesis and Physical Characterization

The Synthesis as well as XRD and SEM measurements on the V_2O_5 material studied in this work were carried out by the research team of Prof. Dr. Ewa Mijowska [1]. The sample was synthesized via a hydrothermal method. For that, 2 g of ammonium vanadate (V) NH_4VO_3 (99 %, Junsei Chemical Co., Ltd. Japan) were dispersed in 100 mL of deionized water and constantly stirred for 2 hours. The solution pH was then adjusted to 1 by drop-wise addition of nitric acid (HNO_3) (64.66 %, Duksan pure Chemical Co., Ltd. Korea). Finally, the solution was kept in a 150 mL Teflon coated stainless steel autoclave at 160 °C for 20 hours. Afterwards, the autoclave was cooled to room temperature and the solution was filtered and washed several times with ethanol and water. After drying the material at 100 °C, it was calcined at 600 °C for 4 hours in a high temperature furnace [79].

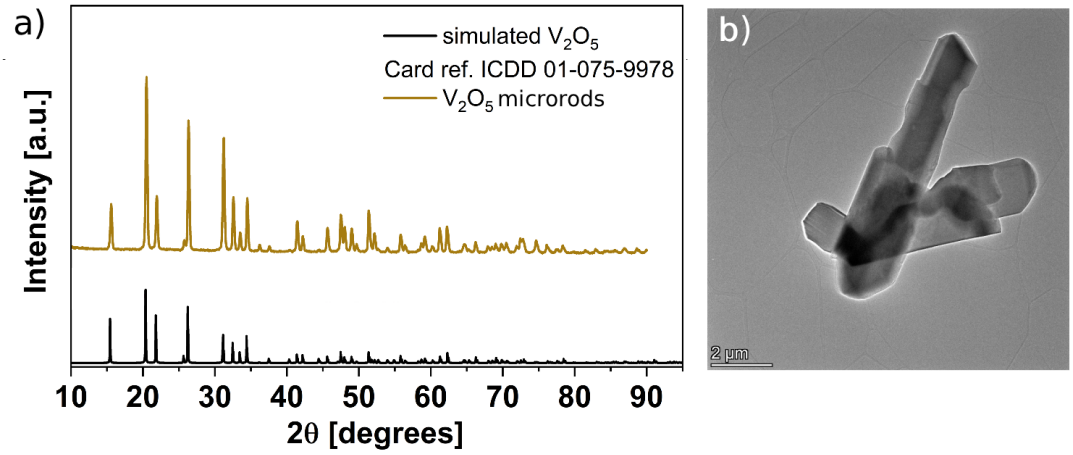


Figure 3.6: (a) XRD pattern of V_2O_5 microrods, confirming the orthorhombic crystal structure with space group *Pmmn*. (b) SEM-image of V_2O_5 microrods, showing diameters of up to $\sim 2\,\mu m$. XRD and SEM were recorded by the team of Prof. Dr. Ewa Mijowska from the Faculty of Chemical Technology and Engineering, ZUT (Szczecin, Poland) [79]

To confirm the crystallographic structure of the powdered V_2O_5-sample, XRD measurements were performed by the research team of Prof. Dr. Ewa Mijowska. As shown in Fig. 3.6a, the golden curve represents the measured diffraction pattern of the synthesized sample. It is in good agreement with the reference pattern from the ICDD database (ICDD No. 01-075-9978), displayed in black. The diffraction pattern

[1] Faculty of Chemical Technology and Engineering, West Pomeranian University of Technology (ZUT), Szczecin (Poland)

exhibits sharp and well-defined peaks, which are characteristic of an orthorhombic V_2O_5 crystal structure with a space group of *Pmmn*.

The SEM-measurement (Fig. 3.6b) reveals significant morphological differences of the synthesized V_2O_5 sample compared to the one from Boruah et al. (see Fig. 3.2b). Unlike the thin nanofibers in [11], our sample corresponds to V_2O_5 microrods, with a much larger diameter of several hundreds of nm to $1 - 2\,\mu m$. The reason for that could be differences in the thermal treatment of both samples. While the microrods were calcined at 600 °C, Boruah et al. obtained the nanofibers by annealing the sample at 400 °C. It was shown by other studies that lower annealing temperatures lead to smaller morphologies of V_2O_5 nanostructures [80].

3.4 Electrochemical Characterization

3.4.1 Electrochemical Behavior of V_2O_5 Cathodes in the Dark

In order to investigate the electrochemical behavior of V_2O_5, cyclic voltammetry (CV) and galvanostatic charge-discharge (GCPL) measurements were carried out in lithium-ion half-cells. As discussed in Section 2.3.1, V_2O_5-based working electrodes were prepared in accordance with Boruah et al. [11], using the same chemicals, weight ratios, current collector and electrolyte.

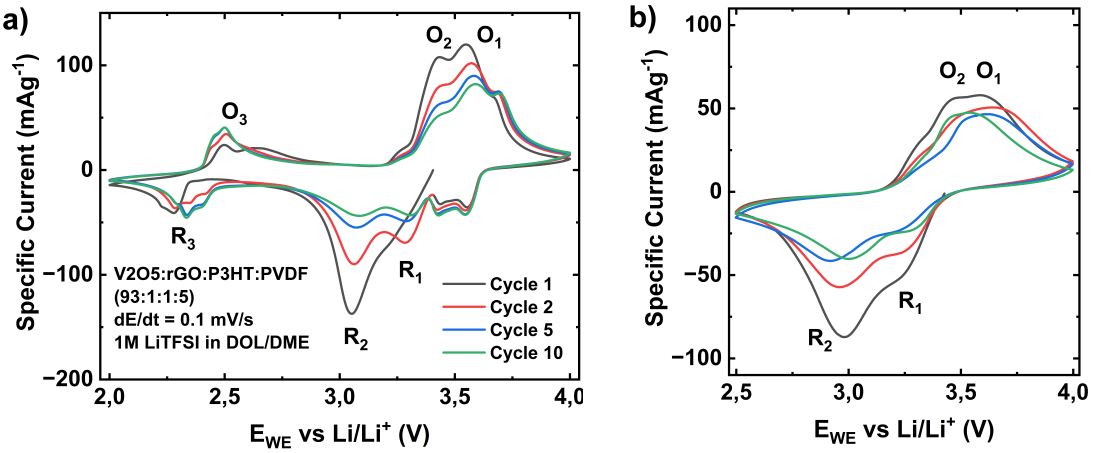


Figure 3.7: (a) CV of the V_2O_5-based electrode at $2 - 4\,V$, showing extra redox features: two reduction peaks near 3.5 V, reduction shoulders at $\sim 2.4\,V$, and oxidation shoulders around 2.4 V, 3.3 V and 3.7 V, attributed to defect state formation. (b) Cycling only between $2.5 - 4\,V$ (excluding the γ-phase transition) removes these additional features.

Fig. 3.7a shows a CV measurement of the composite electrode, recorded at a scan rate of 0.1 mV/s in the potential window of $2 - 4$ V vs Li/Li^+. The first, second, fifth and tenth cycle is shown in black, red, blue and green, respectively. The scan starts at an open circuit voltage of 3.41 V. In the first cycle, two reduction (R) peaks are visible at 3.05 V (R_2) and 2.28 V (R_3), which are accompanied by shoulders at 3.19 V and 2.23 V, respectively. Additionally, there are two reduction peaks in the high-voltage range at 3.44 V and 3.55 V. During the oxidation scan, there are peaks located at 2.51 V (O_3), 3.46 V (O_2) and 3.57 V (O_1), together with shoulders at 2.63 V, 3.27 V and 3.67 V. From the second cycle onward, a new reduction peak emerges at 3.28 V (R_1). In the low-voltage range, there are new shoulders at 2.35 V and 2.41 V. The oxidation shoulder at 2.63 V disappears from the second cycle onward, and a new shoulder appears at 2.45 V. In the high-voltage range, no significant changes occur. Starting from the fifth cycle, the peak R_3 shifts to 2.33 V, while the potential values for all other CV-features remain stable. The three prominent reduction (R_{1-3}) and oxidation peaks (O_{1-3}) are characteristic for the V_2O_5 phase transitions and correspond to Li^+ (de-)intercalation from the interlayer gaps of the 2-dimensional lattice [70]. The occurrence of additional CV features after initial lithiation could be attributed to a permanent structural change of the V_2O_5 lattice [81, 82, 83]. Over the 10 measured cycles, the potential values of the first two main redox couples R_1/O_1 and R_2/O_2, which are associated with the intercalation of the first Li-ion, remain stable. The shape of the voltammogram in the low voltage range changes after the first cycle: the reduction features move to higher voltages, while the oxidation peaks and shoulders shift to lower potential values. Such changes in peak positions indicate structural changes in the material during cycling [84]. According to reports, the phase transition of V_2O_5 into the γ-phase is not as reversible as the transitions into the ε- and δ-phases [85], which may explain the unusual behavior. Upon deep lithiation, defect states could be created, which show additional electrochemical activity. This activity manifests itself in the form of the extra peaks and shoulders observed in Fig. 3.7a.

Fig. 3.7b shows a cyclic voltammogram at the same scan rate of 0.1 mV/s, but in a smaller voltage range of $2.5 - 4$ V. Once again, the black, red, blue and green curves show the first, second, fifth and tenth cycle, respectively. In the first cycle (in black), a reduction peak is observable at 2.98 V (R_2), together with a shoulder at 3.20 V (R_1). In terms of oxidation, there are two flat peaks at 3.50 V (O_2) and 3.59 V (O_1), accompanied by a shoulder at 3.31 V. In the second cycle (red), the potential values

of the CV-features remain unchanged. The width of the oxidation peaks O_1 and O_2 increases, causing them to merge together. By the fifth cycle (blue), the peak separation of both redox couples R_1/O_1 and R_2/O_2 increases, with the potential values changing to 3.21 V (R_1) and 2.92 V (R_2). While it is impossible to deduce separate positions of the merged O_1 and O_2 peaks, one can observe their collective shift towards higher voltages. By the tenth cycle (green), the redox peaks have moved back towards each other, with the oxidation features falling to lower potential values, while R_1 and R_2 take on the voltages of 3.27 V and 3.01 V, respectively.

Excluding the γ-phase transition by cycling only down to 2.5 V causes most of the additional CV-features to vanish, indicating that less defect states are created. However, the appearance of an additional oxidation shoulder, as well as shifts in the redox peak potentials, suggests that permanent structural changes cannot be fully excluded. Additionally, the peaks have become broader and merged much more together, indicating worse kinetics of the sample. This unusual behavior could be attributed to imperfections in the preparation of the used electrode.

Fig. 3.8 shows the results of GCPL measurements on the V_2O_5-electrode, performed at a specific current of 200 mA/g in the voltage range of $2 - 4$ V. The measurement starts off at an open circuit voltage of 3.25 V, thereby skipping the first reduction plateau R_1. The initial charge capacity is 87.2 mA h/g (Fig. 3.8a), which corresponds to 29.7 % of the theoretical capacity for a 2 Li^+ intercalation. By the 100th cycle, it goes down to 64.8 mA h/g. The plateau O_1 accounts for approximately 41 % of the specific capacity in the initial cycle, while O_2 contributes $\sim$ 34 %. Therefore, O_1 and O_2 have the largest contribution to the capacity, which aligns with the CV observations (Fig. 3.7a). In the first cycle, the reduction plateaus are centered at 3.08 V (R_2) and 2.19 V (R_3), while oxidation occurs at 3.50 V (O_1), 3.37 V (O_2) and 2.60 V (O_3). From the second cycle onward, R_1 emerges at 3.32 V. By the 100th cycle, the plateaus have shifted to 3.30 V (R_1), 3.07 V (R_2) and 2.32 V (R_3) for the reduction, and 3.52 V (O_1), 3.39 V (O_2) and 2.45 V (O_3) for the oxidation. These results are consistent with the observations in cyclic voltammetry.

In the potential profile of the galvanostatic cycling (Fig. 3.8a), the characteristic three-step behavior of V_2O_5 can be seen, consisting of three reduction (R_{1-3}) and three oxidation plateaus (O_{1-3}). These correspond to the reversible V_2O_5-phase transitions (see Section 3.1) and are in accordance with the main CV-peaks in Fig. 3.7a. The rather poor capacity values could be the cause of the defect states created

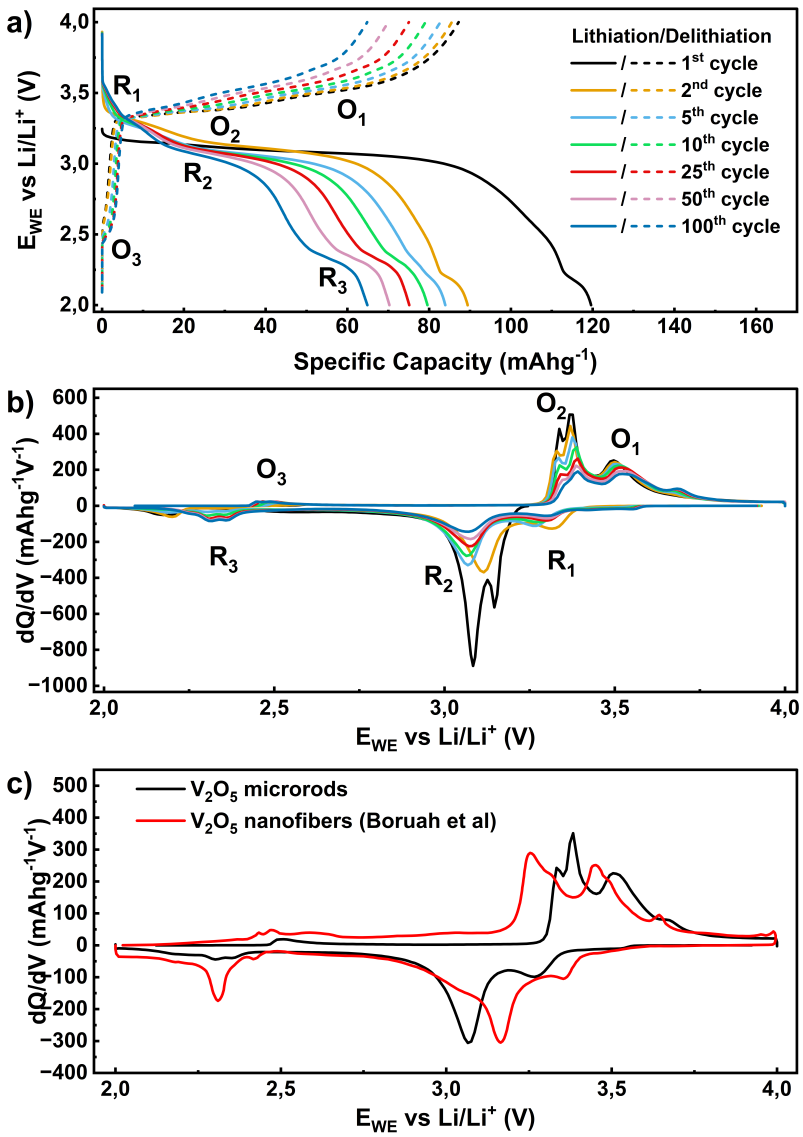


Figure 3.8: (a) GCPL-curves of V_2O_5-electrode with a current density of 200 mA/g. (b) Differential capacity (dQ/dV) plot showing the evolution from first to 100th cycle. (c) Direct comparison of seventh GCPL-cycle between V_2O_5 microrods (black) and nanofibers from [11] (red). R_{1-3} denote the three-step reduction of V_2O_5 from the α- to the γ-phase, with the corresponding oxidation O_{1-3} back to the α-phase.

upon deep discharge [86]. With subsequent cycling, the potential profile shows a continuous decline in the capacity values. This is often caused by a dissolution of the active material into the electrolyte [87], which in turn leads to less charge carriers being involved in the redox reactions. In the potential profile of the GCPL measurement, it is observed as a capacity decrease.

Plotting the derivative dQ/dV of the charge-discharge profiles (Fig. 3.8b) reveals that

only the first two redox couples R_1/O_1 and R_2/O_2 experience a capacity fade with subsequent cycling. The peaks R_3/O_3 as well as all additional features associated with the defect states show an increase in their capacity contribution. A possible explanation could be that with each new lithiation cycle, more defect states are created and their electrochemical signal gets enhanced. Since the γ-phase transition is associated with the severe structural changes occurring in the material, the third redox couple R_3/O_3 shows a similar behavior. Same qualitative observations can be made in Fig. 3.7a, where the intensities of the aforementioned peaks and shoulders show an increase with subsequent cycling.

Fig. 3.8c shows a direct comparison between the seventh GCPL cycle of the V_2O_5 microrods (in black) with the nanofibers from Boruah et al. (in red). After deducing the peak positions for both materials via Gaussian fitting, the corresponding redox potentials ($E_{1/2}$) and overpotentials (η) are calculated according to the formulas in Section 2.2.1. Table 3.1 summarizes the results:

		V_2O_5 microrods	**V_2O_5 nanofibers [11]**
$E_{1/2}$	R_1/O_1	(3.39 ± 0.06) V	(3.41 ± 0.04) V
	R_2/O_2	(3.23 ± 0.03) V	(3.21 ± 0.03) V
	R_3/O_3	(2.41 ± 0.04) V	(2.39 ± 0.03) V
η	R_1/O_1	(0.33 ± 0.11) V	(0.11 ± 0.08) V
	R_2/O_2	(0.31 ± 0.05) V	(0.10 ± 0.05) V
	R_3/O_3	(0.21 ± 0.07) V	(0.16 ± 0.06) V

Table 3.1: Comparison of redox potentials $E_{1/2}$ and corresponding overpotentials η for V_2O_5 microrods studied at hand and for the nanofibers from Boruah et al. [11].

While the redox potentials for both microrods and nanofibers are in good agreement within their respective uncertainties, the overpotentials are significantly lower for the reference study. This indicates that V_2O_5 microrods display worse Li^+ diffusion kinetics than the nanofibers from [11]. As already discussed in chapter 3.3, the studied microrods are significantly larger than the nanofibers. This means that their specific surface area is rather small compared to other morphologies, so that much less redox active sites are accessible at the surface of the crystals. Li-ions have to diffuse into the bulk of the material to carry out the redox reactions. V_2O_5 has a rather poor Li^+ diffusion coefficient of 1.7×10^{-12} to $5.8 \times 10^{-15} \mathrm{cm}^2/\mathrm{s}$, depending on the state of lithiation [88]. As a result, the movement of the Li-ions is slowed down. The ions experience higher resistances and a larger overpotential is needed to drive the redox reactions.

3.4.2 Light and Heat Effects on Cycling Behavior

To examine the separate effects of light and temperature on the electrochemical performance of V_2O_5, experiments were conducted on a windowed coin cell (see Section 2.3.3), similar to Boruah et al. [11]. Instead of using monochromatic light, the Xenon light source was set to white light in order to get a higher power output. To minimize unwanted heating, both an IR- and a UV-filter were placed between light source and coin cell. Unlike in Boruah et al., Kapton was used for the cell window instead of glass. It provides a larger heat capacity ($\sim 1.1\,\mathrm{J/(g\,°C)}$ for Kapton vs $\sim 0.9\,\mathrm{J/(g\,°C)}$ for glass) and lower thermal conductivity ($\sim 0.12 - 0.5\,\mathrm{W/(m\,K)}$ vs $\sim 0.8 - 1.0\,\mathrm{W/(m\,K)}$), making it harder to heat up the cell, which could reduce the influence of photo-thermal effects. Following the procedure described in Section 3.2, a Pt1000 temperature sensor was embedded inside the coin cell, in direct proximity to the V_2O_5 electrode. Figure 3.9 shows temperature measurements of the illuminated cell conducted every second. After switching on the lamp, the temperature increases by $\sim 3\,°\mathrm{C}$ from about $25\,°\mathrm{C}$ to $28.15\,°\mathrm{C}$ within $\sim 17\,\mathrm{min}$ (Fig. 3.9a). This shows that temperature driven effects do play a role upon illuminating the V_2O_5-electrode. Switching off the light source causes a return to room temperature within $\sim 10\,\mathrm{min}$ (Fig. 3.9b).

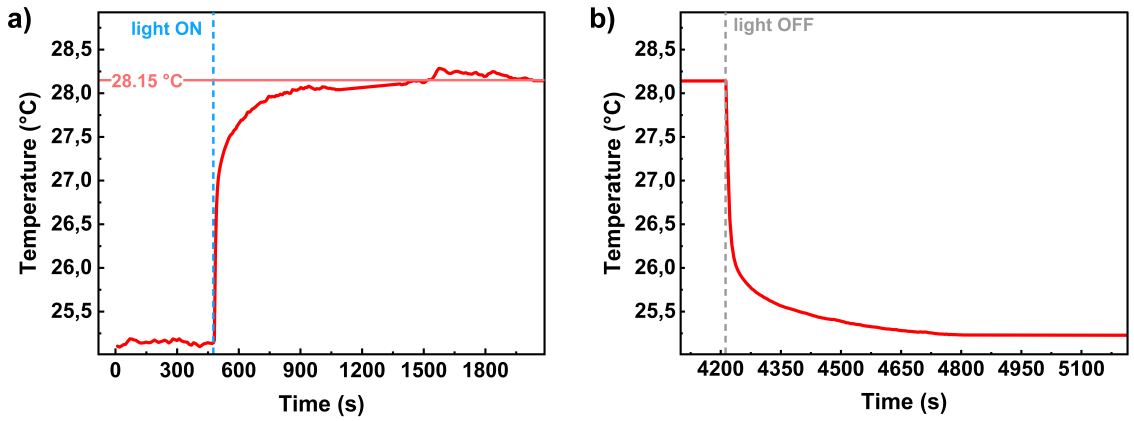


Figure 3.9: Pt1000 temperature measurement of V_2O_5 cell: (a) After turning on the light, the cell heats up by $\sim 3\,°\mathrm{C}$ within ~ 7 mins. (b) Switching off the illumination yields temperature decrease at the same pace.

To replicate the experimental findings of Boruah et al., cyclic voltammetry measurements were conducted at a scan rate of $1.0\,\mathrm{mV/s}$ in the voltage window $2 - 4\,\mathrm{V}$ (see Fig. 3.10). The V_2O_5-based electrodes were subjected to three different conditions: two non-illuminated measurements, one at room temperature ($\sim 25\,°\mathrm{C}$, gray) and

one at $\sim 30\,°C$ (red), as well as an illuminated cell at ambient temperature (blue). To disentangle any possible thermal effects that may occur during illumination and isolate them from photonic contributions, a dark reference measurement at 30 °C was carried out. For this, an incubator was used, where the ambient temperature of the cell was externally maintained throughout the measurement.

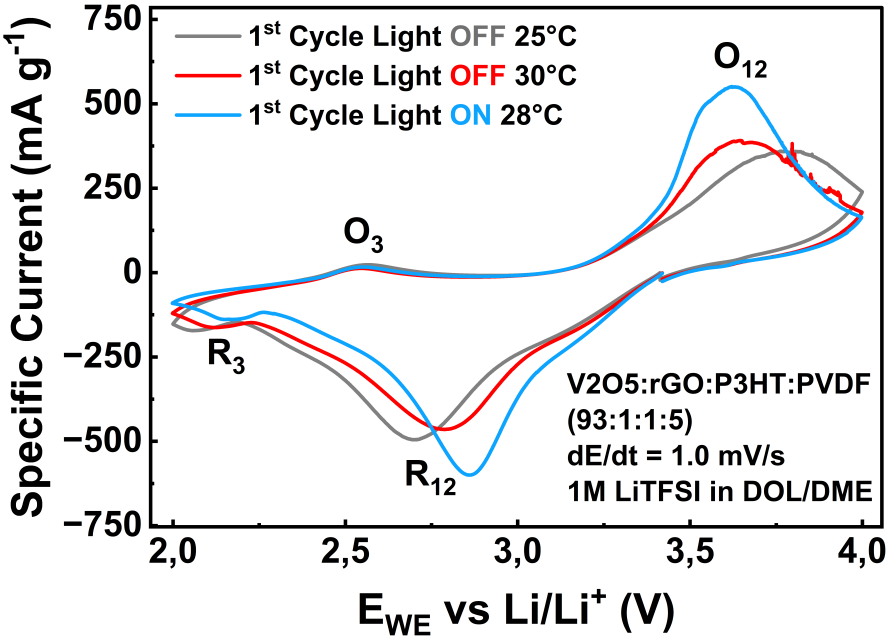


Figure 3.10: Cyclic voltammogram (first cycle) of V_2O_5-electrodes for light ON at 28 °C (blue), light OFF at 30 °C (red) and 25 °C (gray), measured at a scan rate of 1.0 mV/s.

For all three conditions, the first two reduction (R_1 and R_2) and oxidation peaks (O_1 and O_2) are found to merge into each other resulting in combined peaks (termed R_{12} and O_{12}). The third redox couple R_3/O_3 has a flattened shape compared to the measurement at 0.1 mV/s (Fig. 3.7a). The first cycle of the dark CV measurement at room temperature (gray curve) shows the reduction peaks R_{12} and R_3 at 2.70 V and 2.06 V, respectively. During the oxidation scan, peaks occur at 2.57 V (O_3) and 3.79 V (O_{12}). In the dark reference measurement at 30 °C (red curve), the reduction peaks are shifted towards higher potentials (2.79 V for R_{12} and 2.12 V for R_3), with the opposite behavior during oxidation (2.54 V for O_3 and 3.65 V for O_{12}). The illuminated condition (blue curve) has its peaks further shifted, with the reduction features being positioned at 2.86 V (R_{12}) and 2.17 V (R_3), while O_3 and O_{12} are found at 2.55 V and 3.62 V, respectively. Regarding the peak currents, there are almost no differences between the dark measurements at 25 °C and 30 °C. The clearest

change occurs in the light measurement for the redox couple R_{12}/O_{12}. The reduction peak R_{12} goes from $-497\,\mathrm{mA/g}$ (dark 25 °C) to $-600\,\mathrm{mA/g}$ (light 28 °C), while O_{12} increases from $359\,\mathrm{mA/g}$ (dark 25 °C) to $551\,\mathrm{mA/g}$ (light 28 °C).

The CV measurement shows similar results as discussed in Section 3.1.1 for Boruah et al.. Illumination with white light yields an increase in the peak current for the R_1/O_1 and R_2/O_2 redox couples (R_{12}/O_{12}) compared to the non-illuminated measurement at room temperature. This causes a larger swept CV area and indicates that more charge carriers are involved in the redox reactions. Additionally, the peaks of the light measurement shift towards each other, which suggests a decrease in overpotential and improvements in the kinetics. The non-illuminated reference measurement at 30 °C also shows reduced peak separation and overpotential, which is expected as temperature elevation speeds up Li^+ diffusion kinetics [89]. However, the overpotential is found to be still higher than for the illuminated cell, indicating a bare photonic contribution to the kinetics. Besides that, the peak current for both non-illuminated measurements is almost the same, which suggests that the light-induced increase in peak intensity has some contributions beyond photo-thermal effects. Comparing the results with the V_2O_5 nanofibers in Boruah et al., the microrods display significantly smaller peak currents. For dark conditions, the peaks take on values of up to $|I| \sim 497\,\mathrm{mA/g}$ (vs $|I| \sim 980\,\mathrm{mA/g}$ for the nanofibers). Upon illumination, the peak current rises up to $|I| \sim 600\,\mathrm{mA/g}$ (vs $|I| \sim 1500\,\mathrm{mA/g}$ in Boruah et al.). Additionally, the V_2O_5 microrods show overall wider CV-peaks. This causes the first two redox couples to merge enough into each other to be indistinguishable, making it hard to determine the actual peak positions. These phenomena indicate worse kinetics for the microrods, most probably caused by their large morphology (as discussed in Section 3.4.1). The increase in peak current caused by illumination is $\sim 53\,\%$ for the nanofibers, while the V_2O_5 microrods demonstrate a smaller photo-induced enhancement of only $\sim 21\,\%$. Light-induced effects play out mainly at the sample surface, and for the nanofibers, the specific surface area is larger (see Sections 3.3 and 3.4.1). This yields a higher illuminated fraction of the sample, which may cause the light effect to be more explicit.

Figures 3.11 a and b show galvanostatic charge-discharge potential profiles of a V_2O_5 electrode, measured at $200\,\mathrm{mA/g}$ under dark (gray) and illuminated (blue) conditions. The first five cycles were conducted without illumination, after which the light source was turned on for the subsequent five cycles. After cycle 10, the light source was switched off again. The potential profile shows the characteristic three-step be-

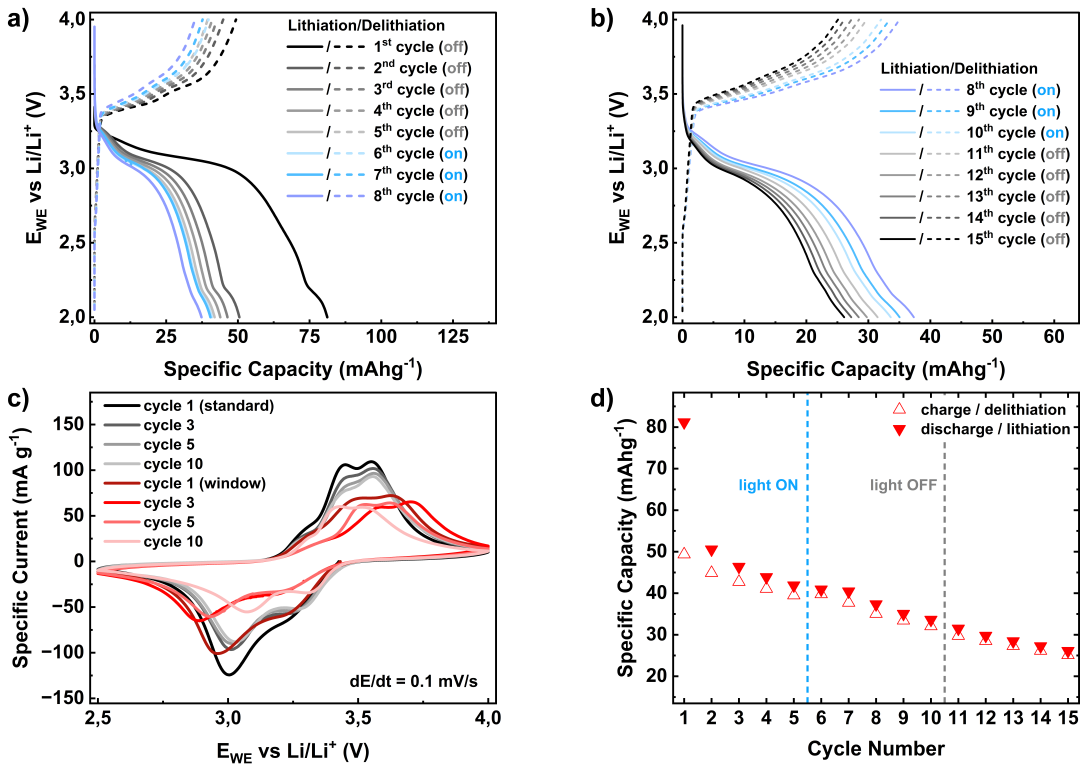


Figure 3.11: (a) Galvanostatic charge-discharge potential behavior of V_2O_5-electrode (200 mA/g) for light OFF (cycle $1-5$, gray) and light ON (cycle $6-8$, blue). (b) GCPL-behavior for light ON (cycle $8-10$, blue) and light OFF (cycle $11-15$, gray). (c) Cyclic voltammogram (scan rate 0.1 mV/s) for standard (gray) vs windowed (red) stainless steel cap, showing a reduced signal for the latter. (d) Specific capacity behavior for dark and illuminated conditions within the first 15 cycles, showing hardly any light-induced effect.

havior of V_2O_5, achieving $\sim$ 49.3 mA h/g in the first charge cycle, which is about 17 % of the theoretical capacity. This is even lower than in the GCPL results discussed in Section 3.4.1, which could stem from the fact that for light measurements, a windowed steel cap was used instead of a standard one. The Kapton window, which acts as an insulator, reduces the electrical contact between the electrode and the metallic housing, causing a reduced electrochemical signal. Such an influence of the window can be confirmed by comparative cyclic voltammetry measurements with and without the Kapton window, which is shown in Fig. 3.11c by the red and gray curves, respectively. The CV-measurement was conducted at a scan rate of 0.1 mV/s between 2.5 and 4 V. For all measured cycles, the windowed coin cell shows reduced peak currents by about $20-34$ %, indicating that less charge carriers are involved in the redox reactions. This could explain the additional dip in specific capacity.

Looking at the capacity profile of the GCPL measurement (Fig. 3.11d), one can see

a decline in C_{spec} caused by capacity fade (as discussed in Section 3.4.1), with the charge capacity going down from 49.3 mA h/g in the first cycle to 26.1 mA h/g in the 15th cycle. Switching on the light source after the fifth cycle slows down the capacity decline; however, from the eighth cycle onward, it regains its previous pace. Between the fifth and sixth cycles, the charge capacity shows a plateau with a slight increase of $\sim 0.7\,\%$, going from 39.5 to 39.8 mA h/g. This enhancement, however, is hardly resolvable and lies within the systematic error of the measurement, which is about 5 % [90]. Overall, the light effect on specific capacity can be regarded as negligible, unlike in Boruah et al., where illumination caused a capacity enhancement by about 36 % (see Section 3.1.1). The reason for that could again be morphology. The smaller specific surface area of V_2O_5 microrods causes any photo-induced effects to be much less pronounced. Other possible reasons could be differences in the experimental setup. Monochromatic blue light ($\lambda \sim 455$ nm) yields a larger photo-conversion efficiency ($\sim 2.6\,\%$) than white light ($\sim 0.22\,\%$) [11], meaning that a higher fraction of photons can produce electron-hole pairs. The window diameter in the reference study was 7 mm and thus 1 mm larger than for the coin cells used in this work, providing a larger illuminated area. Instead of using glass as in Boruah et al., a Kapton window was used. Although it may reduce photo-thermal influences on the measured signal, Kapton starts to transmit light only for wavelengths higher than ~ 550 nm, approaching 80 % only for wavelengths over 600 nm [91]. Thus, only a small margin of transmitted light can be absorbed by V_2O_5, which has a bandgap of ~ 2.2 eV ($\lambda \sim 564$ nm) [11]. Transparent glass, on the other hand, allows up to 90 % of visible light to pass through [92], causing more light to be absorbed by the active material. This further increases the efficiency difference of both setups in favor of Boruah et al..

Comparing Fig. 3.10 and 3.11, the photo-induced effect seems to be more visible in cyclic voltammetry than in galvanostatic cycling. CV- and GCPL-measurements are affected differently by non-equilibrium effects like interface charge transfer, with the shape of CV-curves showing a more sensitive reaction [93]. The potential sweep of 1.0 mV/s could be fast enough so that many bulk states cannot react in time. As a result, surface signals become more noticeable, yielding a stronger observed light effect for cyclic voltammetry.

3.4.3 In-situ Temperature Measurement in LIB Cells

To separate photonic and photo-thermal effects on the battery performance more precisely, all possible contributions to a temperature increase have to be considered. In addition to the light source, the inner cell temperature can also be altered by electrochemical processes. For more precise dark reference measurements at elevated temperatures, in-situ temperature recording of an illuminated electrode is essential. For that, a coin cell was built that included an embedded Pt1000 temperature sensor (according to the setup described in Section 3.2). For the following measurements, a more advanced experimental setup was developed, including an LED light source (MNWHLP1, ThorLabs) instead of a Xe-lamp. The light was focused onto the cell window using two aspherical condenser lenses, while an IR filter reduced the thermal load on the sample (more details in Section 2.3.3).

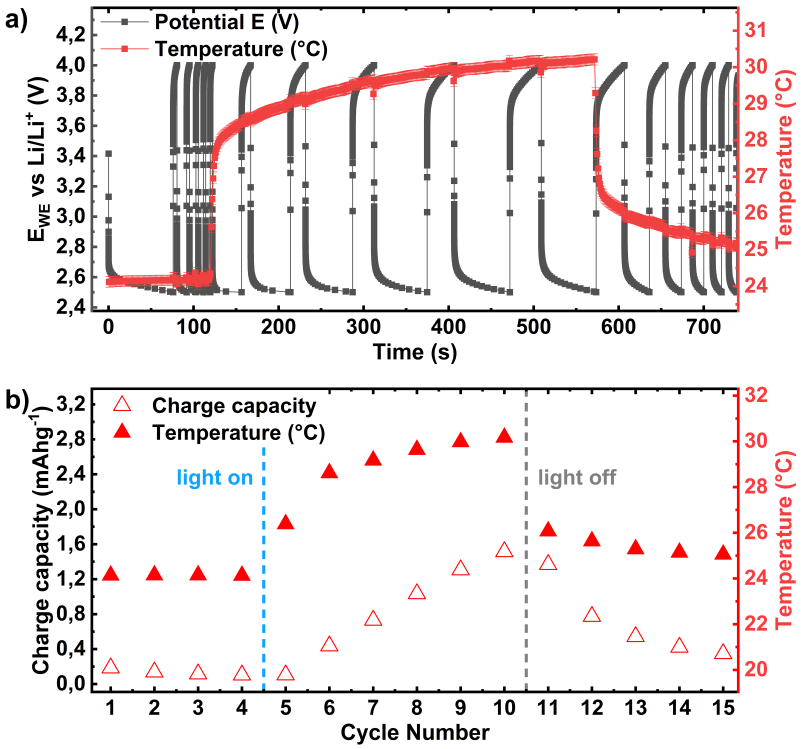


Figure 3.12: (a) GCPL-measurement (C-rate 0.5 C) showing the cell voltage profile over time (gray), together with in-situ temperature measurements (red) with a Pt1000 sensor. Illumination with LED yields a temperature increase by $\sim 6\,°C$, and a wider voltage profile. (b) Strong correlation between measured specific capacity values (white triangles) and temperature (red triangles). However, overall capacity values are negligibly small and reveal the hindering effect of the in-built Pt1000 sensor for electrochemical processes.

Figure 3.12 shows the results of a galvanostatic charge-discharge measurement, which was conducted in a voltage window of $2.5 - 4\,\mathrm{V}$ for 15 cycles. The experiment was performed at a C-rate of 0.5 C, which corresponds to a current of $942\,\mu\mathrm{A}$. The light source was switched on after the fourth cycle, and turned off again after cycle 10. This allows to clearly distinguish between dark and illuminated conditions.

Fig. 3.12a depicts the resulting potential profile. Here, the cell voltage (in gray) and the measured internal temperature (in red) are plotted against time. Under initial dark conditions, the first four charge-discharge cycles last $t_1 = 19\,\mathrm{s}$, $t_2 = 11\,\mathrm{s}$, $t_3 = 9\,\mathrm{s}$ and $t_1 = 8\,\mathrm{s}$, respectively. The internal temperature of the battery lies at $\sim 24\,^{\circ}\mathrm{C}$. Upon switching on illumination after the fourth cycle, the temperature increases to $30\,^{\circ}\mathrm{C}$ in about 9 min. Meanwhile, the voltage profile becomes wider. The fifth cycle goes on for 37 s, with the subsequent cycles increasing in duration from 57 s (cycle 6) to 101 s (cycle 10). After the tenth cycle, the light source was switched off again. As a result, the temperature decreases back to $\sim 25\,^{\circ}\mathrm{C}$ in about 3 min. This is accompanied by a narrowing of the potential profile. The cycling duration decreases from 63 s (cycle 11) to 21 s (cycle 15).

The Pt1000 in-situ temperature measurement shows that illumination with white LED light includes a significant heating by $\sim 6\,^{\circ}\mathrm{C}$. This enhances the kinetics of the charge carriers, causing more of them to participate in the (dis)charging cycles. As a result, the voltage profile becomes wider in correlation with the temperature rise. However, the profile doesn't show the characteristic three-step behavior of V_2O_5, which suggests that the active material wasn't properly probed in this measurement.

This can be additionally confirmed by looking at the capacity profile of the measurement (Fig. 3.12b). Here, the charge capacity (white triangles) and temperature (red triangles) are plotted against the cycle number. The initial charge capacity in the first cycle is $\sim 0.22\,\mathrm{mA\,h/g}$, which amounts to less than 0.1 % of the theoretical capacity. Switching on the light causes a rapid temperature increase in the following cycles, approaching $30\,^{\circ}\mathrm{C}$ by cycle 10. Meanwhile, the capacity value rises almost linearly and reaches $\sim 1.5\,\mathrm{mA\,h/g}$ by the tenth cycle. After switching off the LED at cycle 11, both temperature and capacity experience a sharp decline and approach their initial values. By the 15th cycle, the battery temperature reaches $25\,^{\circ}\mathrm{C}$, with the charge capacity being $0.35\,\mathrm{mA\,h/g}$.

The measured capacity values are far below the theoretical values associated with V_2O_5, making it unlikely that the observed electrochemical signal originates from

this material. This suggests that the Pt1000 resistance thermometer, which is placed right in between electrode and separator, acts as a barrier at the electrode-electrolyte interface and presents a physical obstacle to Li-ion diffusion. As a result, much fewer charge carriers can participate in the charge and discharge processes, significantly reducing the capacity and signal size.

As an alternative, the temperature of the electrode could also be measured in-situ via non-contact infrared (IR) thermometry. For that, an IR thermometer (Fluke 62 MAX [58]) was aimed at the cell window during illumination, while the measured temperature was logged every 30 seconds. For comparative purposes, the cell temperature was simultaneously monitored via an built-in Pt1000 sensor once per second. The results, which are depicted in Fig. 3.13a, show a significant discrepancy between both measurements. Before turning on the LED light source, the temperature measurements already differ by almost 2 °C. While the platinum sensor shows a temperature of ~ 25 °C in the interior of the half-cell, the IR thermometer measures 23.4 °C from the outside. A possible explanation to this could be that the outer cap is efficiently cooled by convection to ambient air, while the Pt1000 sensor measures the temperature within a thermally insulated environment inside the cell, which is not influenced by surface convection [94].

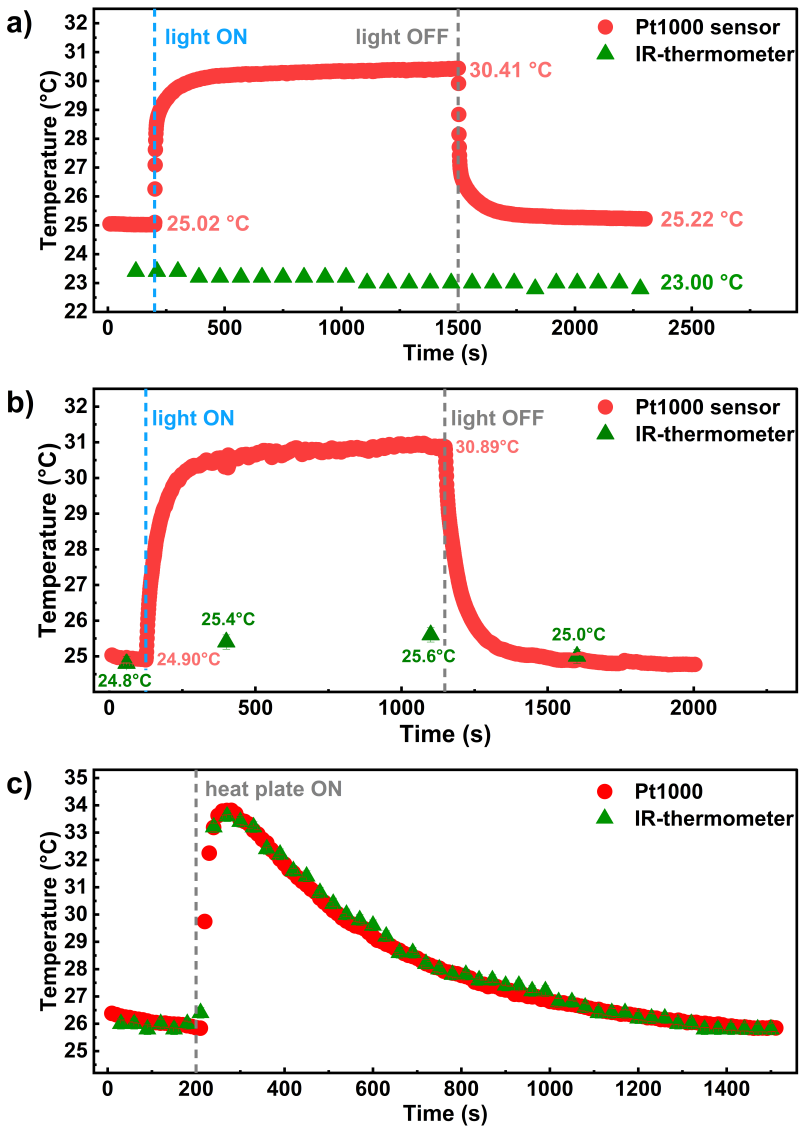


Figure 3.13: (a) Temperature measurement of illuminated V_2O_5-cell, once with an embedded Pt1000 resistance thermometer (red), and once via an IR thermometer (green) from above. (b) Measurement of an illuminated V_2O_5-electrode in an open cell. (c) Comparative measurement of a heat plate with both Pt1000- and IR thermometer.

Upon illumination, the Pt1000 sensor records a temperature increase to $\sim 30\,°C$ within $\sim 7\,min$. Switching the light off again yields a decrease in temperature to $\sim 25\,°C$ in $\sim 4\,min$. Meanwhile, the IR thermometer doesn't show any change throughout the entire measurement period and fluctuates between 23.4 and 22.8 °C. This discrepancy could be related to the surface conditions of the battery cell, more precisely its emissivity. It indicates how much radiation is emitted from the target object compared to blackbody radiation at the same temperature. Objects with

low emissivity, such as polished metals or shiny surfaces, represent a significant error source for IR thermometry [95]. Such materials emit less infrared radiation than materials with high emissivity at the same temperature, which can falsify the temperature measurement. Although Kapton has a rather high emissivity of 0.61 [96], the cell window itself could be too small for a sufficiently accurate measurement. The IR thermometer had to be held manually at a flat angle ($\sim 25 - 30°$) to bypass the IR filter (which was $\sim 1.5\,\text{cm}$ above the coin cell). This makes accidental measurements of the shiny stainless steel surface (with an emissivity of ~ 0.35 [97]) more probable, leading to false temperature values.

To circumvent this problem, the illuminated electrode was measured in an open cell, where all parts except for the upper windowed steel cap were removed. With that, the IR thermometer could be directly pointed onto the electrode from underneath. Figure 3.13b shows the results of the temperature readings (in green), together with a comparative Pt1000 measurement (red). Both Pt1000 sensor and the upper steel cap were attached from opposite sides to the V_2O_5 electrode using high vacuum grease (Dow Corning), which is assumed to provide good thermal coupling [98]. Unlike in the measurement with the fully assembled half-cell, the temperature readings of both Pt1000- and IR thermometer coincide here for dark conditions. Since both electrode and Pt1000 sensor aren't isolated from the environment anymore, it can be assumed that ambient air convection could have equal influence on both measurements. However, after switching on the light source, the temperature measurements are drifting apart again. While the Pt1000 sensor once again shows an increase of about 5 °C, the IR thermometer only records slight heating of 0.8 °C to 25.6 °C. Since the emissivity of both carbon felt mesh (typically 0.95 [99]) and V_2O_5 ($\sim 0.91 - 0.98$ [100]) is rather high, this discrepancy indicates possible deficiencies in the accuracy of the IR measurement.

Figure 3.13c shows comparative temperature measurements of both Pt1000- and IR thermometer on a heating plate. The platinum sensor was attached directly to the plate using adhesive tape. As one can see, both measurements show good agreement with each other, ruling out any functional defects in the temperature measurement of Pt1000- or IR thermometer. Instead, the discrepancy observed in Fig. 3.13a & b can be attributed to inaccuracies in the measurement setup for IR thermometry.

3.5 Conclusion and Outlook

Vanadium pentoxide (V_2O_5) electrodes have gained considerable attention for their light-induced enhancements in electrochemical performance, showing the potential to improve lithium-ion battery operation through photo-assisted mechanisms. Results from both cyclic voltammetry (CV) and galvanostatic cycling (GCPL) measurements show that illumination significantly improves reaction kinetics and specific capacity. However, these enhancements cannot be attributed exclusively to photonic effects, as localized heating introduces photo-thermal contributions. By means of temperature monitoring with Pt1000 sensors embedded inside modified coin cells, this study tries to disentangle both effects and reinterpret previously reported photo-assisted performance gains.

Illumination with a Xenon light source is found to increase the temperature of the V_2O_5 electrode by $\sim 3\,°C$. Cyclic voltammetry measurements display photo-enhanced electrochemical performance beyond possible thermal effects. Even compared to slightly elevated temperatures ($\sim 30\,°C$), the illuminated cell exhibits better reaction kinetics and higher peak currents. This suggests a direct interaction of light with the electronic structure of V_2O_5, creating electron-hole pairs and enhancing redox processes via efficient charge carrier separation. Galvanostatic cycling, however, couldn't confirm any light influence on specific capacity beyond systematic errors. This may be attributed to the morphology of the examined sample, whose structure is significantly larger (up to $2\,\mu m$) than in other comparative studies. As a result, the particles have a smaller specific area, which reduces any surface-sensitive light effects. The different dynamics of CV and GCPL measurements result in a more pronounced light-effect observation in cyclic voltammetry, where the chosen scan rate could be too high to allow sufficient probing of the bulk states. The use of Kapton as window material, as well as white light illumination instead of a fixed wavelength, could further minimize the overall photo-efficiency of the experimental setup.

When trying to conduct in-situ temperature measurements, the Pt1000 sensor was found to cause significant obstacles for Li-ion diffusion, acting as a physical barrier at the electrode-electrolyte interface. As a result, the measured capacity showed greatly reduced values and an absence of V_2O_5-characteristic voltage plateaus in the GCPL measurement. Comparative studies were performed using an infrared (IR) thermometer as a possible alternative solution. However, this resulted in substantial differences from the Pt1000 reading, suggesting that the measurement setup was still

too inaccurate for IR thermometry.

In summary, the enhanced electrochemical response of V_2O_5-based electrodes under illumination might arise from a combination of photonic and photo-thermal effects, with the thermal contribution being dominant under the investigated conditions. A genuine photonic effect is present but modest and strongly dependent on morphology and experimental design. To optimize the photo-enhancement in lithium-ion batteries, future work should focus on smaller V_2O_5 nanostructures with higher specific surface areas. In addition, emphasis should be placed on monochromatic illumination matched to the absorption spectrum, as well as on improved cell designs that enable reliable temperature control without interfering with the electrochemistry. This would further pave the way for broader practical adoption of photo-sensitive battery materials.

4. Azo-Based Electrode Materials

4.1 Organic Azo-Based Batteries: State of the Art

At present, commercial electrode materials for lithium-ion batteries are predominantly focused on inorganic compounds, such as lithium metal oxides and phosphates [36, 37]. However, the toxicity, high energy demand and pollutant emissions associated with the production of these inorganic electrodes have raised increasing concerns regarding resource use and environmental impact [101, 102, 18, 103]. In pursuit of higher sustainability and environmental-friendliness, organic species have emerged as promising alternatives for LIBs [104, 105, 106]. In particular, azo compounds have been reported as suitable active electrode materials due to their nitrogen center showing reversible redox activity [22, 23]. Beside abundant sources and low-cost, they possess high theoretical capacities and fast kinetics [24, 25]. This is ensured by two-electron redox reactions and $\pi-$conjugation of the azo groups (N = N) to aromatic groups (C_6H_6) [107]. Fig. 4.1a depicts the redox process of such a compound. Upon discharge, each azo group is reduced from the N = N double bond to the twice negatively charged N − N moiety, which associates the binding of two Li-ions [108, 107]. During charging, the reverse process happens. Each azo group contains a delocalized π bond (overlap of nitrogen p-orbitals) whose low-lying antibonding π^* orbital can accept electrons. This allows the group to be reduced without immediately breaking the N − N bond [109], which enables reversible redox cycling. One of the key molecular models to study azo redox mechanisms in LIBs is azobenzene [107], which has a chemically simple and well-defined model system. It consists of two aromatic benzene rings linked by an azo group (see Fig. 4.1b). The structure of the benzene rings, where p-orbitals overlap continuously across alternating single and double bonds, extends the π-conjugation of the electrons across the whole molecule [110]. This minimizes internal resistance and supports fast kinetics and high-rate capability [111]. Azobenzene provides a considerable theoretical capacity of $\sim 290\,\mathrm{mA\,h/g}$ [112].

It was discovered that azo compounds, which can be electrochemically reduced from nitro composites, i.e. molecules with a nitro group (NO_2), display superior electrochemical performance in LIBs [113]. Fig. 4.1c shows the reaction mechanism of

nitro-based organic materials. In the first lithiation cycle, the crystalline nitro compound reduces into an amorphous azo species, which then can undergo reversible redox reactions with Li-ions through the nitrogen center [113]. This irreversible conversion of nitro- into azo group features more than two electron redox reactions per functional group, yielding overall higher initial discharge capacities.

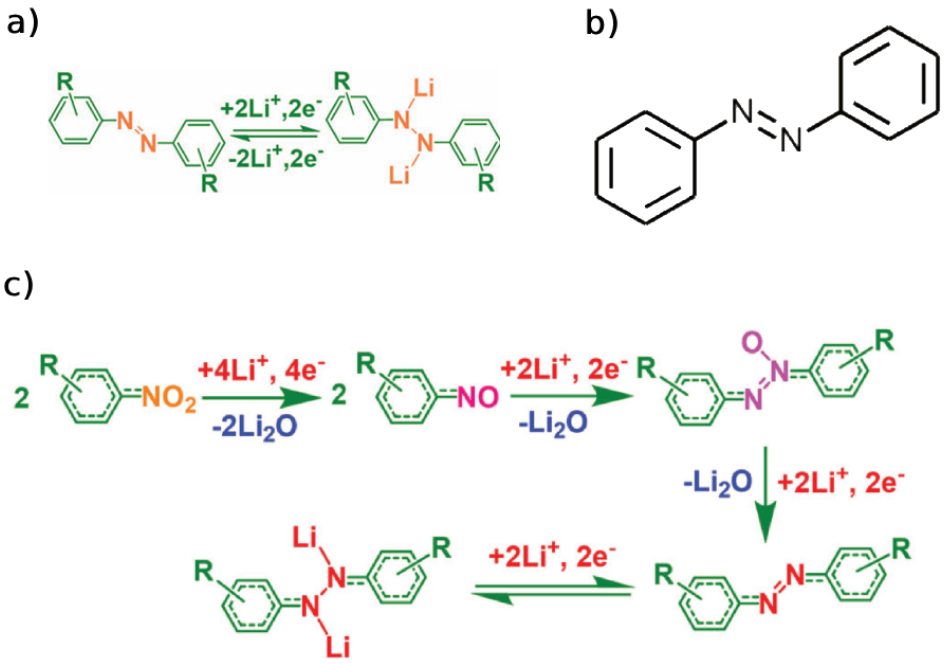


Figure 4.1: (a) Reversible two-electron redox reaction of an azo compound [108]. (b) Structural formula of azobenzene [107]. (c) Reaction mechanism of nitro-based organic compounds, comprising an irreversible reduction of the nitro group into the N = N linkage, and subsequent reversible redox reaction of the azo moiety [113].

A representative example of this electrochemical behavior is provided by 4-nitrobenzoic acid lithium salt (NBALS), as shown in Fig. 4.2 for a voltage window of $1.5 - 2.5\,\mathrm{V}$ [113]. For the electrolyte, 7 M LiTFSI in DOL/DME (volume ratio 1:1) was used. In Figure 4.2a, a cyclic voltammogram is shown, where two reduction peaks occur during the initial lithiation cycle. The first peak at 2.25 V can be attributed to the irreversible six-electron reduction of the nitro into the azo group [113]. The second peak at 2.0 V corresponds to the lithiation of the N = N double bond into the N − N moiety. Upon initial oxidation, the azo group is reversibly delithiated back to N = N, forming a peak at $\sim 2.2\,\mathrm{V}$. In the following cycles, one pair of redox peaks is observed, which corresponds to the redox-activity of the azo group [113].

By the fifth cycle, the reduction and oxidation reaction is centered at $E_R \sim 1.9\,V$ and $E_O \sim 2.1\,V$, respectively. This yields a redox potential of $E_{1/2} \sim 2.0\,V$. Looking at the galvanostatic cycling behavior of NBALS at the C-rate of 0.5 C (Fig. 4.2b), the irreversible reaction of the nitro group yields a short plateau at 2.35 V and a wide plateau-like feature at 1.90 V [113]. This results in a large initial discharge capacity of $\sim 550\,mA\,h/g$ [107]. In the second cycle, the discharge capacity falls to $\sim 220\,mA\,h/g$, as the first plateau at 2.35 V vanishes. Hence, this plateau can be associated with the irreversible CV-peak in the first cycle (Fig. 4.2a).

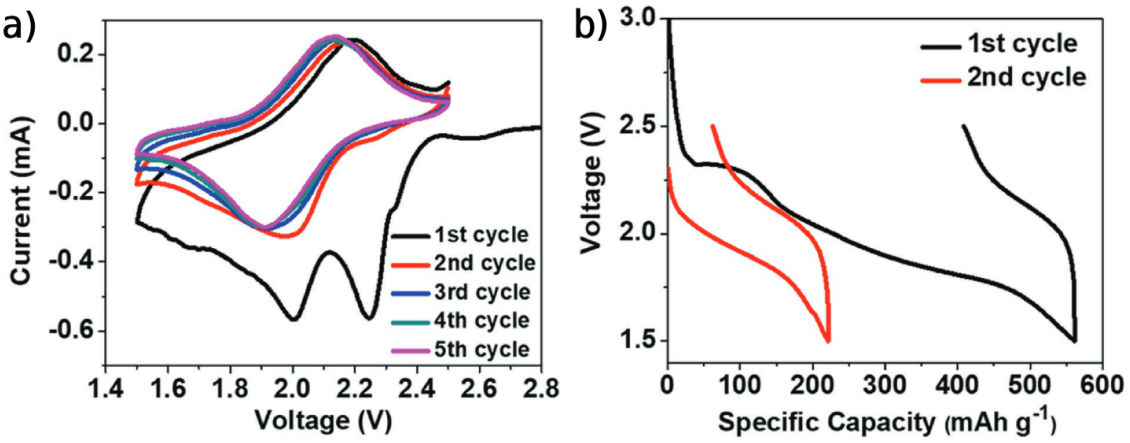


Figure 4.2: Electrochemical behavior of NBALS in lithium-ion batteries in the potential window of $1.5 - 2.5\,V$, with 7 M LiTFSI in DOL/DME as the electrolyte. (a) Cyclic voltammograms at a scan rate of $0.1\,mV/s$, showing two initial reduction peaks, corresponding to the irreversible conversion of nitro- into azo group and subsequent reversible lithiation of the N = N double bond. (b) Galvanostatic charge-discharge curves conducted at a C-rate of 0.5 C, showing a large irreversible lithiation capacity of $\sim 550\,mA\,h/g$ in the first cycle. Adapted from [113].

The usefulness of organic compounds is typically restricted due to their high solubility in electrolytes, which causes capacity degradation and limits their application as high-performance active electrode materials [26, 27]. Within this context, organic azo-based polymers present a promising solution. They possess extended conjugated structures, higher molecular weight and stronger inter-molecular forces, resulting in a cross-linked polymer network that makes them much more insoluble in electrolytes [28, 114, 115]. The polymers can be designed to exhibit a large surface area. This could reduce the diffusion paths of charge carriers and as a result, enhance the redox activity and kinetics [116]. Moreover, the highly cross-linked and insoluble polymer network ensures exceptional chemical and electrochemical stabil-

ity, enhancing the cycling performance [117]. Considering these advantages, a range of conjugated azo-based polymers with different structures and functions have been tested as electrodes for LIBs. For instance, Wu et al. investigated azo-linked covalent triazine-based frameworks (Azo-CTF), which are 3-dimensional frameworks made of azo (N = N) and triazine (C_3N_3) groups [118]. They exhibited a capacity retention of 89.1 % after 5000 cycles, as well as a high power density of 4253 W/kg. Yu et al. studied the electrochemical performance of Azo-BT, which is a π-conjugated microporous polymer (CMP) [119]. Due to its porous structure facilitating the Li-ion movement, it displayed a high reversible capacity of 2332.8 mA h/g at 100 mA/g. Moreover, the polymer achieved astonishing rate capabilities, with the capacity retaining 1034.4 mA h/g after 1000 cycles at 2000 mA/g.

In this work, the electrochemical performance of novel azo-based polymers will be investigated by means of cyclic voltammetry (CV) and galvanostatic charge-discharge cycling (GCPL). In addition to polymers linked by simple azo groups, novel compounds incorporating nitro moieties into the polymer structure will be investigated. Furthermore, the impact of various structural additives on the polymer's cycling performance will be systematically evaluated.

4.2 Synthesis of Organic Azo-Compounds

All organic azo compounds investigated in this work were synthesized by Christian Delavier[1]. Two kinds of organic polymers were prepared: PEGDA-crosslinked acrylate polymers with azo (N = N) and nitro (NO_2) pendant groups. The latter can also function as an azo group after successful irreversible reduction (see Section 4.1).

For the azo-linked polymers, the active monomer is P-N Boc Aniline ($C_{11}H_{15}NO_2$, molecular weight M_W = 193.2 g/mol), which is the building block of the molecule that contains the electrochemically active azo group. It was dissolved and homogenized with a weight percentage of 42.4 wt % in Dimethylacetamide (DMAc, 40.9 wt %), together with 15.6 wt % of Poly(ethylenglycol)diacrylate (PEGDA575, M_W = 575 g/mol) acting as a crosslinker and 1.1 wt % of Bis(2,4,6-trimethylbenzoyl)-phenylphosphine oxide (BAPO, M_W = 418.5 g/mol) being the photoinitiator. The homogenization process was carried out in an ultrasonic bath for 45 min. The crosslinker molecules contain two polymerizable groups, which leads to covalent link-

[1] Institute for Molecular Engineering and Advanced Materials (IMSEAM), Heidelberg University

age of the linear polymer chains afforded by the active monomer molecules, thus forming a polymer network. This provides mechanical stability, reduced solubility and can support ionic conductivity [120]. Under UV-illumination, the photoinitiator releases radicals that break the acrylate double bonds present in the crosslinker and active monomer, and initiate polymerization [121]. In this case, photopolymerization is achieved through the use of a Digital Light Processing (DLP) 3D printer (LED wavelength $\lambda_{\mathrm{LED}} = 405\,\mathrm{nm}$). After postprocessing with isopropanol, the raw material is obtained (Fig. 4.3a) consisting of the active monomer and crosslinker in a molar ratio of 6 : 1. Treatment with sodium nitrite ($NaNO_2$) and hydrochloric acid (HCl) (step 1) converts this into the baseline material (Fig. 4.3b). In step 2, coupling with various aromatic side groups introduces azo (N = N) linkages, resulting in the final polymer structure (Fig. 4.3c).

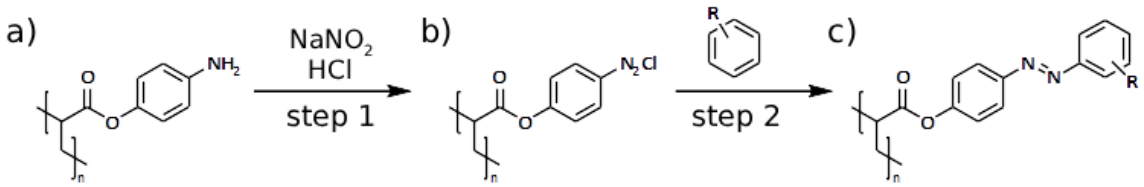


Figure 4.3: Synthesis steps of novel azo polymers, conducted by Christian Delavier from IMSEAM, Heidelberg University. Treatment of the printed precursor with $NaNO_2$/HCl (step 1) and coupling with substituted aromatic compounds (step 2) forms N = N linkages, yielding the final azo-functionalized polymer structure [122].

In this work, materials with the side groups Phenol (C_6H_5OH), Anisole (C_7H_8O) and sodium 3-hydroxynaphtalene-2,7-disulfonate ($C_{10}H_6Na_2O_7S_2$, also called Disodium napthol) are used, yielding the correspondingly named novel azo polymers (see Fig. 4.4b – d). The baseline material can also undergo self-coupling to form azo linkages. If step 2 is omitted, the resulting product is referred to as the Blank material (Fig. 4.4a). The effective molecular weights of the compounds are 323 g/mol (Blank), 268.27 g/mol (Phenol), 282.30 g/mol (Anisole) and 522.41 g/mol (Disodium napthol). Using (2.5), the theoretical specific capacities are calculated as 165.95 mA h/g, 199.81 mA h/g, 189.88 mA h/g and 102.61 mA h/g, respectively.

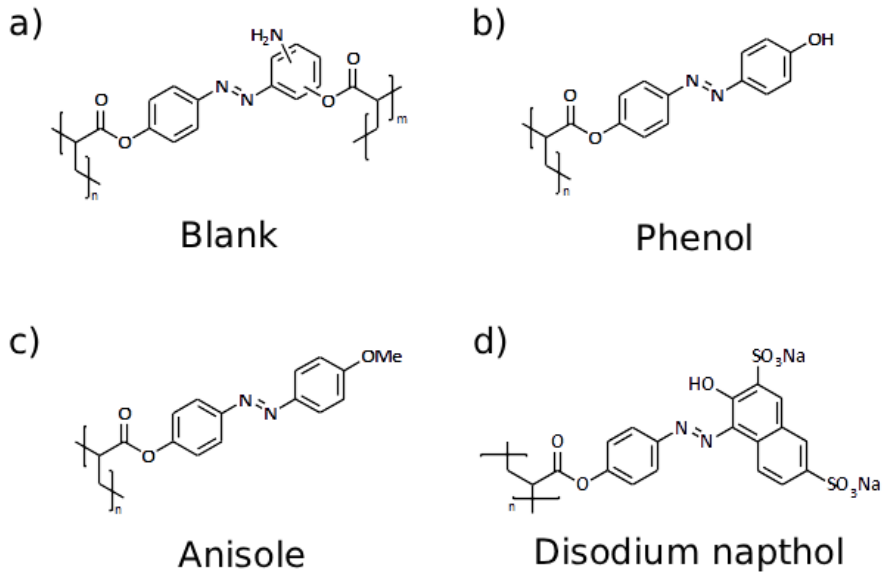


Figure 4.4: Azo-linked polymers Blank (a), Phenol (b), Anisole (c) and Disodium napthol (d), synthesized by Christian Delavier from IMSEAM, Heidelberg University [122].

In addition to azo-linked polymers, compounds with nitro (NO_2) pendant groups were also prepared. Here, bis(4-methoxybenzoyl)diethylgermanium (Ivocerin, $C_{20}H_{24}GeO_4$, $M_W = 401.04\,g/mol$) acted as the photoinitiator ($\lambda_{LED} = 460\,nm$). For the active monomer, P-NO_2PhenAc ($C_9H_7NO_4$, $M_W = 193.16\,g/mol$) and P-NO2PhenHexAc ($C_{15}H_{19}NO_5$, $M_W = 293.32\,g/mol$) were used to obtain the nitro polymers Azo-018 (Fig. 4.5a) and Azo-019 (Fig. 4.5b), respectively. Both compounds consist of 88 % active monomer and 12 % crosslinker (PEGDA575).

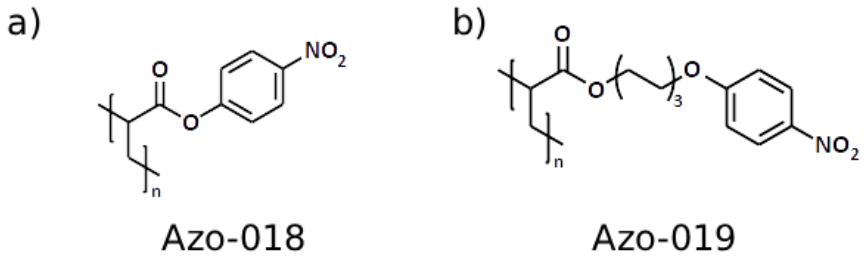


Figure 4.5: Nitro-based compounds Azo-018 (a) and Azo-019 comprising an additional alkyl spacer (b), synthesized by Christian Delavier from IMSEAM, Heidelberg University [122].

With molecular masses of $M_W \approx 239\,g/mol$ (Azo-018) and $M_W \approx 327\,g/mol$ (Azo-

019), the theoretical capacities of the compounds are calculated as $C_{th}^{Azo\text{-}018} = 224.28\,mA\,h/g$ and $C_{th}^{Azo\text{-}019} = 163.92\,mA\,h/g$. In Azo-018, the nitrophenyl group (benzene ring carrying the NO_2 substituent) is directly connected to the polymer backbone through a short ester linkage, whereas in Azo-019 it is separated from the backbone by a longer, flexible alkyl spacer.

After DLP 3D printing, the azo- and nitro-based compounds are acquired in the form of macroscopic flakes and stripes. For electrode preparation, the material is milled manually in a mortar for one hour to obtain a fine powder.

4.3 Electrochemical Characterization

4.3.1 Carbon Black Reference Measurement

Conductive Carbon Black (CB) is added to the working electrode to enhance electronic conductivity, enabling efficient charge transport and better electrical access to redox active sites [123]. Additionally, Li-ions can intercalate into CB, contributing to the measured specific capacity, as well as to redox features in CV and GCPL profiles within the potential window of $0 - 1.5\,V$. In this work, novel azo-linked polymers will be investigated as anode materials in the voltage range $0.01 - 3\,V$ based on studies on similar azo structures in the literature [107]. Since this range includes the electrochemical response of Carbon Black, its contribution has to be also considered. Therefore, reference CV and GCPL measurements were performed. The electrodes for this purpose consist of CB and PVDF in a mass ratio of 85 : 15.

Fig. 4.6a shows a blank cyclic voltammetry measurement performed at a scan rate of $0.1\,mV/s$ in the voltage range $0.01 - 3\,V$. The first, second, fifth and tenth (dis)charge scan is displayed in black, red, blue and green, respectively. In the first discharge cycle, three distinct reduction peaks occur at $R_1 = 0.80\,V$, $R_{SEI} = 0.42\,V$ and $R_2 = 0.01\,V$. During the first charge scan, two oxidation peaks O_1 and O_2 can be observed at $0.93\,V$ and $0.18\,V$, respectively, as well as a peak O_3 at $2.81\,V$. From the second cycle onward, the reduction feature R_{SEI} disappears.

The vanishing of the R_{SEI} peak after the first cycle is characteristic of an irreversible process. In this case, it can be linked to the formation of a solid electrolyte interface (SEI) layer, which is a stable passivation layer forming due to the interaction between electrode and electrolyte [124, 125]. The redox couples R_1 / O_1 and R_2 / O_2 can be

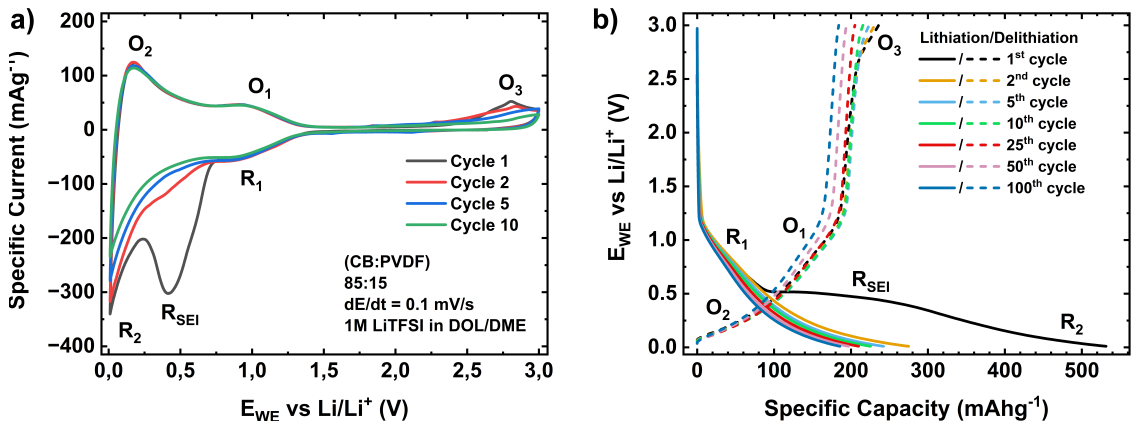


Figure 4.6: (a) Cyclic voltammetry (CV) of Carbon Black recorded at a scan rate of 0.1 mV/s. (b) Potential profile of Carbon Black, obtained from GCPL measurements at a specific current of 200 mA/g in the voltage window $0.01 - 3$ V.

attributed to the intercalation processes of Li-ions into Carbon Black [126]. Meanwhile, the third oxidation peak O_3 at high potentials doesn't have a corresponding reduction feature. It could result from oxidative decomposition of the ether-based solvents DOL and DME, which may occur at higher voltages [127]. The decomposition is catalyzed at the high-surface-area carbon black interface, where solvent oxidation and formation of oxidized interfacial products occur without a reversible redox couple [128, 129].

Fig. 4.6b depicts a GCPL measurement of Carbon Black at 200 mA/g between 0.01 and 3 V. The initial discharge capacity of 531 mA h/g drops after the first cycle and stabilizes at approximately 200 mA h/g from cycle 25 onward. A distinct reduction peak R_{SEI} occurs around 0.47 V in the first discharge cycle, as well as an onset of a second plateau R_2 at 0.01 V. Subsequent oxidation shows plateaus at ~ 0.2 V (O_2), ~ 0.9 V (O_1) and ~ 2.9 V (O_3), reaching a charge capacity of 235 mA h/g. In the second discharge cycle, the specific capacity falls to 274 mA h/g, as the reduction plateau R_{SEI} vanishes. During the subsequent cycles, both charge and discharge capacities gradually decrease. By the 100th cycle, they reach the values 184 mA h/g and 186 mA h/g, respectively. Overall, the galvanostatic cycling measurement is in good agreement with the CV results.

4.3.2 Novel Azo Compounds

To evaluate the electrochemical activity of the novel azo polymers Blank, Phenol, Anisole and Disodium napthol (see Fig. 4.4) as potential anode materials for LIBs, the compounds were manually milled and mixed at a weight fraction of 60 wt % together with Carbon Black (30 wt %) and PVDF binder (10 wt %), before disperging the mixture in NMP. The resulting slurry was coated onto copper meshes, and initial experiments were conducted using the electrolyte 1 M LiTFSI in 1,3-Diloxane (DOL) and Dimethoxyethane (DME) in a 1:1 volume ratio.

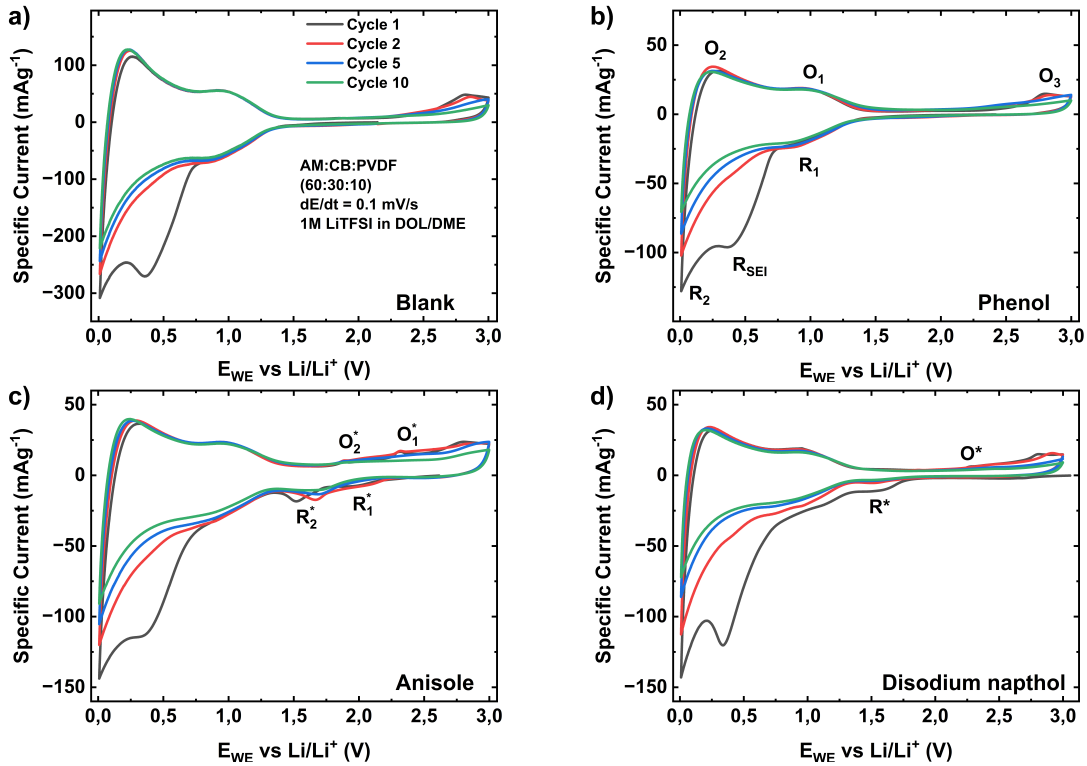


Figure 4.7: Cyclic voltammetry of the azo compounds Blank (a), Phenol (b), Anisole (c) and Disodium napthol (d), recorded at a scan rate of 0.1 mV/s in the voltage range 0.01 − 3 V.

Fig. 4.7 shows cyclic voltammograms of Blank (a), Phenol (b), Anisole (c) and Disodium napthol (d), recorded at a scan rate of 0.1 mV/s within the potential window of 0.01 − 3 V. The black, red, blue and green curves display the first, second, fifth and tenth cycles, respectively. After a resting time of ∼ 24 h, the OCV voltages of the materials were 2.15 V (Blank), 2.24 V (Phenol), 2.62 V (Anisole) and 3.06 V (Disodium napthol). The recorded CV-profiles of the azo compounds display very similar features. In the first lithiation cycle (in black), the materials show three

distinct reduction peaks within the potential window $0 - 1\,\mathrm{V}$. The first one, R_1, sits at around 1 V for all four compounds. The second one, R_{SEI}, is positioned at 0.36 V (Blank), 0.41 V (Phenol), 0.32 V (Anisole) and 0.34 V (Disodium napthol). Finally, all materials show a reduction peak R_2 at 0.01 V. During initial delithiation, three oxidation peaks can be observed. O_1 and O_2 emerge in the low-voltage range at $\sim 0.2\,\mathrm{V}$ and $\sim 0.9\,\mathrm{V}$, respectively, while O_3 is positioned around the upper voltage limit of 3 V. In the second cycle (in red), the reduction peak R_{SEI} vanishes. From the fifth cycle (in blue) onward, the oxidation feature O_3 shifts beyond 3 V. These features behave very similarly for all four azo compounds. Beside that, Anisole shows two additional small redox couples R_1^*/O_1^* and R_2^*/O_2^*, positioned at $R_1^* = 1.95\,\mathrm{V}$, $O_1^* = 2.32\,\mathrm{V}$, $R_2^* = 1.52\,\mathrm{V}$ and $O_2^* = 1.89\,\mathrm{V}$ in the initial cycle. In the subsequent cycles, the peak R_2^* moves to 1.67 V (cycle 2), 1.70 V (cycle 5) and 1.72 V (cycle 10), while O_2^* retains its position. The first redox couple R_1^*/O_1^* disappears after the second cycle, with R_2^*/O_2^* showing a strong flattening, too. Similarly, Disodium napthol exhibits an additional reduction ($R^* = 1.46\,\mathrm{V}$) and oxidation feature ($O^* = 2.29\,\mathrm{V}$) in the initial cycle, which, however, disappear in the subsequent cycles.

The differences in OCV observed for the various azo compounds could be attributed to their distinct chemical structures and side groups, which may modify the electronic environment of the redox centers and thus their equilibrium potentials. However, repeated OCV measurements using different electrodes of the same material revealed a spread in the recorded values of up to 0.6 V, indicating that cell preparation also plays an important role. The open-circuit voltage depends on the redistribution of ions and electrons after assembly [130]. Electrolyte wetting has been reported to be strongly correlated with measured OCV [131]. It improves ionic access over time and activates regions that were initially electrochemically inactive [132, 133]. Variations in how the electrolyte penetrates and spreads within the electrode structure lead to differences in interfacial contact with the active material, affecting ionic transport, cell impedance, and ultimately the measured open-circuit voltage.

The cyclic voltammetry profile for all azo composites shows strong similarities to the Carbon Black reference measurement, suggesting that the main redox activity comes from the carbon additive in the working electrode. The irreversible reduction peak R_{SEI} can once again be associated with the formation of an SEI layer. The absence of redox activity for the azo group of the organic polymers between 1.5 and 2.5 V could be explained by the sample size of the compounds. After DLP 3D printing, the azo material was obtained as macroscopic flakes, which had to be manually milled prior

to mixing with Carbon Black and PVDF. The time required for the grinding process may not have been sufficient to adequately reduce the particle size. It is likely that parts of the material remained electronically isolated or poorly accessible to Li-ions. As a result, the fraction of active sites that can participate in the electrochemical reaction is limited, causing any possible signals to be non-observable. As the only two exceptions, Anisole and Disodium napthol show additional redox couples (R_1^*/O_1^* and R_2^*/O_2^* for Anisole and R^*/O^* for Disodium napthol) in the potential range of 1.5 to 2.5 V suggesting a small redox activity of the N = N group. However, the peaks notably flat out or even vanish after the second cycle, making the overall contribution very insignificant.

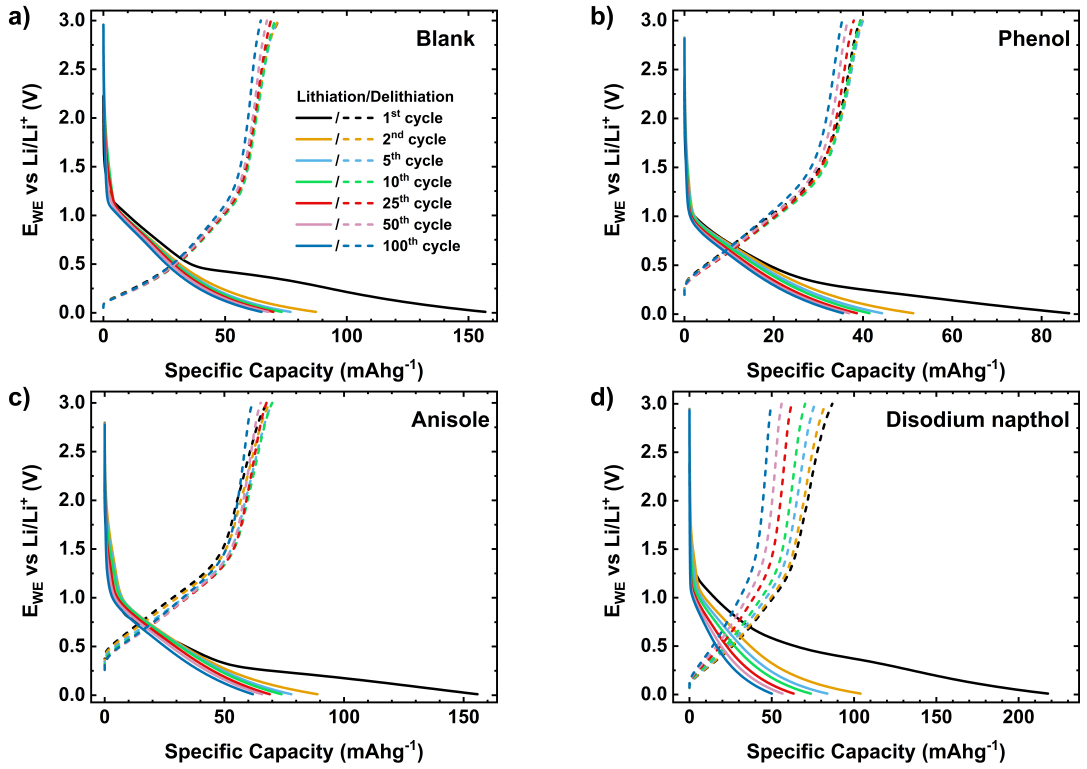


Figure 4.8: Galvanostatic cycling behavior of the azo compounds (a) Blank, (b) Phenol, (c) Anisole and (d) Disodium napthol at a specific current of 200 mA/g in the voltage range $0.01 - 3$ V, showing no additional redox activity beyond Carbon Black.

The electrochemical inactivity of the azo compounds is further supported by galvanostatic charge-discharge cycling (GCPL) shown in Fig. 4.8. The GCPL measurement was conducted at a current density of 200 mA/g in the potential window of $0.01 - 3$ V. The active materials Blank (Fig. 4.8a), Phenol (b), Anisole (c) and Disodium napthol (d) all show the characteristic voltage profile of Carbon Black. The

initial discharge capacities of the compounds are 156.9 mA h/g (Blank), 86.2 mA h/g (Phenol), 155.8 mA h/g (Anisole) and 217.8 mA h/g (Disodium napthol).

In the subsequent cycles, all materials show a capacity fade, approaching 64.9 mA h/g (Blank), 35.3 mA h/g (Phenol), 61.9 mA h/g (Anisol) and 50.0 mA h/g (Disodium napthol) in the 100th cycle. Within the applied voltage range, the total electrochemical contribution comes from both the 60 % of active material and the 30 % of Carbon Black. The specific capacity is normalized to the combined mass of both components and closely matches the measured contribution of CB alone (Section 4.3.1) under the same normalization. For 33 % of Carbon Black, the contribution would be 177 mA h/g for the initial discharge capacity, and 62 mA h/g for the capacity in the 100th cycle, all of which matches and even exceeds the corresponding values of the azo compounds. The only exception is Disodium napthol, which shows an initial specific capacity above the normalized CB contribution. However, with subsequent cycling, the capacity values quickly decrease below this contribution. Overall, almost no redox activity of the active material could be observed.

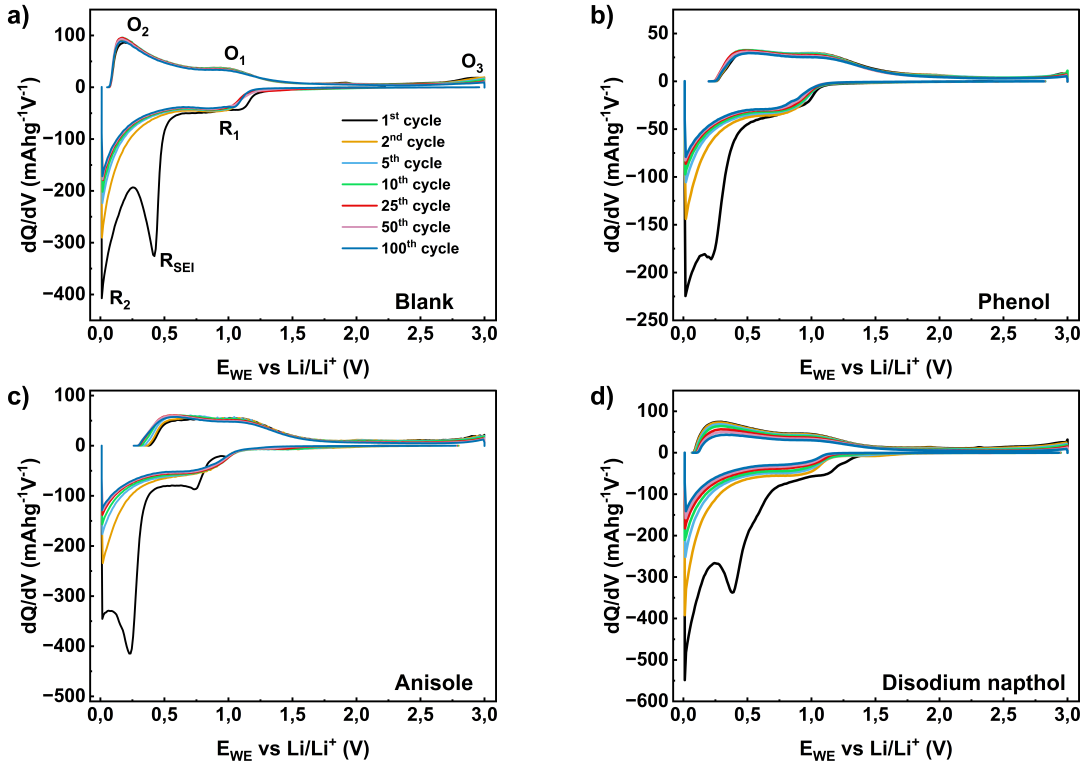


Figure 4.9: Differential capacity plot of GCPL measurement (200 mA/g), recorded for (a) Blank, (b) Phenol, (c) Anisole and (d) Disodiumnapthol.

To further analyze the redox behavior of the azo-based electrodes, differential capac-

ity (dQ/dV) plots are shown in Fig. 4.9, once again for the compounds Blank (a), Phenol (b), Anisole (c) and Disodium napthol (d). Beyond the peaks associated with Carbon Black and SEI, no additional redox peaks occur. This further supports the experimental findings of CV and GCPL, confirming the electrochemical inactivity of the azo group. For Phenol and Anisole, a shift of O_2 to $\sim 0.5\,V$ is observed for all cycles, which may be attributed to errors in the GCPL measurement.

As already discussed, the observed inactivity could be the cause of insufficient milling processes, which in turn lead to large sample sizes and vastly hinder the accessibility of the redox active sites for the charge carriers. As a result, the chosen specific current of 200 mA/g could be too large for efficient Li^+ diffusion into the redox-active sites. To investigate possible kinetic limitations in the electrochemical activity, a GCPL measurement was performed at a reduced specific current of 10 mA/g (Fig. 4.10a). This diminishes kinetic limitations by giving the system more time to equilibrate [134, 135]. The initial reduction cycle features two distinct peaks at 0.59 V (R_{SEI}) and 0.01 V (R_2), as well as a broad peak R^* at $\sim 1.3\,V$. In the following oxidation, three peaks emerge at 0.03 V (O_2), 2.74 V (O^*) and $\sim 3\,V$ (O_3). Additionally, a flat peak O_1 occurs at 0.95 V. In the subsequent cycles, the features R_{SEI}, R^* and O^* vanish, indicating irreversible processes associated with the formation of an SEI layer. Beyond the contribution of Carbon Black, no additional redox activity was observed. Although kinetic limitations cannot be fully excluded, this experimental finding gives room for other possible explanations.

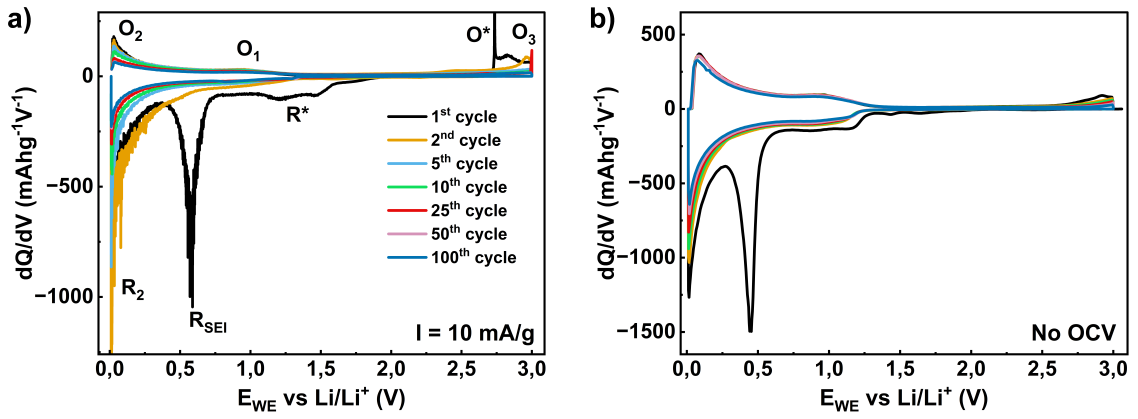


Figure 4.10: Differential capacity plots of galvanostatic cycling, recorded for the Blank material at 10 mA/g (a), and without OCV resting time at 200 mA/g (b).

The observed electrochemical inactivity may also stem from a dissolution of the active material in the ether-based electrolyte, more specifically in the organic solvents

1,3-Diloxane (DOL) or Dimethoxyethane (DME). Previous studies showed that aromatic azo compounds can be soluble in organic battery electrolytes [136]. Prior to the electrochemical measurements, the azo-based LIBs are usually put to rest for 24 h so that their open-circuit voltage has enough time to equilibrate. A dissolution of the azo compounds within this time frame could be a reason for the observed electrochemical inactivity. To test this, a GCPL measurement was performed right after battery assembly, skipping the typical OCV resting time (Fig. 4.10b). However, the differential capacity shows no qualitative deviations from the previous measurements, indicating that the OCV equilibration period doesn't play an important role in the absence of azo-related redox activity.

To verify whether dissolution could in principle occur for the compounds investigated in this work, dedicated solubility tests were performed. Each material (Blank, Phenol, Anisole and Disodium naphthol) was manually ground for one hour to reduce particle size and subsequently dispersed in 300 µL of DOL. The same procedure was repeated using DME. The suspensions were stored for several weeks inside an argon-filled glove box. No visible dissolution or discoloration of the solvents was observed in any case. This indicates that dissolution of the active material in DOL or DME may be excluded as a plausible explanation for the observed electrochemical inactivity.

Additional electrolyte studies were conducted to test whether the compounds perform better in carbonate-based solvents like ethylene carbonate (EC), dimethyl carbonate (DMC) or diethyl carbonate (DEC). Fig. 4.11 depicts differential capacity (dQ/dV) plots for GCPL measurements conducted at a specific current of 200 mA/g in the voltage range $0.01 - 3$ V. Here, the Blank material was used as active material, together with three different electrolytes: 1 M $LiClO_4$ in EC/DEC (1:1) (Fig. 4.11a), 1 M $LiPF_6$ in EC/DMC (1:1) (Fig. 4.11b) and 1 M $LiPF_6$ in EC/DMC + 10wt.% FEC (Fluoroethylene carbonate) (Fig. 4.11c). In the first two cases (Fig. 4.11a & b), the initial reduction scan features peaks at 0.9 V (R_1), 0.68 V (R_{SEI}) and 0.01 V (R_2), followed by oxidation peaks at 0.2 V (O_2), 1.0 V (O_1) and 3.0 V (O_3). From the second cycle onward, R_{SEI} vanishes. A similar behavior can be observed for 1 M $LiPF_6$ with the FEC additive (Fig. 4.11c), except for two additional reduction peaks in the initial cycle, positioned at 1.29 V (R_1^*) and 1.01 V (R_2^*), as well as a less pronounced R_{SEI} peak. These features, however, vanish after the first cycle.

Qualitatively, the measured differential capacity profiles strongly resemble the redox

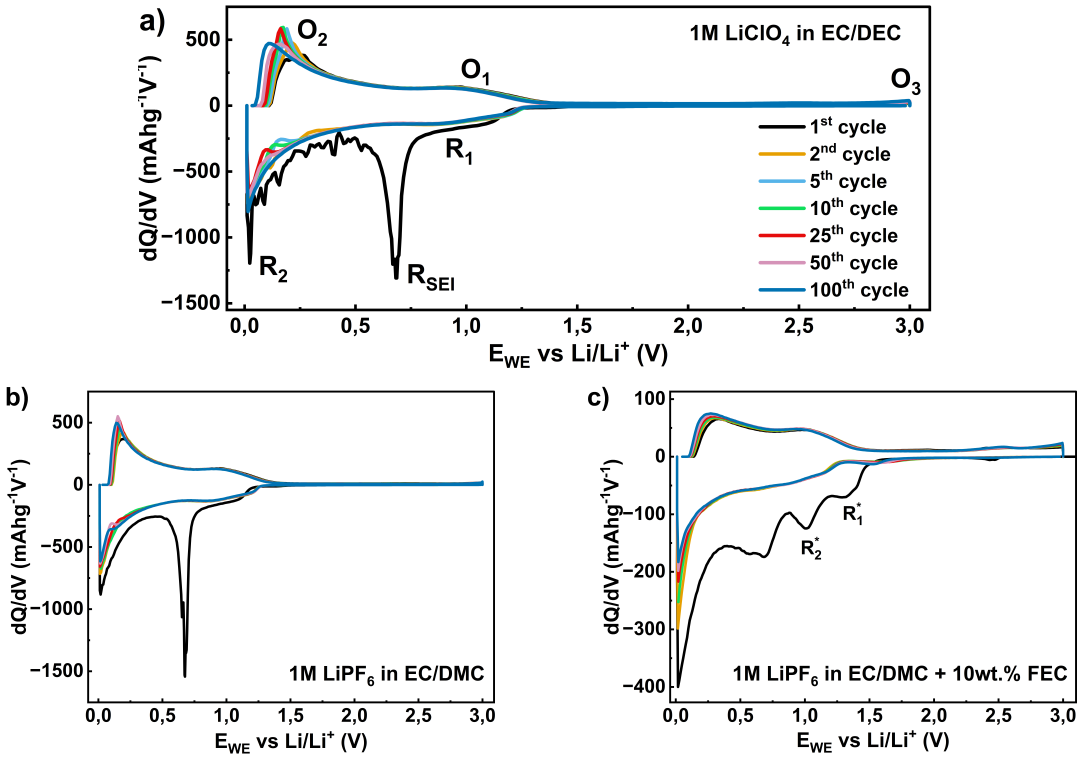


Figure 4.11: Differential capacity plots of GCPL measurements (200 mA/g), recorded for the Blank material with the electrolytes (a) 1M $LiClO_4$, (b) 1M $LiPF_6$ and (c) 1M $LiPF_6$ + 10wt.% FEC. No significant differences are observable beyond the first cycle.

behavior of Carbon Black. Here, the irreversible peak R_{SEI} can be again associated with an SEI layer. In this case, the SEI formation is primarily driven by EC-reduction and occurs at characteristic potentials around $0.6 - 0.8$ V [137]. The additional irreversible peaks R_1^* and R_2^* observed in Fig. 4.11c could be related to the reduction of FEC at higher potentials, which may lead to the early formation of a LiF-rich passivation layer [138, 139]. As a result, the typical EC-driven SEI formation could be suppressed, producing a broad first-cycle reduction feature instead of the sharp SEI peak observed in Figs. 4.11a & b. Overall, the carbonate-based electrolytes also indicate the absence of azo-related electrochemical activity for the four compounds Blank, Phenol, Anisole and Disodium napthol.

To conclude, no significant features beyond those attributed to Carbon Black and SEI formation are observed for the investigated organic azo compounds. Through several dedicated experiments, the dissolution of the active material in the electrolyte could be potentially ruled out as the primary cause. Instead, a possible explanation

could be insufficient particle reduction through manual grinding. As a result, Li-ion diffusion may be vastly limited, preventing the observation of any possible azo-related redox activity even at low specific currents of 10 mA/g.

4.3.3 Nitro Compounds

NBALS: Electrochemical Behavior

As discussed in Section 4.1, nitro (NO_2) functional groups can display superior electrochemical performance in lithium-ion batteries. To investigate this effect in the context of novel nitro-based azo polymers, 4-nitrobenzoic acid lithium salt (NBALS) was selected as a model compound for a cathode material. The synthesis was carried out by Christian Delavier[2]. The obtained NBALS product had a powder structure. The active material was mixed with CB and PVDF binder in a weight ratio of 60:30:10 (AM:CB:PVDF), consistent with the electrode preparation used for the azo-linked polymers. Electrochemical characterization was carried out by CV and GCPL, using 1 M LiTFSI dissolved in DOL/DME (1:1) as the electrolyte.

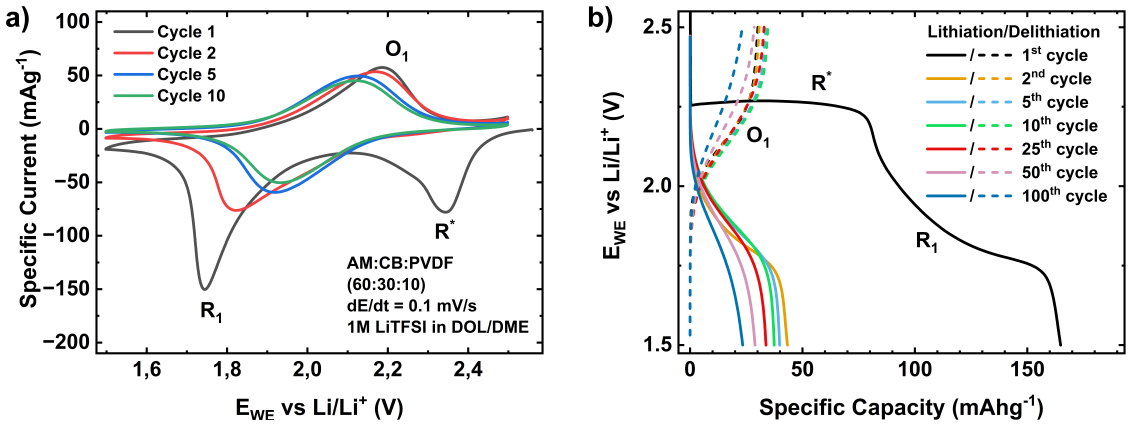


Figure 4.12: Electrochemical performance of NBALS in a potential window of $1.5 - 2.5$ V with 1 M LiTFSI in DOL/DME as the electrolyte. (a) Cyclic voltammetry at a scan rate of 0.1 mV/s, showing irreversible NO_2-reduction R* into the azo group, with subsequent reversible redox reactions R_1/O_1. (b) GCPL measurement of NBALS, recorded at a specific current of 200 mA/g.

Fig. 4.12a shows the initial CV measurement of NBALS, conducted at a scan rate of 0.1 mV/s within the voltage range $1.5 - 2.5$ V. The first, second, fifth and tenth cycles are depicted by the black, red, blue and green curves, respectively. The measurement

[2]Institute for Molecular Engineering and Advanced Materials (IMSEAM), Heidelberg University

starts off at an open-circuit voltage of $\sim$ 2.8 V. In the first discharge cycle, two distinct reduction peaks occur at 2.34 V (R^*) and 1.74 V (R_1). The subsequent oxidation scan shows one peak O_1 at 2.19 V. In the second cycle, the reduction peak R_1 shifts to 1.82 V, while the peak R^* vanishes. Upon oxidation, O_1 moves to 2.17 V. In the cycles five to ten, the peaks R_1 and O_1 are positioned at $\sim$ 1.9 V and $\sim$ 2.1 V, respectively. The corresponding redox potentials and overpotentials are:

	Redox potential $E_{1/2}$	**Overpotential η**
cycle 1	(1.96 ± 0.08) V	(0.44 ± 0.16) V
cycle 2	(2.00 ± 0.09) V	(0.35 ± 0.17) V
cycle 5	(2.03 ± 0.09) V	(0.21 ± 0.18) V
cycle 10	(2.03 ± 0.08) V	(0.18 ± 0.16) V

Table 4.1: Comparison of redox potentials $E_{1/2}$ and corresponding overpotentials η for NBALS in different CV-cycles.

Upon initial discharge, the first reduction peak R^* may correspond to the expected irreversible conversion of the nitro group NO_2 to the azo group. The reduction feature R_1 represents the lithiation of the azo linkage that is formed in situ during this process. Consequently, the oxidation peak O_1 in the first cycle and the redox couple R_1/O_1 observed in subsequent cycles originate from the reversible lithiation/delithiation of the azo group. Compared to Luo et al. [113], which had 2.25 V (R^*) and 2.0 V (R_1), the reduction peaks R^* and R_1 in Fig. 4.12 show a displacement towards larger ($R^* = 2.34$ V) and lower potentials ($R_1 = 1.74$ V), respectively. Differences in electrode microstructure and porosity, as well as interfacial charge-transfer kinetics, are known to influence the apparent peak potentials in cyclic voltammetry [140, 141]. Additionally, Luo et al. used a higher lithium salt concentration (7 M LiTFSI) in their electrolyte. Differences in the composition and concentration of the electrolyte can modify the interfacial distribution of redox-active species and thereby shift the voltammetric response [142]. The observed decrease in peak separation between R_1 and O_1 over successive sweeps ($\eta = 0.44$ V in 1st cycle, $\eta = 0.19$ V in 10th cycle, see Table 4.1) indicates a progressive enhancement in charge transfer kinetics. This can be attributed to an improvement of conductive pathways with subsequent cycling [143], causing an electrochemical activation of previously inaccessable redox sites. Only with repeated cycling, these sites become approachable, reducing the overpotential and causing the peaks to move closer together. Overall, the model compound exhibits qualitative behavior consistent with the literature data, displaying electrochemical features attributable to both nitro and azo functionalities.

Fig. 4.12b displays the potential profile of NBALS from a GCPL measurement, performed at a specific current of 200 mA/g (vs 0.5 C $\hat{=}$154.9 mA/g in Luo et al. [113]) in the voltage range 1.5 − 2.5 V. The initial delithiation capacity of 30.2 mA h/g shows an increase to 34.6 mA h/g within the first 25 cycles, after which it gradually decreases and reaches 23.2 mA h/g by cycle 100. The delithiation profiles show a distinct oxidation plateau O_1 centered around 2.1 V. As for the lithiation capacity, a value of 164.8 mA h/g is reached in the first cycle, compared to $\sim$ 550 mA h/g in Luo et al.. The initial lithiation cycle comprises two plateaus, located at $\sim$ 2.3 V (R^*) and $\sim$ 1.8 V (R_1). In the second lithiation cycle, the specific capacity shows a significant drop to 43.3 mA h/g (vs $\sim$ 220 mA h/g in Luo et al.) as the plateau R^* vanishes. In the subsequent sweeps, the capacity value further decreases and reaches 23.3 mA h/g by the 100th cycle.

The initial increase in the delithiation capacity can be attributed to the aforementioned progressive improvement of conductive pathways, which gradually enhances ionic access to redox-active sites [132, 133]. This causes more charge carriers to participate in the redox reactions, effectively lifting the measured capacity. The large lithiation capacity in the first cycle may result from the multi-electron reduction of the NO_2 pendant group into the azo-group (see Section 4.1). This irreversible reaction is indicated by the vanishing of the plateau R^* from the second cycle onward, accompanied by a steady capacity fade. Meanwhile, the features R_1 and O_1 show reversibility and occur in every cycle. Overall, the GCPL measurement confirms the electrochemical findings of cyclic voltammetry.

In conclusion, the model compound NBALS shows the same qualitative behavior as proposed in the literature, with both irreversible conversion of NO_2 into N = N and the reversible redox activity of the azo group being observed in CV and GCPL. Regarding the specific capacity values, the results are below the literature data, which can be assigned to a lower specific current used in Luo et al. ($\sim$ 155 mA/g vs 200 mA/g). The discrepancy in lithium salt concentration (1 M LiTFSI vs 7 M LiTFSI in Luo et al.) could also play a potential role in the capacity difference and the peak positions in cyclic voltammetry.

Novel Nitro polymers

Building on the experimental results for NBALS, novel NO_2-based polymers are electrochemically investigated. For this, several different nitro compounds were syn-

thesized by Christian Delavier[3]. Their extended structure allows to form crosslinked networks, which makes the polymers less soluble in the electrolyte and enhances their cycling stability [114]. After DLP 3D-printing, the active material was obtained in the form of macroscopic stripes. Same as for the azo-based composites in Section 4.3.2, the AM was manually milled for ~ 1 hour before mixing it with Carbon Black and PVDF binder in a weight ratio of 60:30:10 (AM:CB:PVDF). Electrochemical characterization was carried out by means of cyclic voltammetry (CV) and galvanostatic charge-discharge cycling (GCPL), using 1 M LiTFSI in DOL/DME (1:1) as the electrolyte.

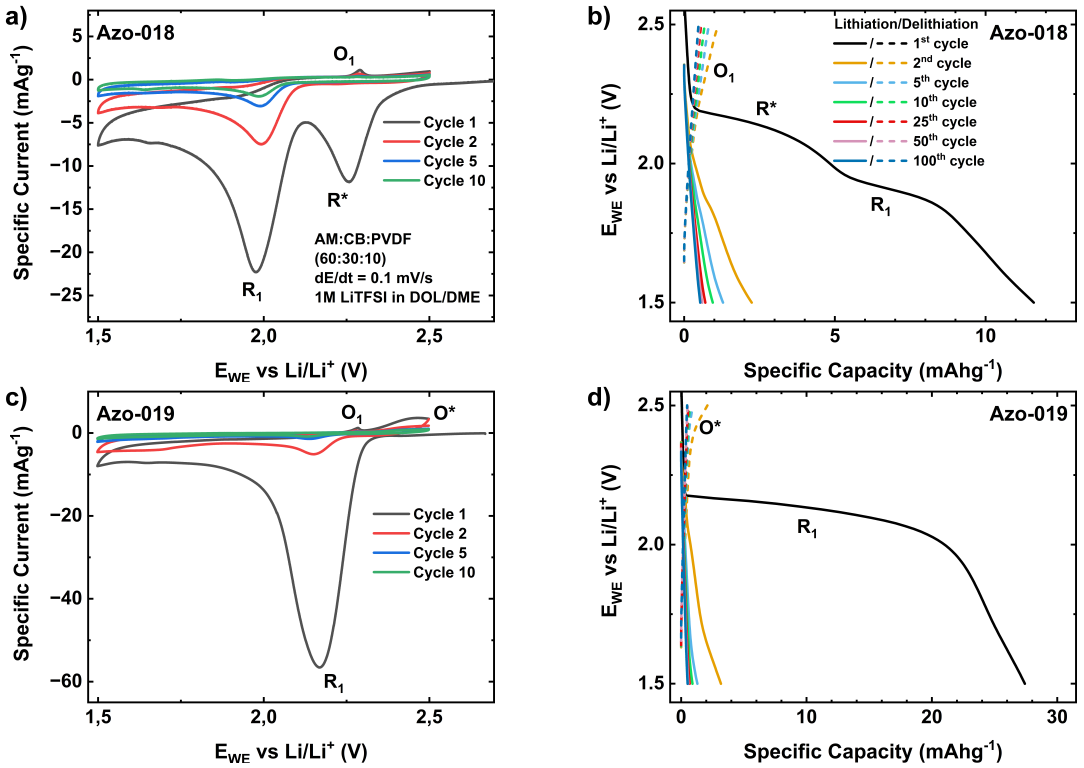


Figure 4.13: Cyclic voltammetry (scan rate 0.1 mV/s) of Azo-018 (a) and Azo-019 (c), along with the corresponding GCPL measurements (b and d respectively) at 200 mA/g, all in a potential window of $1.5 - 2.5$ V.

Fig. 4.13 shows the electrochemical performance of the nitro compounds Azo-018 and Azo-019 (see Section 4.2). For both materials, the measured open-circuit voltage is ~ 2.7 V. Cyclic voltammetry was conducted at a scan rate of 0.1 mV/s in the voltage range $1.5 - 2.5$ V. The black, red, blue and green curves depict the first, second,

[3]Institute for Molecular Engineering and Advanced Materials (IMSEAM), Heidelberg University

fifth and tenth cycles, respectively. Looking at the results of Azo-018 (Fig. 4.13a), the initial cycle shows two distinct reduction peaks, emerging at 2.26 V (R^*) and 1.98 V (R_1), with specific currents of ~ 12 mA/g and ~ 22 mA/g, respectively. Upon oxidation, there is a small peak O_1 occurring at 2.29 V, which, however, flattens out quickly and is hardly visible after the second cycle. Regarding the reduction features, R^* vanishes from the second cycle onward, while R_1 shows reversibility up to the tenth cycle. A similar electrochemical behavior can be observed in galvanostatic cycling (Fig. 4.13b). Initial lithiation yields a capacity of 11.6 mA h/g, corresponding to $\sim 5\,\%$ of the theoretical capacity. Two distinct reduction plateaus emerge at 2.17 V and 1.91 V, labeled R^* and R_1 respectively. Upon initial delithiation, a slight leveling of the voltage profile is observed at 2.29 V (O_1). In the second cycle, the reduction plateau R^* vanishes as the discharge capacity falls to 2.2 mA h/g. Only R_1 remains recognizable, but flattens out from the fifth cycle onward. For all subsequent cycles, both charge and discharge capacities approach zero.

Similar to the NBALS behavior in Luo et al. [113], Azo-018 shows the irreversible reduction R^* of the nitro group to the N = N moiety at around 2.2 V. The redox couple R_1/O_1 of the azo group can also be observed, appearing at similar voltages of ~ 2.0 V for R_1 and ~ 2.3 V (vs ~ 2.2 V in Luo et al.) for O_1. However, the features are less pronounced than for the model compound, especially for the oxidation. The reduction in signal size can be confirmed by galvanostatic cycling, which shows vastly reduced capacity values compared to NBALS. Such a decline in signal size could be attributed to a larger morphology of the active material. While NBALS was synthesized as a powder, the nitro-based polymer was obtained in the form of 3D printed stripes, which first had to be manually grinded. Insufficient milling may lead to excessively large particle sizes, reducing effective contact between the redox-active sites and the conductive carbon network. Consequently, parts of the material remain poorly accessible to Li^+, so that only a limited fraction of redox-active sites can participate in the electrochemical reactions. Another reason for the reduced redox signal could be an inadequate conversion of the nitro into the azo moiety, which is reflected by a smaller reduction peak R^* as compared to the NBALS measurement.

CV-measurements of Azo-019 (Fig. 4.13c) show a very pronounced reduction peak R_1 at 2.17 V in the initial cycle, reaching a peak current of ~ 57 mA/g. Subsequent oxidation yields a small feature O_1 at 2.28 V, followed by the onset of a second peak O^* at 2.46 V. All features show reversibility during the next cycles, but their size significantly decreases. Galvanostatic cycling (Fig. 4.13d) yields a distinct reduction

peak R_1 during the first cycle, centered at $\sim 2.2\,V$. The initial lithiation capacity is $27.4\,mA\,h/g$, which is almost 17 % of the theoretical capacity. In the second cycle, the delithiation profile shows a leveling O_1 at $\sim 2.5\,V$, as the charge capacity reaches $2.0\,mA\,h/g$. However, from the fifth cycle onward, all features disappear, as the capacity values decrease and approach $\sim 0.5\,mA\,h/g$ in cycle 100.

Overall, Azo-019 shows a more pronounced reduction peak than Azo-018. This could be attributed to the longer alkyl spacer, which gives the nitrophenyl group a better contact with the electrolyte. As a result, Li-ions reach the redox-active sites more easily, leading to an increased signal. This is also reflected in a higher initial capacity value. Another plausible explanation could be a merging of the reduction features R_1 and R^* in the first cycle, giving rise to the absence of a distinct irreversible reduction peak. Such a shift of reduction peaks may indicate unexpected structural changes of the compound during cycling.

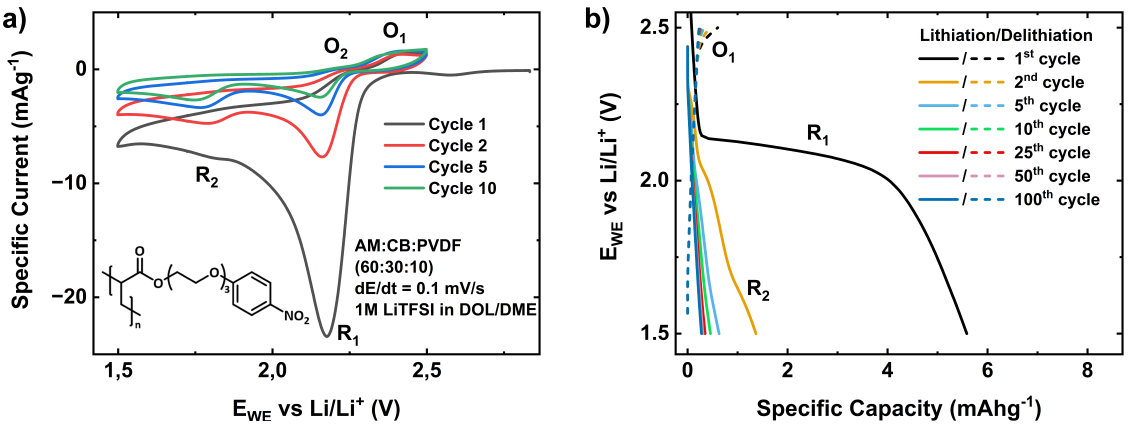


Figure 4.14: Electrochemical behavior of Azo-CD20 in the voltage window $1.5 - 2.5\,V$. (a) Cyclic voltammetry at a scan rate of $0.1\,mV/s$. Inset: structural formula of Azo-CD20, containing an elongated spacer compared to Azo-019 [122]. (b) GCPL measurement, conducted at a specific current of $200\,mA/g$.

The behavior of the initial reduction in Azo-018 and Azo-019 suggests a possible correlation between polymer chain length and the magnitude of the electrochemical signal. Previous studies already observed this pattern [144]. To further investigate this trend, Azo-019 was modified into a new compound called Azo-CD20. Here, the alkyl chain is exchanged with a longer, oxygen-containing spacer (see inset in Fig. 4.14a).

Initial cyclic voltammetry measurements are depicted in Fig. 4.14a. The scan starts at an OCV voltage of $\sim 2.8\,V$. The initial cycle (in black) yields a pronounced

reduction peak R_1 at 2.18 V with a peak current of $\sim$ 23 mA/g. It is followed by a shoulder R_2 at 1.83 V. Upon oxidation, a shoulder O_2 emerges at 2.26 V, followed by a peak O_1 at 2.46 V. During the second cycle (in red), R_2 obtains a peak-like shape. All CV-features show reversibility throughout the subsequent cycles (cycle 5 in blue, cycle 10 in green) and retain their potential values. Looking at the voltage profile of the GCPL measurement (Fig. 4.14b), a distinct reduction plateau R_1 is visible in the first cycle at 2.13 V. The initial lithiation capacity reaches a value of 5.6 mA h/g. During delithiation, a small plateau O_1 can be observed at high voltages around 2.5 V. The second discharge cycle shows a more recognizable reduction plateau R_2 positioned at $\sim$ 1.6 V. Subsequent cycling vastly reduces the specific capacities for both charge and discharge, as the values go down to $\sim$ 0.2 mA h/g by the 100th cycle.

Contrary to the aforementioned trend, the longer spacer of Azo-CD20 leads to a decrease in the size of the initial reduction feature R_1 compared to Azo-019. As a result, the specific capacity value in the first cycle is also reduced and is even below the results of Azo-018. However, the reversibility of all CV-features is more pronounced and better observed for Azo-CD20. Similar to Azo-019, a distinct irreversible peak R^* is absent. This indicates that Azo-CD20 may have undergone different, unforeseen structural changes, too. This could cause a merging of the peaks R_1 and R^*.

Out of all three compounds, Azo-018 seems to give the most promising results. Although it does not have the highest capacity values, its electrochemical profile most closely resembles the behavior of the model compound NBALS. The significantly reduced specific capacity values for Azo-018 could be due to an inadequate milling process, which decreases the fraction of active sites that are electrochemically accessible, leading to lower measured specific capacities.

To circumvent this problem, conductive carbon is integrated into the synthesis of the active material. Incorporation of Carbon Black (CB, Super C65, Timcal) during the printing process of Azo-018 leads to the modified compound Azo-021-d. CB is a strong light absorber in the UV and visible range used for DLP printing [145]. Thus, mixing it into the resin causes the ink to be optically opaque, so the projected light cannot penetrate deeply into the layer. As a result, the photoinitiator is activated only in a very thin region close to the illuminated surface, while the deeper parts of the layer receive too little light to polymerize [122]. This limits the achievable curing depth and the thickness of the layer. Thus, only 0.5 wt % of CB could be

incorporated into the production process to achieve a sufficient size of the Azo-021-d sample [122]. The synthesized active material was milled and mixed with Carbon Black and PVDF binder in a weight ratio of 60:30:10 (AM:CB:PVDF).

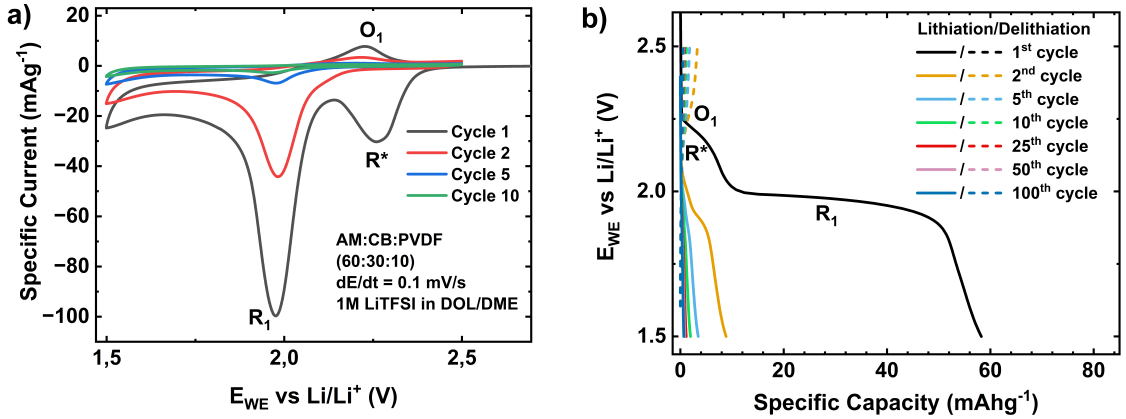


Figure 4.15: Electrochemical performance of Azo-021-d in a voltage window of 1.5 – 2.5 V. (a) Cyclic voltammetry at a scan rate of 0.1 mV/s. (b) GCPL measurement, conducted at 200 mA/g. The incorporated carbon in Azo-021-d yields an enhanced electrochemical signal compared to the precursor compound Azo-018.

Fig. 4.15a shows a cyclic voltammogram of Azo-021-d, recorded at a scan rate of 0.1 mV/s in the potential window 1.5 – 2.5 V. Starting at an open-circuit voltage of ∼ 2.8 V, the first cycle (black curve) includes two reduction peaks centered at 2.26 V (R*) and 1.98 V (R_1). The latter reaches a specific current of ∼ 100 mA/g. Subsequent oxidation features a peak O_1 emerging at 2.23 V. During the second cycle (red curve), R* vanishes, while R_1 and O_1 are preserved at the same potentials, but with reduced current values. By the fifth (in blue) and tenth cycle (in green), both peaks gradually flatten out.

Fig. 4.15b depicts a GCPL measurement on an Azo-021-d working electrode, performed at a current density of 200 mA/g in the voltage range 1.5 – 2.5 V. The first lithiation cycle features two reduction plateaus R* and R_1, emerging at ∼ 2.2 V and ∼ 2.0 V, respectively. The latter one is particularly pronounced, contributing ∼ 40 mA h/g to the specific capacity. The resulting initial discharge capacity measures 59 mA h/g. It falls to 9 mA h/g in the second lithiation cycle and gradually approaches zero during subsequent cycling.

Just as for NBALS and Azo-018, Azo-021-d shows an irreversible reduction feature in the first cycle (R*) indicating the proposed NO_2-reaction into the azo group. Compared to the results of Azo-018, the modified compound shows significantly enhanced

reduction and oxidation peaks. This indicates that more charge carriers participate in the redox reactions, owing to the improved electrical conductivity caused by the conductive carbon incorporation. Galvanostatic cycling confirms this finding, showing an initial discharge capacity of almost 60 mA h/g, which is an enhancement of over 400 % compared to Azo-018 without incorporated Carbon Black.

Another possibility to enhance the electrochemical activity of Azo-018 could be the addition of an inductive electron-withdrawing group like CF_3. Such a substituent is very electronegative due to its three fluorine atoms. It could pull electron density away from the phenyl ring and, through π-conjugation, also from the azo group, making it more electron-deficient [122]. As a result, the redox-active center could become thermodynamically easier to reduce, as its LUMO (lowest unoccupied molecular orbital) energy is lowered [146, 147]. The reduced state may become more stable, which could improve electrochemical reversibility and result in more pronounced peaks [146]. For this purpose, a new nitro compound Azo-025 was synthesized by Christian Delavier[4], introducing the inductive CF_3 substituent into the structure of Azo-018 (see Fig. 4.16a inset).

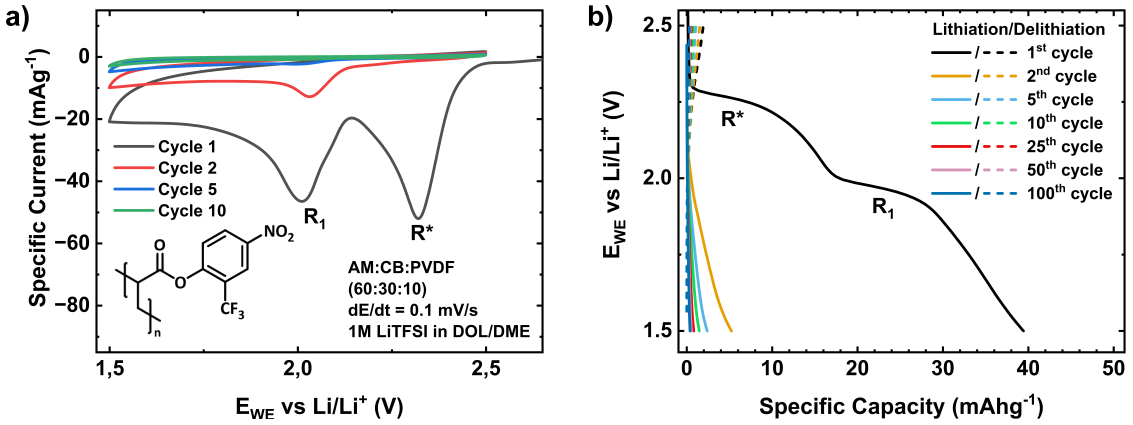


Figure 4.16: (a) Cyclic voltammetry of Azo-025 at a scan rate of 0.1 mV/s. Inset: structural formula of Azo-025, comprising the inductive electron-withdrawing substituent CF_3 [122]. (b) GCPL measurement, conducted at 200 mA/g. Both in a voltage window of 1.5 – 2.5 V.

Fig. 4.16a shows a CV measurement of the material, performed at a scan rate of 0.1 mV/s in the voltage range 1.5 – 2.5 V. The first cycle (black curve) shows two reduction peaks at 2.32 V (R^*) and 2.01 V (R_1), which achieve peak currents of $\sim$ 52 mA/g and $\sim$ 46 mA/g, respectively. In the second cycle (red curve), R_1 slightly

[4]Institute for Molecular Engineering and Advanced Materials (IMSEAM), Heidelberg University

shifts to 2.03 V, while R* vanishes. During the fifth and tenth cycles (blue and green curve, respectively), the peak R_1 also flattens out. Interestingly, no oxidation feature is observed throughout all cycles. Galvanostatic cycling (Fig. 4.16b) confirms this observation. The initial reduction scan shows two distinct plateaus at 2.27 V (R*) and 1.98 V (R_1), resulting in a discharge capacity of 39.4 mA h/g. In the second cycle, R* disappears, while R_1 still shows some impact on the specific capacity, which reaches a value of 5.2 mA h/g. During the subsequent cycles, the capacity value gradually approaches zero. As for the oxidation profile, no distinct plateaus can be observed. Consequently, the charge capacity shows negligible values going from 2.5 mA h/g in the first cycle to 0.3 mA h/g in cycle 100.

Similar to the nitro compounds Azo-018 and Azo-021-d, the CF_3-substituted Azo-025 exhibits a feature R* which may be attributed to the irreversible reduction of the NO_2 group in the first cycle. The reduction peak R_1 shows reversibility and can be associated with the lithiation of the azo group to the twice negatively charged $N - N$ moiety. Both reduction features show increased current values in the first cycle (R* increases by $\sim 330\,\%$, R_1 by $\sim 110\,\%$) compared to Azo-018. Adding the inductive substituent CF_3 could have made the redox-active center more electron-deficient, stabilizing the reduced state. As a result, the reduction peaks become more pronounced [146]. The stabilized reduction is also reflected by increased discharge peaks in GCPL, leading to a higher initial capacity. Still, the compound is below Azo-021-d in terms of peak size and capacity values, indicating that the incorporation of conductive carbon could have a more beneficial effect on electrochemical performance. Compared to Azo-018 and Azo-021-d, both R* and R_1 show slightly increased potential values. This could be attributed to the presence of the electron-withdrawing CF_3 group, too. It may lower the energy of the molecule's LUMO, enabling electron uptake at more positive potentials and thereby shifting the observed redox potential to higher values [147]. The lowered LUMO energy could also be the cause for the absence of an oxidation feature. Besides facilitating reduction processes, it could also increase the barrier for electron removal. As a result, the oxidation potential may have been raised beyond the scanned voltage window. Previous studies have shown that even minor changes in substituents can affect oxidation processes compared to reduction, resulting in a more pronounced shift of oxidation potentials towards higher values [148].

In conclusion, the novel nitro-based azo compounds exhibit more favourable electrochemical performance than the composites discussed in Section 4.3.2. In addition

to the proposed irreversible reduction of the NO_2 group to the azo moiety, subsequent reversible redox processes associated with the azo functionality were also observed for most compounds. Among the investigated systems Azo-018 and Azo-019, the shorter polymer Azo-018 showed a behavior most consistent with the model compound NBALS. Increasing the spacer length, however, led to indications of structural rearrangements within the composite material. Introduction of the electron-withdrawing CF_3 substituent further stabilised the reduction process, resulting in more pronounced reduction peaks. Likewise, incorporation of Carbon Black during synthesis improved both peak intensity and specific capacity. These findings suggest that the primary limitation of the observed azo-linked redox activity could be related to the particle size. Inadequate grinding leads to larger particles, which reduces the effective contact between the conductive carbon network and the redox-active sites, limiting the electrochemical performance.

4.4 Conclusion and Outlook

This chapter investigated the electrochemical behavior of novel synthesized azo- and nitro-based compounds as potential organic electrode materials for lithium-ion batteries. Motivated by the promising redox activity of azo groups (N = N) reported in literature, and the sustainability advantages of polymeric materials, a series of novel PEGDA-crosslinked polymers with different aromatic side groups were examined by cyclic voltammetry and galvanostatic cycling. In addition, nitro-functionalized polymers were studied, exploiting the well-known irreversible conversion of NO_2 to an electrochemically active azo moiety during the first lithiation cycle.

For the azo-linked polymers Blank, Phenol, Anisole, and Disodium napthol, no distinct redox activity attributable to the azo group could be observed. Their electrochemical signatures closely resembled that of Carbon Black alone, and the measured specific capacities matched the expected contribution of the conductive additive. Systematic investigations indicated that dissolution of the polymers in the ether-based solvents DOL and DME was unlikely, including any measurable influence of the OCV resting time. Additional measurements with various carbonate-based electrolytes likewise showed no change in the redox activity of the azo moiety. Even at very low current densities, where kinetic limitations should be minimized, no additional azo-related redox processes were observed. Overall, these findings suggest that the primary limitation is less likely to be chemical or charge-transfer related,

and more likely associated with morphological factors. These DLP-printed polymers had to be milled manually, and insufficient particle size reduction likely resulted in poor electronic conductivity and restricted Li^+ access to the redox-active sites.

In contrast, most of the nitro-based systems demonstrated an electrochemical activity consistent with the mechanism known from the model compound NBALS. The characteristic irreversible reduction of the NO_2 group to the azo moiety in the first cycle and subsequent reversible redox reactions of the N = N group could be successfully reproduced for most compounds. Out of the investigated polymers Azo-018 and Azo-019, the former showed behavior most similar to the model compound, though at much lower specific capacities. This could be again attributed to morphological limitations due to insufficient grinding. Systematic structural modifications provided further insight. Increasing the spacer length between the polymer backbone and the nitrophenyl group (Azo-019, Azo-CD20) altered the electrochemical response, indicating that molecular architecture strongly influences electrolyte contact and redox site accessibility. Furthermore, the absence of a distinct irreversible reduction peak in the first cycle indicates possible structural changes in the material upon cycling. Incorporation of an electron-withdrawing CF_3 substituent in Azo-025 enhanced the reduction features compared to Azo-018 and shifted them towards slightly higher potentials, indicating that the electronic structure of the redox center can be tuned chemically. The strong inductive effect of CF_3 withdraws electron density from the azo moiety, thereby lowering its LUMO energy. As a result, reduction becomes thermodynamically more favorable and occurs at more positive potentials. However, this effect occurs at the expense of the oxidation feature, which is significantly suppressed or shifted beyond the investigated voltage window. Incorporating a small amount of conductive Carbon Black directly into the polymer during synthesis (Azo-021-d) resulted in a noticeable increase in electrochemical performance, with the specific capacity improving by more than 400 % compared to the unmodified polymer Azo-018. This highlights the importance of sufficient electronic connectivity and effective percolation pathways for enabling the redox activity of these materials.

Overall, the results show very little to none electrochemical activity of the azo group. Particularly, this activity can be observed in nitro-based compounds. The main limiting factors appear to be kinetic and morphological in nature, likely arising from insufficient particle size reduction and poor electrical conductivity within the composite electrode. Future work should therefore focus on optimized milling processes and alternative electrode fabrication techniques. Development of fully 3D-printed

electrodes could allow for sufficiently high incorporation of conductive carbon directly into the polymer structure. This would allow better utilization of the intrinsic redox capability of the azo-based polymers. To improve the cyclability of the material, Li-ion containing monomers could be directly integrated into the polymer structure. This would provide built-in ionic pathways and reduce the dependence on long-range Li^+ diffusion from the electrolyte into the bulk of the material.

5. Summary and Outlook

This thesis investigated two distinct research directions in the field of lithium-ion battery materials: the disentanglement of light and temperature effects on the electrochemical performance of vanadium pentoxide (V_2O_5) cathodes, and the evaluation of novel azo- and nitro-based organic compounds as potential sustainable electrode materials. The study of V_2O_5 revealed that deep lithiation down to 2 V may promote the creation of defect states, which manifest as additional redox features in cyclic voltammetry near 3.5 V and as shoulders around 2.5 V, 3.25 V, and 3.7 V. Restricting the lower voltage limit to 2.5 V suppressed these features, indicating that they are associated with the γ-phase transition and the accompanying structural degradation of the V_2O_5 lattice. Under white light illumination, cyclic voltammetry showed reduced overpotentials and an approximate increase of 21 % in peak currents, indicating enhanced reaction kinetics. Temperature measurements using an embedded Pt1000 sensor inside the coin cell showed that illumination raises the electrode temperature by approximately 3 °C, demonstrating that photo-thermal contributions cannot be neglected. Temperature-controlled dark reference measurements at 30 °C confirmed that while thermal effects contribute to the observed improvements, a genuine photonic effect exists beyond pure heating. However, galvanostatic cycling revealed no significant enhancement of specific capacity under illumination beyond systematic measurement errors. The main limiting factors preventing a distinct light effect could stem from the large morphology of the synthesized V_2O_5 microrods, which reaches up to $\sim 2\,\mu m$ in diameter. Additionally, the use of Kapton windows instead of glass may limit light transmission at wavelengths relevant for V_2O_5 absorption. The choice of white light instead of monochromatic illumination matched to the materials bandgap further reduced the photoconversion efficiency. For in-situ temperature measurements, placing the Pt1000 sensor at the electrode-electrolyte interface during cell operation may have physically hindered Li^+ diffusion, resulting in drastically reduced measured capacity values. Infrared thermometry was explored as a non-contact alternative, but potentially emissivity-related inaccuracies of the setup prevented reliable measurements.

Electrochemical characterization of the azo-linked polymers Blank, Phenol, Anisole and Disodium napthol revealed no significant redox activity attributable to the azo

(N = N) group. Systematic investigations indicated that dissolution of the active material in the ether-based electrolyte LiTFSI in DOL/DME was unlikely. A significant influence of open-circuit resting time of 24 hours could also be effectively excluded. Measurements with carbonate-based electrolytes $LiClO_4$ in EC/DEC, $LiPF_6$ in EC/DMC with and without an FEC additive likewise showed no azo-related signals. Even at a reduced specific current of 10 mA/g, which should minimize kinetic limitations, no additional redox activity was observed. These findings suggest that morphology could be an important limiting factor. The DLP-printed polymers were obtained as macroscopic flakes and required manual milling, which likely proved insufficient to achieve adequate particle size reduction. Consequently, poor electronic conductivity and restricted Li^+ access to redox-active sites may have prevented observable electrochemical activity. In contrast, most nitro-based compounds exhibited electrochemical behavior that qualitatively resembled the model system 4-nitrobenzoic acid lithium salt (NBALS). An initial irreversible reduction of the nitro (NO_2) group into an azo moiety at approximately 2.25 V was observed, followed by reversible redox reactions of the azo group centered around 2.0 V for the reduction, and around 2.2 V for the oxidation. Among the novel nitro-polymers Azo-018 and Azo-019, the former showed behavior most similar to NBALS, albeit with reduced specific capacities. Increasing the spacer length between the nitrophenyl group and the polymer backbone (Azo-019, Azo-CD20) led to the disappearance of the characteristic irreversible reduction feature R^*, suggesting structural rearrangements during cycling. Introduction of the electron-withdrawing CF_3 substituent (Azo-025) intensified the reduction peaks by approximately 330 % for R^* and 110 % for R_1 compared to Azo-018. At the same time, it suppressed the corresponding oxidation feature, possibly shifting it beyond the scanned voltage window of $1.5 - 2.5$ V. The most significant improvement came from incorporating Carbon Black directly into the polymer synthesis (Azo-021-d), which enhanced the specific capacity by more than 400 % compared to the unmodified Azo-018, reaching an initial discharge capacity of approximately 60 mA h/g. This suggests that, in addition to inadequate particle size reduction, insufficient electrical conductivity could be the main limiting factor for the organic compounds studied in this thesis.

Future work on V_2O_5 photo-electrodes should prioritize the use of smaller nanostructures like nanofibers, whose higher specific surface areas could maximize light-induced effects. The choice of illumination should be revisited: monochromatic white light adjusted to the absorption spectrum of V_2O_5 would improve photo-conversion

efficiency compared to white light. Transparent glass windows should replace Kapton to ensure adequate light transmission to the active material. For reliable disentanglement of photonic and photo-thermal effects, emphasis should be placed on improved cell designs such as larger window diameters, allowing for proper non-contact temperature measurement techniques like infrared thermometry.

For organic azo- and nitro-based materials, the primary challenge is morphological. Future efforts should focus on producing polymers with smaller particle sizes, which could be achieved by e.g. ball milling. Fully 3D-printed electrodes, where the conductive carbon network is integrated during the printing process rather than added afterward, could provide superior electrical connectivity and eliminate the need for manual grinding. For that, higher loadings of incorporated Carbon Black should be attempted if the optical opacity limitations of DLP printing can be overcome through alternative photopolymerization techniques. Incorporation of Li^+-containing monomers directly into the polymer backbone could provide built-in ionic pathways, reducing dependence on long-range Li^+ diffusion from the electrolyte and potentially improving cyclability.

All in all, this work demonstrated that the electrochemical performance of both inorganic and organic battery materials is critically governed by morphological and microstructural factors rather than solely by their intrinsic chemical or electronic properties. If these challenges can be overcome, both material classes hold significant promise for further investigation toward more sustainable energy storage solutions.

A. Appendix

A.1 My Python Program

In order to read out the Keithley 2000 multimeter attached to the illuminated V_2O_5 cell (see Section 3.2) and convert the measured Pt1000 resistance values into temperature, I wrote the Python program "BatteryTempReadout". It saves the measured resistance values, the converted temperature and the respective timestamps and errors into a CSV-file, which facilitates later data analysis with Origin. For the program, I used common GUI tools like Kivy to make the interface more user-friendly.

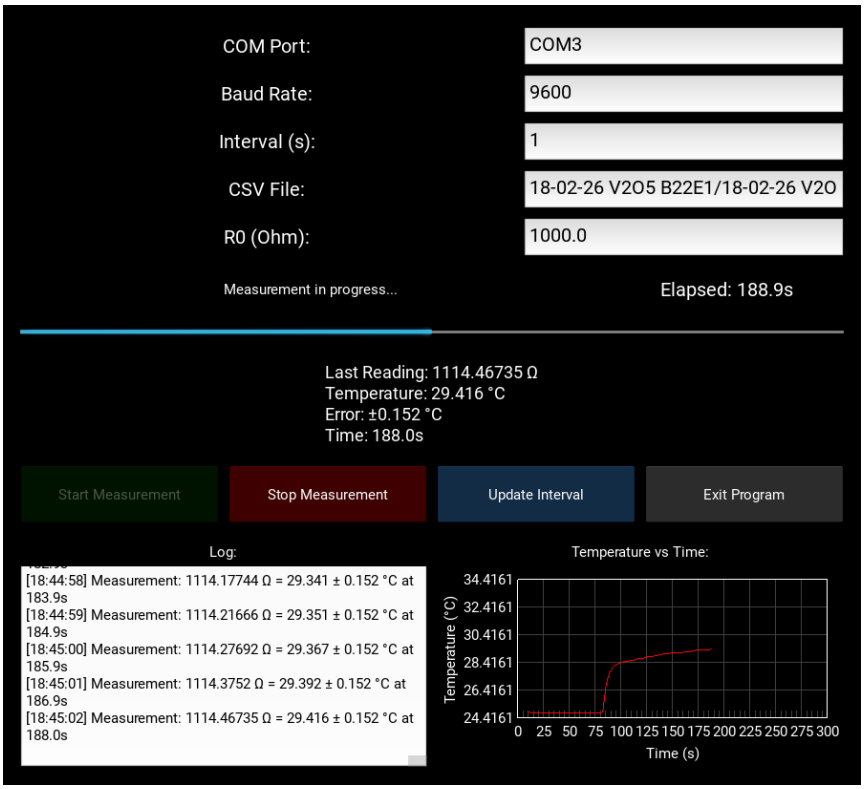


Figure A.1: Python program "BatteryTempReadout" in operation, recording the light-induced temperature increase of a V_2O_5-based electrode.

Fig. A.1 shows a screenshot of the program in use. Prior to starting the light-induced

measurement, the multimeter is connected to the PC with the installed application. After turning the multimeter into remote mode and opening the program, several parameters have to be entered:

- COM-port of the PC (through which the multimeter is connected)
- Baud rate (rate of communication between multimeter and programming terminal, is preset to 9600)
- Interval (in seconds) in which the resistance value is read out from the multimeter
- The desired name of the CSV output file
- The resistance R_0 (in Ω) of the used platimum sensor at 0 °C (1000.0 for a Pt1000)

The application is launched by pressing the green "Start Measurement" button once the battery experiment begins. As the multimeter records the resistance values of the Pt1000 sensor, the program converts them into temperature values using the Callendar-van Dusen equation (3.4). The error of the resistance measurement is composed of the uncertainty in the multimeter reading and the error of the platinum thermometer. The Keithley 2000 multimeter has a 0.008 % 90-day basic resistance accuracy [149], which means a reading error

$$\Delta R_{\text{multimeter}} = \pm 0.008\,\% \cdot R \tag{A.1}$$

of the measured resistance R. For the temperature measurements in this work, the commercial Pt1000 resistance thermometer 32208707 of the group M222 from Yageo Nexensos [57] is used, which belongs to the tolerance class of F 0.1 (1/3 B). According to IEC60751 [78], the temperature error of the platinum sensor is:

$$\Delta T_{\text{Pt1000}} = \pm(0.1 + 0.0017 \cdot T)^{\circ}\text{C}\,, \tag{A.2}$$

with 0.1 °C being the constant base tolerance at 0 °C for the F 0.1 class, and $0.0017 \cdot T$ a temperature-dependent error term. For room temperature (RT, $\sim$ 25 °C), this leads to an error of $\Delta T_{\text{Pt1000}} = 0.1425\,^{\circ}\text{C}$. By taking the derivative of the Callendar-van Dusen equation (3.4) and neglecting the quadratic term for RT and small ΔT, the

resistance change per °C is approximately:

$$\frac{\mathrm{dR}}{\mathrm{dT}} \approx \mathrm{R}_0 \cdot \alpha \,, \tag{A.3}$$

with $\alpha = 3.85 \times 10^{-3\circ}\mathrm{C}^{-1}$ being the sensitivity of the Pt1000 sensor [78], and $\mathrm{R}_0 = 1000\,\Omega$ its resistance at 0 °C. From (A.3), the temperature uncertainty due to tolerance can be approximated as $\Delta\mathrm{T} \approx \Delta\mathrm{R}/(\mathrm{R}_0 \cdot \alpha)$, so the instrument temperature error amounts to:

$$\Delta\mathrm{T}_{\mathrm{multimeter}} \approx \frac{\Delta\mathrm{R}_{\mathrm{multimeter}}}{\mathrm{R}_0 \cdot \alpha} \,, \tag{A.4}$$

At $T = 25\,°\mathrm{C}$, the error is $\Delta\mathrm{T}_{\mathrm{multimeter}} = \pm 0.0229\,°\mathrm{C}$. Using root-sum-square, the combined error of the temperature measurement becomes:

$$\Delta\mathrm{T}_{\mathrm{total}} = \sqrt{\Delta\mathrm{T}^2_{\mathrm{multimeter}} + \Delta\mathrm{T}^2_{\mathrm{Pt1000}}} \,, \tag{A.5}$$

yielding an uncertainty of $\Delta\mathrm{T}_{\mathrm{total}} \approx 0.1443\,°\mathrm{C}$ at room temperature.
On the bottom left, the program logs the measured R- and T-values with the respective timestamps. To the right of this, the temperature values are plotted over time, with the axis limits dynamically adjusting to the most recently measured data. If desired, the time interval for multimeter readout can be modified in-operando by entering the new value into the respective text input and pressing the blue button "Update interval". The temperature measurement can be terminated by pressing the red button "Stop measurement", or by exiting the program via the gray button "Exit program".

Bibliography

[1] J Mitali, S Dhinakaran, and AA Mohamad. Energy storage systems: A review. Energy Storage and Saving, 1(3):166–216, 2022.

[2] Kitalu Ricin Ngoy, Valantine Takwa Lukong, Kelvin O Yoro, John Beya Makambo, Nonso Christopher Chukwuati, Chinedu Ibegbulam, Orevaoghene Eterigho-Ikelegbe, Kingsley Ukoba, and Tien-Chien Jen. Lithium-ion batteries and the future of sustainable energy: A comprehensive review. Renewable and Sustainable Energy Reviews, 223:115971, 2025.

[3] John B Goodenough and Kyu-Sung Park. The li-ion rechargeable battery: a perspective. Journal of the American Chemical Society, 135(4):1167–1176, 2013.

[4] Phuoc-Anh Le. A review of construction and sustainable recycling strategies of lithium-ion batteries across electric vehicle platforms. RSC advances, 15(42): 35687–35725, 2025.

[5] J-M Tarascon and Michel Armand. Issues and challenges facing rechargeable lithium batteries. nature, 414(6861):359–367, 2001.

[6] Naoki Nitta, Feixiang Wu, Jung Tae Lee, and Gleb Yushin. Li-ion battery materials: present and future. Materials today, 18(5):252–264, 2015.

[7] M Stanley Whittingham. Lithium batteries and cathode materials. Chemical reviews, 104(10):4271–4302, 2004.

[8] Yuan Yue and Hong Liang. Micro-and nano-structured vanadium pentoxide (v2o5) for electrodes of lithium-ion batteries. Advanced Energy Materials, 7 (17):1602545, 2017.

[9] A Bystrom, K-A Wilhelmi, and Otto Brotzen. Vanadium pentoxide: a compound with five-coordinated vanadium atoms. Acta Chemica Scandinavica (Denmark) Divided into Acta Chem. Scand., Ser. A and Ser. B, 4, 1949.

[10] Akshaykumar D Salunke, Shubham Chamola, Angus Mathieson, Buddha Deka Boruah, Michael de Volder, and Shahab Ahmad. Photo-rechargeable li-ion batteries: device configurations, mechanisms, and materials. ACS Applied Energy Materials, 5(7):7891–7912, 2022.

[11] B. D. Boruah, B. Wien, and M. D. Volder. "Light Rechargeable Lithium-Ion Batteries Using V_2O_5 Cathodes". Nano Lett., vol. 21, pp. 3527-3532, 2021. Available: `https://pubs.acs.org/doi/10.1021/acs.nanolett.1c00298`.

[12] Michael Wilhelm, Ruth Adam, Aman Bhardwaj, Iuliia Neumann, Sung Hun Cho, Yuki Yamada, Tohru Sekino, Jianming Tao, Zhensheng Hong, Thomas Fischer, et al. Carbon-coated electrospun v2o5 nanofibers as photoresponsive cathode for lithium-ion batteries. Advanced Engineering Materials, 25(1): 2200765, 2023.

[13] Lifu Tan, Byung-Man Kim, Arvind Pujari, Ze He, Buddha Deka Boruah, and Michael De Volder. Photothermal enhancement of prussian blue cathodes for li-ion batteries. Nano Letters, 24(30):9147–9154, 2024.

[14] Lifu Tan, Byung-Man Kim, Kohei Shimokawa, Su Jin Heo, Arvind Pujari, and Michael De Volder. Distinguishing between photothermal and photoelectric effects in li-ion batteries. ACS electrochemistry, 1(6):921–927, 2025.

[15] Arvind Pujari, Byung-Man Kim, Farheen N Sayed, Kate Sanders, Wesley M Dose, Angus Mathieson, Clare P Grey, Neil C Greenham, and Michael De Volder. Does heat play a role in the observed behavior of aqueous photobatteries? ACS Energy Letters, 8(11):4625–4633, 2023.

[16] Arumugam Manthiram. A reflection on lithium-ion battery cathode chemistry. Nature communications, 11(1):1550, 2020.

[17] Musab Hammas Khan, Patrizia Lamberti, and Vincenzo Tucci. Multidimensional inorganic electrode materials for high-performance lithium-ion batteries. Inorganics, 13(2):62, 2025.

[18] Zhiping Song and Haoshen Zhou. Towards sustainable and versatile energy storage devices: an overview of organic electrode materials. Energy & Environmental Science, 6(8):2280–2301, 2013.

[19] Yang Xu, Min Zhou, and Yong Lei. Organic materials for rechargeable sodium-ion batteries. Materials Today, 21(1):60–78, 2018.

[20] Simon Muench, Andreas Wild, Christian Friebe, Bernhard Haupler, Tobias Janoschka, and Ulrich S Schubert. Polymer-based organic batteries. Chemical reviews, 116(16):9438–9484, 2016.

[21] Yanliang Liang, Zhanliang Tao, and Jun Chen. Organic electrode materials for rechargeable lithium batteries. Advanced Energy Materials, 2(7):742–769, 2012.

[22] Wen-Fu Fu, Huifang-Jie Li, De-Hui Wang, Liang-Jun Zhou, Li Li, Xin Gan, Quan-Qing Xu, and Hai-Bin Song. A novel kolbe reaction pathway for a selective one-and two-electron reduction of azo compounds. Chemical communications, (37):5524–5526, 2009.

[23] Changxu Lin, Long Yang, Mengchun Xu, Qi An, Zheng Xiang, and Xiangyang Liu. Properties and applications of designable and photo/redox dual responsive surfactants with the new head group 2-arylazo-imidazolium. RSC advances, 6 (57):51552–51561, 2016.

[24] Wenyan Ma, Chong Zhang, Xiaomin Gao, Chang Shu, Chao Yan, Feng Wang, Yu Chen, Jing Hui Zeng, and Jia-Xing Jiang. Structure evolution of azo-fused conjugated microporous polymers for high performance lithium-ion batteries anodes. Journal of Power Sources, 453:227868, 2020.

[25] Zhonghui Sun, Hongyan Yao, Jiabin Li, Bing Liu, Ziyu Lin, Meng Shu, Huiling Liu, Shiyang Zhu, and Shaowei Guan. Stable hexaazatrinaphthalene-based planar polymer cathode material for organic lithium-ion batteries. ACS Applied Materials & Interfaces, 15(36):42603–42610, 2023.

[26] Yong Lu and Jun Chen. Prospects of organic electrode materials for practical lithium batteries. Nature Reviews Chemistry, 4(3):127–142, 2020.

[27] Manik E Bhosale, Sudong Chae, Ji Man Kim, and Jae-Young Choi. Organic small molecules and polymers as an electrode material for rechargeable lithium ion batteries. Journal of Materials Chemistry A, 6(41):19885–19911, 2018.

[28] Chengwei Ye, XiaoYa Zhou, and Shaochun Tang. An azo polymer with abundant active sites and extended conjugation as a stable cathode for high-performance zinc-organic batteries. Angewandte Chemie International Edition, 64(17):e202501743, 2025.

[29] Zhenzhen Wu, Qirong Liu, Pan Yang, Hao Chen, Qichun Zhang, Sheng Li, Yongbing Tang, and Shanqing Zhang. Molecular and morphological engineering of organic electrode materials for electrochemical energy storage. Electrochemical Energy Reviews, 5(Suppl 1):26, 2022.

[30] Sergio Manzetti and Florin Mariasiu. Electric vehicle battery technologies: From present state to future systems. Renewable and Sustainable Energy Reviews, 51:1004–1012, 2015.

[31] Cyril Ikechukwu Idu, Uwa Orji Uyor, Abimbola Patricia Popoola, Olawale M Popoola, and Sani Mohammed Adams. A review of recent advances, current limitations, and remedies of lithium-ion batteries for advanced technological applications. Future Batteries, page 100109, 2025.

[32] Joachim Dohmann. Experimentelle einführung in die elektrochemie. Berlin, Heidelberg: Springer Berlin Heidelberg. DOI, 10:978–3, 2020.

[33] D. Bresser, S. Passerini, and B. Scrosati. "Leveraging valuable Synergies by combining Alloying and Conversion for Li-Ion Anodes". Energy & Environmental Science, vol. 9, pp. 3348–3367, 2016.

[34] P. Kurzweil and O. K. Dietlmeier. Elektrochemische Speicher. Springer Fachmedien Wiesbaden, 2018.

[35] U. G. A. Office. *Science and Tech Spotlight: Advanced Batteries*. `https://www.gao.gov/products/gao-23-106332`, Accessed: 2025-02-29.

[36] M Stanley Whittingham. Ultimate limits to intercalation reactions for lithium batteries. Chemical reviews, 114(23):11414–11443, 2014.

[37] Kai Zhang, Xiaopeng Han, Zhe Hu, Xiaolong Zhang, Zhanliang Tao, and Jun Chen. Nanostructured mn-based oxides for electrochemical energy storage and conversion. Chemical Society Reviews, 44(3):699–728, 2015.

[38] P. Kurzweil. Angewandte Elektrochemie. Springer Fachmedien Wiesbaden, 2020.

[39] A. J. Bard *et al.* Electrochemical Methods: Fundamentals and Applications. Wiley, 2001.

[40] A. J. Bard *et al.* Electrochemical Dictionary. Springer Verlag GmbH, vol. 2, 2012.

[41] R. Compton and C. Banks. Understanding voltammetry. World Scientific, 2007. URL `https://www.worldscientific.com/doi/abs/10.1142/9781800615984_0005`.

[42] F. Harnisch and S. Freguia. "A basic tutorial on cyclic voltammetry for the investigation of electroactive microbial biofilms". Chemistry, an Asian journal, vol. 7, pp. 466–475, 2012.

[43] MS Al-Hoshan, JP Singh, AM Al-Mayouf, AA Al-Suhybani, and MN Shaddad. Synthesis, physicochemical and electrochemical properties of nickel ferrite spinels obtained by hydrothermal method for the oxygen evolution reaction (oer). International Journal of Electrochemical Science, 7(6):4959–4973, 2012.

[44] A. J. Bard, L. R. Faulkner, and H. S. White. "Electrochemical methods: Fundamentals and applications, 3rd edition". Transition Metal Chemistry, vol. 48, pp. 433-436, 2001. ISSN 0340-4285. doi: 10.1007/S11243-023-00555-6.

[45] E. Laviron. "General expression of the linear potential sweep voltammogram in the case of diffusionless electrochemical systems". Journal of Electroanalytical Chemistry and Interfacial Electrochemistry, vol. 101, pp. 19-28, 1979. ISSN 0022-0728. doi: 10.1016/S0022-0728(79)80075-3.

[46] Richard S Nicholson. Theory and application of cyclic voltammetry for measurement of electrode reaction kinetics. Analytical chemistry, 37(11):1351–1355, 1965.

[47] N. Elgrishi, K. J. Rountree, B. D. McCarthy, E. S. Rountree, T. T. Eisenhart, and J. L. Dempsey. "A practical Beginners Guide to Cyclic Voltammetry". Journal of Chemical EducatIon, vol. 95, pp. 197–206, Feb, 2018.

[48] J. Xiao, Q. Li, Y. Bi, M. Cai, B. Dunn, T. Glossmann, J. Liu, T. Osaka, R. Sugiura, B. Wu, J. Yang, J. G. Zhang, and M. S. Whittingham. "Understanding and applying coulombic efficiency in lithium metal batteries". Nature Energy 2020 5:8, vol. 5, pp. 561-568, 2020. Available: https://www.nature.com/articles/s41560-020-0648-z.

[49] B. VMPPotentiostat. *Biologic- VMP-3e Multichannel Potentiostat*, 2025. https://www.biologic.net/products/vmp-3e-potentiostat/.

[50] B. VSPPotentiostat. *Biologic- VSP Potentiostat*, 2025. https://www.biologic.net/products/vsp-potentiostat/.

[51] B. BatteryCyclers. *Biologic- Discover Battery Cyclers*, 2025. https://www.biologic.net/discover-battery-cyclers/.

[52] B. EC-LabSoftware. *Biologic- EC-Lab® software*, 2025. https://www.biologic.net/softwares/ec-lab-software/.

[53] T. Wickenhäuser. Investigations on organic, inorganic and hybrid materials for lithium-ion batteries. Ph. D. dissertation, Heidelberg University, 2025.

[54] Z. Xue, D. Guan, J. Zeng, Y. Cao, Z. Peng, G. Hu, , and K. Du. "Research on the assembly process of full coin cells: Key factors affecting data reliability". Ionics, vol. 29, pp. 5285–5293, 2023.

[55] KIT Campus Transfer GmbH, 2025. https://kit-campus-transfer.de/.

[56] Xe lamp power measurement conducted with Luca Bischof. 2026.

[57] Yageo Nexensos GmbH. *Yageo Nexensos 32208707 M222 Pt1000 Temperatursensor*, . 2026, Online: https://yageogroup.com/products/Sensors%20-%20Temperature/part/32208707.

[58] Fluke GmbH. *Mini-infrarotthermometer | ir-thermometer fluke 62 max | fluke*, . 2026, Online: https://www.fluke.com/de-de/produkt/temperaturmessung/ir-thermometer/fluke-62-max.

[59] Y. Yue and H. Liang. "Micro- and Nano-Structured Vanadium Pentoxide (V_2O_5) for Electrodes of Lithium-Ion Batteries". Advanced Energy Materials, vol. 17, issue 7, 1602545, 2017. Available: `https://doi.org/10.1002/aenm.201602545`.

[60] G. A. Horrocks, L. R. De Jesus, J. L. Andrews, and S. X. Banerjee. "X-ray spectroscopy and imaging as multiscale probes of intercalation phenomena in cathode materials". JOM, vol. 69, pp. 14691477, 2017. Available: `https://doi.org/10.1007/s11837-017-2398-3`.

[61] David McNulty, D Noel Buckley, and Colm O'Dwyer. Synthesis and electrochemical properties of vanadium oxide materials and structures as li-ion battery positive electrodes. Journal of Power Sources, 267:831–873, 2014.

[62] Xin Huang, Xianhong Rui, Huey Hoon Hng, and Qingyu Yan. Vanadium pentoxide-based cathode materials for lithium-ion batteries: morphology control, carbon hybridization, and cation doping. Particle & Particle Systems Characterization, 32(3):276–294, 2015.

[63] Ying Wang and Guozhong Cao. Synthesis and enhanced intercalation properties of nanostructured vanadium oxides. Chemistry of Materials, 18(12): 2787–2804, 2006.

[64] Sul Ki Park, Puritut Nakhanivej, Jeong Seok Yeon, Kang Ho Shin, Wesley M Dose, Michael De Volder, Jin Bae Lee, Hae Jin Kim, and Ho Seok Park. Electrochemical and structural evolution of structured v2o5 microspheres during li-ion intercalation. journal of energy chemistry, 55:108–113, 2021.

[65] Patient D Nzengu, Ntuthuko W Hlongwa, Kutloano E Sekhosana, and Mesfin A Kebede. Enhancing vanadium pentoxide-based (v 2 o 5) cathodes for high-performance aqueous zinc-ion batteries: optimization of interlayer spacing, ion kinetics, voltage window. RSC advances, 15(41):34362–34398, 2025.

[66] Kowsalya Palanisamy, Ji Hyun Um, Mihee Jeong, and Won-Sub Yoon. Porous v2o5/rgo/cnt hierarchical architecture as a cathode material: Emphasis on the contribution of surface lithium storage. Scientific reports, 6(1):31275, 2016.

[67] Jolanta Świątowska-Mrowiecka, Vincent Maurice, Sandrine Zanna, Lorena Klein, and Philippe Marcus. Xps study of li ion intercalation in v2o5 thin

films prepared by thermal oxidation of vanadium metal. Electrochimica Acta, 52(18):5644–5653, 2007.

[68] Dongliang Chao, Xinhui Xia, Jilei Liu, Zhanxi Fan, Chin Fan Ng, Jianyi Lin, Hua Zhang, Ze Xiang Shen, and Hong Jin Fan. A v2o5/conductive-polymer core/shell nanobelt array on three-dimensional graphite foam: a high-rate, ultrastable, and freestanding cathode for lithium-ion batteries. Advanced materials, (33):5794–5800, 2014.

[69] Gregory A Horrocks, Maliek F Likely, Jesus M Velazquez, and Sarbajit Banerjee. Finite size effects on the structural progression induced by lithiation of v 2 o 5: a combined diffraction and raman spectroscopy study. Journal of Materials Chemistry A, 1(48):15265–15277, 2013.

[70] Luis R De Jesus, Justin L Andrews, Abhishek Parija, and Sarbajit Banerjee. Defining diffusion pathways in intercalation cathode materials: some lessons from v2o5 on directing cation traffic. ACS Energy Letters, 3(4):915–931, 2018.

[71] Wenjie Wang, Haiyan Wang, Suqin Liu, and Jianhan Huang. Synthesis of γ-liv2o5 nanorods as a high-performance cathode for li ion battery. Journal of Solid State Electrochemistry, 16(7):2555–2561, 2012.

[72] C Delmas, H Cognac-Auradou, JM Cocciantelli, M Ménétrier, and JP Doumerc. The lixv2o5 system: An overview of the structure modifications induced by the lithium intercalation. Solid State Ionics, 69(3-4):257–264, 1994.

[73] Khemchand Dewangan, Nupur Nikkan Sinha, Padmakar G Chavan, Prashant K Sharma, Avinash C Pandey, MA More, DS Joag, N Munichandraiah, and NS Gajbhiye. Synthesis and characterization of self-assembled nanofiber-bundles of v2o5: their electrochemical and field emission properties. Nanoscale, 4(2):645–651, 2012.

[74] Patrick Rozier, Jean Michel Savariault, and Jean Galy. A new interpretation of the lixv2o5 electrochemical behaviour for $1< x< 3$. Solid State Ionics, 98 (3-4):133–144, 1997.

[75] Illustrated with the help of ChatGPT and Photoshop. 2026.

[76] Copper shielding tape "CMC 38382", *CMC Klebetechnik GmbH*. https://www.cmc.de/en/kupfer-abschirmband.

[77] Andrew Chen, Hsuan-Yu Chen, and Chiachung Chen. A software improvement technique for platinum resistance thermometers. Instruments, 4(2):15, 2020.

[78] International Electrotechnical Commission. *IEC 60751: Industrial Platinum Resistance Thermometers and Platinum Temperature Sensors*. 2008.

[79] 2025. E. Mijowska, Private Communication.

[80] Heng-guo Wang, De-long Ma, Yun Huang, and Xin-bo Zhang. Electrospun v2o5 nanostructures with controllable morphology as high-performance cathode materials for lithium-ion batteries. Chemistry–A European Journal, 18 (29):8987–8993, 2012.

[81] Ayelet Odani, Vilas Ganpat Pol, Swati Vilas Pol, Maxim Koltypin, and Aharon Gedanken. Testing carbon-coated vox prepared via reaction under autogenic pressure at elevated temperature as li-insertion materials. materials science, 11:14, 2006.

[82] SY Zhan, CZ Wang, K Nikolowski, H Ehrenberg, G Chen, and YJ Wei. Electrochemical properties of cr doped v2o5 between 3.8 v and 2.0 v. Solid State Ionics, 180(20-22):1198–1203, 2009.

[83] Yanwei Li, Jinhuan Yao, Evan Uchaker, Jianwen Yang, Yunxia Huang, Ming Zhang, and Guozhong Cao. Leaf-like v2o5 nanosheets fabricated by a facile green approach as high energy cathode material for lithium-ion batteries. Advanced Energy Materials, 3(9):1171–1175, 2013.

[84] Michael E Spahr, Petra Stoschitzki-Bitterli, Reinhard Nesper, Otto Haas, and Petr Novák. Vanadium oxide nanotubes. a new nanostructured redox-active material for the electrochemical insertion of lithium. Journal of The Electrochemical Society, 146(8):2780–2783, 1999.

[85] Marta Prześniak-Welenc, Jakub Karczewski, J Smalc-Koziorowska, M Łapiński, Wojciech Sadowski, and Barbara Kościelska. The influence of nanostructure size on v 2 o 5 electrochemical properties as cathode materials for lithium ion batteries. RSC advances, 6(61):55689–55697, 2016.

[86] Marine Reynaud, Jon Serrano-Sevillano, and Montse Casas-Cabanas. Imperfect battery materials: a closer look at the role of defects in electrochemical performance. Chemistry of Materials, 35(9):3345–3363, 2023.

[87] Joshua P Pender, Gaurav Jha, Duck Hyun Youn, Joshua M Ziegler, Ilektra Andoni, Eric J Choi, Adam Heller, Bruce S Dunn, Paul S Weiss, Reginald M Penner, et al. Electrode degradation in lithium-ion batteries. ACS nano, 14 (2):1243–1295, 2020.

[88] Jeanne M McGraw, Christian S Bahn, Philip A Parilla, John D Perkins, Dennis W Readey, and David S Ginley. Li ion diffusion measurements in v2o5 and li (co1- xalx) o2 thin-film battery cathodes. Electrochimica Acta, 45(1-2): 187–196, 1999.

[89] Kehua Zhong, Yanmin Yang, Guigui Xu, Jian-Min Zhang, and Zhigao Huang. An ab initio and kinetic monte carlo simulation study of lithium ion diffusion on graphene. Materials, 10(7):761, 2017.

[90] Thomas Hußenether, Carlos Antônio Rufino Júnior, Tomás Selaibe Pires, Tarani Mishra, Jinesh Nahar, Akash Vaghani, Richard Polzer, Sergej Diel, and Hans-Georg Schweiger. Analysis of the measurement uncertainties in the characterization tests of lithium-ion cells. Energies, 19(3):825, 2026.

[91] Gianfranco Carotenuto. Study of the kapton-h fundamental absorption edge and tailing behaviour. Engineering Proceedings, 105(1):7, 2025.

[92] Andrea Presciutti, Francesco Asdrubali, Assunta Marrocchi, Alessandra Broggi, Giuliano Pizzoli, and Alessio Damiani. Sun simulators: development of an innovative low cost film filter. Sustainability, 6(10):6830–6846, 2014.

[93] Maria Sofia Palagonia, Collins Erinmwingbovo, Doriano Brogioli, and Fabio La Mantia. Comparison between cyclic voltammetry and differential charge plots from galvanostatic cycling. Journal of Electroanalytical Chemistry, 847: 113170, 2019.

[94] Xiaolong Yang, Xiaolin Gao, Futao Zhang, Wei Luo, and Yongkang Duan. Experimental study on temperature difference between the interior and surface of li [ni1/3co1/3mn1/3] o2 prismatic lithium-ion batteries at natural convection and adiabatic condition. Applied Thermal Engineering, 190:116746, 2021.

[95] Rubén Usamentiaga, Pablo Venegas, Jon Guerediaga, Laura Vega, Julio Molleda, and Francisco G Bulnes. Infrared thermography for temperature measurement and non-destructive testing. Sensors, 14(7):12305–12348, 2014.

[96] European Space Agency (ESA). Material specification: Polyimide film, kapton h, hn, (ESA Document No. A.17.11). ESA Publications Division, Online: `http://esmat.esa.int/a17_11.htm`.

[97] Fluke Process Instruments. Emissivity—metals. 2023, Online: `https://www.flukeprocessinstruments.com/en-us/service-and-support/knowledge-center/infrared-technology/emissivity-metals`.

[98] ZY Jiang, JY Li, ZG Qu, L Wang, and JY Miao. Theoretical analysis on thermal grease dry-out degradation in space environment. International Journal of Thermal Sciences, 179:107694, 2022.

[99] Zoubir Acem, Damien Brissinger, Anthony Collin, Gilles Parent, Pascal Boulet, Thi Hay Yen Quach, Benjamin Batiot, Franck Richard, and Thomas Rogaume. Surface temperature of carbon composite samples during thermal degradation. International Journal of Thermal Sciences, 112:427–438, 2017.

[100] Qiang Zhen, Ling Li, Rong Li, Fei Lu, Zhenquan Li, and Yali Wang. Morphology controllable preparation and infrared emissivity of vanadium pentoxide. Infrared Physics & Technology, 71:303–306, 2015.

[101] Sen Xin, Lin Gu, Na-Hong Zhao, Ya-Xia Yin, Long-Jie Zhou, Yu-Guo Guo, and Li-Jun Wan. Smaller sulfur molecules promise better lithium–sulfur batteries. Journal of the American Chemical Society, 134(45):18510–18513, 2012.

[102] Chong Zhang, Rui Kong, Xue Wang, Yunfeng Xu, Feng Wang, Wenfeng Ren, Yanhong Wang, Fabing Su, and Jia-Xing Jiang. Porous carbons derived from hypercrosslinked porous polymers for gas adsorption and energy storage. Carbon, 114:608–618, 2017.

[103] Pan Mu, Wenyan Ma, Yongbo Zhao, Chong Zhang, Shijie Ren, Feng Wang, Chao Yan, Yu Chen, Jing Hui Zeng, and Jia-Xing Jiang. Facile preparation of mno/nitrogen-doped porous carbon nanotubes composites and their application in energy storage. Journal of Power Sources, 426:33–39, 2019.

[104] Ken Sakaushi, Eiji Hosono, Georg Nickerl, Thomas Gemming, Haoshen Zhou, Stefan Kaskel, and Jürgen Eckert. Aromatic porous-honeycomb electrodes for a sodium-organic energy storage device. Nature communications, 4(1):1485, 2013.

[105] Ye Shi, Lele Peng, Yu Ding, Yu Zhao, and Guihua Yu. Nanostructured conductive polymers for advanced energy storage. Chemical Society Reviews, 44 (19):6684–6696, 2015.

[106] Zhiping Song, Yumin Qian, Mikhail L Gordin, Duihai Tang, Terrence Xu, Minoru Otani, Hui Zhan, Haoshen Zhou, and Donghai Wang. Polyanthraquinone as a reliable organic electrode for stable and fast lithium storage. Angewandte Chemie International Edition, 54(47):13947–13951, 2015.

[107] Takeshi Shimizu, Naoki Tanifuji, and Hirofumi Yoshikawa. Azo compounds as active materials of energy storage systems. Angewandte Chemie International Edition, 61(36):e202206093, 2022.

[108] Chao Luo, Gui-Liang Xu, Xiao Ji, Singyuk Hou, Long Chen, Fei Wang, Jianjun Jiang, Zonghai Chen, Yang Ren, Khalil Amine, et al. Reversible redox chemistry of azo compounds for sodium-ion batteries. Angewandte Chemie International Edition, 57(11):2879–2883, 2018.

[109] Günter Grampp, Claudia Mureşanu, and Stephan Landgraf. Solvent influence on the electrochemical reduction of photochemically generated cis-azobenzene. Journal of Electroanalytical Chemistry, 582(1-2):171–178, 2005.

[110] E. Hückel. Quantentheoretische Beiträge zum Benzolproblem. Z. Phys. Chem, 70:204–286, 1931.

[111] Sen Zhang, Fangfang Xing, Ling Chen, Xiujuan Wang, and Xiaoming He. Tuning the azo location in conjugated polymers toward high-performance lithium-ion batteries. Chemistry of Materials, 34(20):9031–9041, 2022.

[112] Shengyang Dong, Hang Ren, Jinyao Yang, Jingyuan Zhang, Zeyu Cao, Lifen Long, Zikang Xu, Huaiyu Shao, and Xiaogang Zhang. An aqueous proton battery under alkaline electrolyte. Energy Storage Materials, 74:103888, 2025.

[113] Chao Luo, Xiao Ji, Singyuk Hou, Nico Eidson, Xiulin Fan, Yujia Liang, Tao Deng, Jianjun Jiang, and Chunsheng Wang. Azo compounds derived from electrochemical reduction of nitro compounds for high performance li-ion batteries. Advanced Materials, 30(23):1706498, 2018.

[114] Jiawen Wang, Yifan Tong, Weiwei Huang, and Qichun Zhang. Conjugated azo compounds as active materials for rechargeable sodium-metal batteries with high-rate performance. Batteries & Supercaps, 6(2):e202200413, 2023.

[115] Sirakorn Wiratchan, Thanapat Autthawong, Waewwow Yodying, Sireenart Surinwong, Takumi Konno, Thapanee Sarakonsri, and Natthawat Semakul. Easily accessible and tunable porous organic polymer anode from azo coupling for sustainable lithium-organic batteries. Chemical Engineering Journal, 466: 143090, 2023.

[116] Shengliang Zhang, Wei Huang, Pu Hu, Changshui Huang, Chaoqun Shang, Chuanjian Zhang, Renqiang Yang, and Guanglei Cui. Conjugated microporous polymers with excellent electrochemical performance for lithium and sodium storage. Journal of Materials Chemistry A, 3(5):1896–1901, 2015.

[117] Shunqi Xu, Gang Wang, Bishnu P Biswal, Matthew Addicoat, Silvia Paasch, Wenbo Sheng, Xiaodong Zhuang, Eike Brunner, Thomas Heine, Reinhard Berger, et al. A nitrogen-rich 2d sp2-carbon-linked conjugated polymer framework as a high-performance cathode for lithium-ion batteries. Angewandte Chemie, 131(3):859–863, 2019.

[118] Chuanguang Wu, Mingjun Hu, Xiaorong Yan, Guangcun Shan, Jinzhang Liu, and Jun Yang. Azo-linked covalent triazine-based framework as organic cathodes for ultrastable capacitor-type lithium-ion batteries. Energy Storage Materials, 36:347–354, 2021.

[119] Yanxin Yu, Qianqian Jin, Qiling Li, Huapeng Sun, Yanbiao Ren, Shubiao Xia, Shi Wang, and Zhong Jin. Fully extended conjugated azo-bridged covalent triazine framework with maximum dual-redox-active sites for advanced lithium organic batteries. Nano Energy, 137:110808, 2025.

[120] Manjit Singh Grewal, Kazuaki Kisu, Shin-ichi Orimo, and Hiroshi Yabu. Photo-crosslinked polymer electrolytes containing solvate ionic liquids: an ap-

proach to achieve both good mechanical and electrochemical performances for rechargeable lithium ion batteries. Chemistry Letters, 49(12):1465–1469, 2020.

[121] Klaus Ruhland, Fereshteh Habibollahi, and Robert Horny. Quantification and elucidation of the uv-light triggered initiation kinetics of tpo and bapo in liquid acrylate monomer. Journal of Applied Polymer Science, 137(6):48357, 2020.

[122] 2026. C. Delavier, Private Communication.

[123] Xuesong Lu, Guo J Lian, James Parker, Ruihuan Ge, Milan K Sadan, Rachel M Smith, and Denis Cumming. Effect of carbon blacks on electrical conduction and conductive binder domain of next-generation lithium-ion batteries. Journal of Power Sources, 592:233916, 2024.

[124] Peter M Attia, Supratim Das, Stephen J Harris, Martin Z Bazant, and William C Chueh. Electrochemical kinetics of sei growth on carbon black: Part i. experiments. Journal of The Electrochemical Society, 166(4):E97–E106, 2019.

[125] Xiayin Yao, Ning Huang, Fudong Han, Qiang Zhang, Hongli Wan, Jean Pierre Mwizerwa, Chunsheng Wang, and Xiaoxiong Xu. High-performance all-solid-state lithium–sulfur batteries enabled by amorphous sulfur-coated reduced graphene oxide cathodes. Advanced Energy Materials, 7(17):1602923, 2017.

[126] Jingwei Hu, Shengwen Zhong, and Tingting Yan. Using carbon black to facilitate fast charging in lithium-ion batteries. Journal of Power Sources, 508: 230342, 2021.

[127] Xuexue Pan, Wenkai Li, Xiaoting Lai, Yongqi Liang, Zicheng Jiang, Xiaoling Luo, and Rong Hu. Electrolyte design strategies for next-generation supercapacitors and metal-ion batteries. Emergent Materials, pages 1–75, 2025.

[128] Diego Ramón Lobato-Peralta, Patrick U Okoye, and Cinthia Alegre. A review on carbon materials for electrochemical energy storage applications: State of the art, implementation, and synergy with metallic compounds for supercapacitor and battery electrodes. Journal of Power Sources, 617:235140, 2024.

[129] Sean J Ashton and Matthias Arenz. Comparative dems study on the electrochemical oxidation of carbon blacks. Journal of Power Sources, 217:392–399, 2012.

[130] David Theuerkauf and Lukas Swan. Characteristics of open circuit voltage relaxation in lithium-ion batteries for the purpose of state of charge and state of health analysis. Batteries, 8(8):77, 2022.

[131] Hao Cui, Dongsheng Ren, Mengchao Yi, Sixuan Hou, Kai Yang, Hongmei Liang, Xuning Feng, Xuebing Han, Youzhi Song, Li Wang, et al. Operando monitoring of the open circuit voltage during electrolyte filling ensures high performance of lithium-ion batteries. Nano Energy, 104:107874, 2022.

[132] Jeff R Dahn, Tao Zheng, Yinghu Liu, and JS Xue. Mechanisms for lithium insertion in carbonaceous materials. Science, 270(5236):590–593, 1995.

[133] M Endo, C Kim, K Nishimura, T Fujino, and K Miyashita. Recent development of carbon materials for li ion batteries. Carbon, 38(2):183–197, 2000.

[134] Liulin Que and Wei Chen. Analysis of the lithium electrodeposition behavior in the charge process of lithium metal battery associated with overpotential. Journal of Power Sources, 557:232536, 2023.

[135] Yosuke Ugata, Chihaya Motoki, Kaoru Dokko, and Naoaki Yabuuchi. Fundamental methods of electrochemical characterization of li insertion materials for battery researchers. Journal of Solid State Electrochemistry, 28(3):1387–1401, 2024.

[136] Chao Luo, Oleg Borodin, Xiao Ji, Singyuk Hou, Karen J Gaskell, Xiulin Fan, Ji Chen, Tao Deng, Ruixing Wang, Jianjun Jiang, et al. Azo compounds as a family of organic electrode materials for alkali-ion batteries. Proceedings of the National Academy of Sciences, 115(9):2004–2009, 2018.

[137] Robin Lundstrom, Neeha Gogoi, Tim Melin, and Erik J Berg. Unveiling reaction pathways of ethylene carbonate and vinylene carbonate in li-ion batteries. The Journal of Physical Chemistry C, 128(20):8147–8153, 2024.

[138] Paul G Kitz, Matthew J Lacey, Petr Novák, and Erik J Berg. Operando investigation of the solid electrolyte interphase mechanical and transport properties formed from vinylene carbonate and fluoroethylene carbonate. Journal of Power Sources, 477:228567, 2020.

[139] Kjell Schroder, Judith Alvarado, Thomas A Yersak, Juchuan Li, Nancy Dudney, Lauren J Webb, Ying Shirley Meng, and Keith J Stevenson. The effect of

fluoroethylene carbonate as an additive on the solid electrolyte interphase on silicon lithium-ion electrodes. Chemistry of Materials, 27(16):5531–5542, 2015.

[140] Simon-Johannes Kinkelin, Fridolin Roeder, Katja Vogel, Matthias Steimecke, and Michael Bron. A fundamental study on cyclic voltammetry at porous carbon thin-film electrodes. Electrochimica Acta, 488:144183, 2024.

[141] Noémie Elgrishi, Kelley J Rountree, Brian D McCarthy, Eric S Rountree, Thomas T Eisenhart, and Jillian L Dempsey. A practical beginner's guide to cyclic voltammetry. Journal of chemical education, 95(2):197–206, 2018.

[142] Eduardo Laborda, Javier Lopez-Asanza, and Angela Molina. Theoretical framework and guidelines for the cyclic voltammetry of closed bipolar cells. Analytical Chemistry, 95(47):17311–17317, 2023.

[143] Binglin Tao, Ian J McPherson, Enrico Daviddi, Cameron L Bentley, and Patrick R Unwin. Multiscale electrochemistry of lithium manganese oxide (limn2o4): from single particles to ensembles and degrees of electrolyte wetting. ACS sustainable chemistry & engineering, 11(4):1459–1471, 2023.

[144] Qing Zhang, Xun Cui, Shumeng Hao, Qiang Zhang, Zaiping Guo, Huiqiao Li, Zhiqun Lin, and Yingkui Yang. Chain engineering of carbonyl polymers for sustainable lithium-ion batteries. Materials Today, 50:170–198, 2021.

[145] Tami C Bond and Robert W Bergstrom. Light absorption by carbonaceous particles: An investigative review. Aerosol science and technology, 40(1):27–67, 2006.

[146] Dong Joo Min, Kyunam Lee, Hyunji Park, Ji Eon Kwon, and Soo Young Park. Redox potential tuning of s-tetrazine by substitution of electron-withdrawing/donating groups for organic electrode materials. Molecules, 26 (4):894, 2021.

[147] Yu Ding, Changkun Zhang, Leyuan Zhang, Yangen Zhou, and Guihua Yu. Molecular engineering of organic electroactive materials for redox flow batteries. Chemical Society Reviews, 47(1):69–103, 2018.

[148] Dominic Schatz, Chris Burdenski, Finn M Schneider, Max M Hansmann, and Hermann A Wegner. Amino-substituted azoxybenzenes as potential

redox-active catholyte materials. Chemistry–A European Journal, 31(21): e202404001, 2025.

[149] Keithley Instruments. Model 2000 multimeter user's manual, 2000.

Acknowledgments

Abschließend möchte ich mich bei all denen bedanken, ohne die diese Arbeit nicht möglich gewesen wäre. Im Besonderen sind dies:

Prof. Dr. Rüdiger Klingeler für die freundliche Aufnahme in die Arbeitsgruppe, die Möglichkeit an solch einem interessanten Thema zu arbeiten sowie die kontinuierliche Unterstützung und Verfügbarkeit zum Beantworten von Fragen.

JProf. Dr. Loredana Gastaldo für die freundliche Übernahme der Zweitkorrektur dieser Arbeit.

Dr. Tom Wickenhäuser für die tolle Betreuung und Zusammenarbeit im Labor, das Beantworten von zahlreichen Fragen, der gemeinsamen Interpretationsarbeit von diversen Messergebnissen und natürlich für das Korrekturlesen dieser Arbeit. Viel Erfolg dir weiterhin!

Luca Bischof für viele bereichernde Diskussionen zu den Lichtmessungen und dem dazugehörigen experimentellen Aufbau.

Christian Delavier für die Synthese der Azo-Materialien sowie die zahlreichen interessanten Diskussionen zu diesem Thema.

Allen Mitgliedern der Arbeitsgruppe F25 für die freundliche und motivierende Arbeitsatmosphäre sowie die vielen genussvollen Kuchenpausen, die die Zeit in der Gruppe besonders angenehm gemacht haben.

Zu guter Letzt gilt ein besonderer Dank an meine Familie und meine Freunde für die grenzenlose Unterstützung im gesamten Studium und darüber hinaus.

Ich versichere, dass ich diese Arbeit selbstständig verfasst und keine anderen als die angegebenen Quellen und Hilfsmittel benutzt habe.



Heidelberg, den 19.05.2026 .....

(Pavel Rozov)